

2

NAVAL POSTGRADUATE SCHOOL

Monterey, California

AD-A240 868



DTIC
ELECTE
SEP 30 1991
S D D



THESIS

PERFORMANCE ANALYSIS OF HIGH FREQUENCY
SINGLE-SITE-LOCATION ANTENNA ARRAYS
USING NUMERICAL ELECTROMAGNETIC MODELING

by

Harry Thornberry Schiantarelli

September, 1990

Thesis Advisor:

Richard W. Adler

Approved for public release; distribution is unlimited.

91-11757



91 9 27 022

REPORT DOCUMENTATION PAGE				
1a REPORT SECURITY CLASSIFICATION UNCLASSIFIED			1b RESTRICTIVE MARKINGS	
2a SECURITY CLASSIFICATION AUTHORITY			3 DISTRIBUTION/AVAILABILITY OF REPORT Approved for public release; distribution is unlimited.	
2b DECLASSIFICATION/DOWNGRADING SCHEDULE				
4 PERFORMING ORGANIZATION REPORT NUMBER(S)			5 MONITORING ORGANIZATION REPORT NUMBER(S)	
6a NAME OF PERFORMING ORGANIZATION Naval Postgraduate School	6b OFFICE SYMBOL (If applicable) EW	7a NAME OF MONITORING ORGANIZATION Naval Postgraduate School		
6c ADDRESS (City, State, and ZIP Code) Monterey, CA 93943-5000		7b ADDRESS (City, State, and ZIP Code) Monterey, CA 93943-5000		
8a NAME OF FUNDING/SPONSORING ORGANIZATION	8b OFFICE SYMBOL (If applicable)	9 PROCUREMENT INSTRUMENT IDENTIFICATION NUMBER		
8c ADDRESS (City, State, and ZIP Code)		10 SOURCE OF FUNDING NUMBERS		
		Program Element No	Project No	Task No
				Work Unit Accession Number
11 TITLE (Include Security Classification) PERFORMANCE ANALYSIS OF HIGH FREQUENCY SINGLE-SITE-LOCATION ANTENNA ARRAYS USING NUMERICAL ELECTROMAGNETIC MODELING				
12 PERSONAL AUTHOR(S) THORNBERRY, HARRY				
13a TYPE OF REPORT Master's Thesis	13b TIME COVERED From To	14 DATE OF REPORT (year, month, day) September 1990	15 PAGE COUNT 125	
16 SUPPLEMENTARY NOTATION The views expressed in this thesis are those of the author and do not reflect the official policy or position of the Department of Defense or the U.S. Government.				
17 COSATI CODES			18 SUBJECT TERMS (continue on reverse if necessary and identify by block number)	
FIELD	GROUP	SUBGROUP	SINGLE-SITE LOCATION, DIRECTION FINDING, HIGH FREQUENCY, NUMERICAL ELECTROMAGNETICS CODE.	
19 ABSTRACT (continue on reverse if necessary and identify by block number) Electronic support measures (EW) systems play an increasingly important role in modern warfare and can influence the outcome of a military engagement. The application of ESM can be extended to anti-guerrilla and anti-drug operations where law enforcement agencies can exploit the fact that their presence is inducing the outlaw to depend more on radio communications to coordinate their activities. When a propagation path of no more than one reflection at the ionosphere (1-hop) can be assumed, position of an HF emitter can be determined by a single observing site using vertical triangulation, provided that the height of the ionosphere at the point where the radio wave is reflected, can be determined. This technique is known as "high frequency direction finding single-site-location" (HFDF SSL). This thesis analyzes the HFDF SSL error in measuring the direction of arrival of the signal, how this error is generated by the antenna array and its effect on emitter location. The characteristics of the two antenna arrays used by a specific HFDF SSL system that implements the phase-interferometer technique were studied using electromagnetic modeling. Results showed that angle-of-arrival errors for the high band array were less than 0.5° and were under 0.2° for the low band antenna system. The maximum HFDF SSL lateral and range error of this system were found to be 8.7 km and 22.4 km respectively for the high band array, when the targeted emitter is located at 500 km, and the incoming wave has an E- propagation mode. The smallest lateral and range error were found to be 2.1 km and 4.3 km respectively for the low band array, when the targeted emitter is located at 300 km, and the incoming wave has an E-mode.				
20 DISTRIBUTION/AVAILABILITY OF ABSTRACT <input checked="" type="checkbox"/> UNCLASSIFIED UNLIMITED <input type="checkbox"/> SAME AS REPORT <input type="checkbox"/> LIMITATIONS			21 ABSTRACT SECURITY CLASSIFICATION	
22a. NAME OF RESPONSIBLE INDIVIDUAL Richard W. Adler			22b TELEPHONE (Include Area code) (408) 646-2352	22c OFFICE SYMBOL EC/Ab

Approved for public release; distribution is unlimited.

Performance Analysis of High Frequency
Single-Site-Location Antenna Arrays
Using Numerical Electromagnetic Modeling

by

Harry Thornberry Schiantarelli
Commander, Peruvian Navy

Submitted in partial fulfillment
of the requirements for the degree of

MASTER OF SCIENCE IN ELECTRICAL ENGINEERING
AND
MASTER OF SCIENCE IN SYSTEMS ENGINEERING
(Electronic Warfare)

from the


NAVAL POSTGRADUATE SCHOOL
September 1990

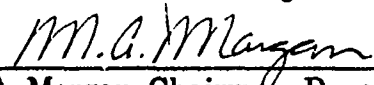
Author:

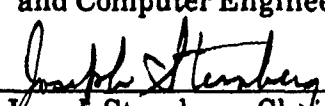

Harry Thornberry Schiantarelli

Approved by:


Richard W. Adler, Thesis Advisor


Stephen Jauregui, Second Reader


Michael A. Morgan, Chairman, Department of Electrical
and Computer Engineering


Joseph Sternberg, Chairman,
Electronic Warfare Academic Group

ABSTRACT

Electronic support measures (ESM) systems play an increasingly important role in modern warfare and can influence the outcome of a military engagement. The application of ESM can be extended to anti-guerrilla and anti-drug operations where law enforcement agencies can exploit the fact that their presence is inducing the outlaw to depend more on radio communications to coordinate their activities. When a propagation path of no more than one reflection at the ionosphere (1-hop) can be assumed, position of an HF emitter can be determined by a single observing site using vertical triangulation, provided that the height of the ionosphere at the point where the radio wave is reflected, can be determined. This technique is known as "high frequency direction finding single-site-location" (HFDF SSL). This thesis analyzes the HFDF SSL error in measuring the direction of arrival of the signal, how this error is generated by the antenna array and its effect on emitter location. The characteristics of the two antenna arrays used by a specific HFDF SSL system that implements the phase-interferometer technique were studied using electromagnetic modeling. Results showed that angle-of-arrival errors for the high band array were less than 0.5° and were under 0.2° for the low band antenna system. The maximum HFDF SSL lateral and range error of this system were found to be 8.7 km and 22.4 km respectively for the high band array, when the targeted emitter is located at 500 km, and the incoming wave has an E-propagation mode. The smallest lateral and range error were found to be 2.1 km and 4.3 km respectively for the low band array, when the targeted emitter is located at 300 km, and the incoming wave has an E-mode.



Accession For	
NTIS	CRA&I
DTIC	TAB
Unannounced	
Justification	
By	
Distribution /	
Availability Codes	
Dist	Avail and/or Special
A-1	

TABLE OF CONTENTS

I. INTRODUCTION	1
A. OVERVIEW	1
B. DF TECHNIQUES	3
C. PURPOSE OF THE THESIS	6
D. TACTICAL SCENARIO	7
II. HIGH FREQUENCY SINGLE-SITE-LOCATION DIRECTION FINDING ...	9
A. THE CONCEPT OF A PHASE-INTERFEROMETER	9
B. PHASE-INTERFEROMETER BASELINE TYPES	11
C. IONOSPHERIC CONSIDERATIONS	20
D. HFDF SSL VERTICAL TRIANGULATION	26
E. TYPICAL HFDF SSL PATHS	28
III. NEC MODELING	30
A. BACKGROUND	30
B. SWRI HFDF SSL SYSTEM DESCRIPTION	31
C. COMPUTER MODEL DEVELOPMENT	37
D. NEC DATASETS	41
IV. PERFORMANCE OF THE ANTENNAS	42
A. ANTENNA INPUT IMPEDANCE	42

B. SMITH CHART INPUT IMPEDANCE ANALYSIS	46
C. AVERAGE POWER GAIN	46
D. RADIATION PATTERNS	53
V. HFDF SSL ERROR ANALYSIS	57
A. DF MATHEMATICAL MODEL	57
B. BEARING AMBIGUITY RESOLUTION	59
C. SELECTION OF ANGLES OF ARRIVAL FOR MODEL COMPARISON	62
D. SSL ARRAY PHASE ERROR ANALYSIS	63
E. EFFECT OF SSL PHASE ERROR IN AOA MEASUREMENT	66
F. HFDF SSL ERROR AND SSL FOOTPRINT	69
VI. CONCLUSIONS AND RECOMMENDATIONS	72
A. CONCLUSIONS	72
B. RECOMMENDATIONS	74
APPENDIX A - NEC DATASETS	75
APPENDIX B - ANTENNA INPUT IMPEDANCE	78
APPENDIX C - CROSSED LOOP RADIATION PATTERNS	80
APPENDIX D - VERTICAL MONOPOLE RADIATION PATTERNS	90
APPENDIX E - PHASE ERROR ANALYSIS	100
APPENDIX F - SSL ERROR ANALYSIS	108
LIST OF REFERENCES	116
INITIAL DISTRIBUTION LIST	117

ACKNOWLEDGEMENT

I want to express my gratitude to Dr. Richard W. Adler, for his guidance, patience and support throughout the thesis work.

Special thanks to my wife, daughter, and son for their love and understanding during the difficult period of the research, and for constantly reminding me that I could do it.

I. INTRODUCTION

A. OVERVIEW

Passive electronic warfare (EW) systems play an increasingly important role in modern warfare. Electronic support measures (ESM) are now used to accomplish a number of missions that include the detection, location, identification and threat assessment of hostile emitters. Modern ESM systems provide critically important data which can influence the outcome of a military engagement.

The application of ESM can be extended to anti-guerrilla and anti-drug operations. Law enforcement agencies can use these techniques to help locate illegal installations and to obtain additional advantage from the element of surprise. Specifically, law enforcement agencies can exploit the fact that their presence is inducing increased mobility of the outlaw, which in turn will cause them to depend more on radio communications to coordinate their activities.

Passive ESM systems are harder to build, and accuracy requirements are generally more stringent than requirements for active EW systems. These systems have to work in an unfriendly and totally uncooperative signal environment. In order to be effective they must exhibit broad spectral coverage, high probability of intercept, real time operation, and high accuracy. Probably the most important component of modern ESM systems is the radio direction finder.

Radio direction finding (DF) can be defined as geographically fixing the position of a targeted transmitter both in azimuth and range, using one or more receiving sites. Virtually all DF systems derive emitter location from the measured arrival angle of the received signal. This angle of arrival is always defined in azimuth and in some cases elevation. Horizontal or azimuth triangulation is the determination of the position of an emitter using azimuth angles measured at two or more DF stations. This is the most common technique used in DF, but requires that receiving sites be separated by a distance comparable to the distance to the emitter, and their operation must be precisely synchronized in order to obtain accurate position measurements.

In the high frequency (HF) band, propagation of radio waves takes place mainly by means of reflections at the ionized layers of the atmosphere. Only at very short distances are the direct ray and surface waves of importance. By using this special characteristic, another way of DF can be implemented for HF signals provided that the height of the ionosphere at the point where the radio wave is reflected, can be determined.

When a propagation path of no more than one reflection at the ionosphere (1-hop) can be assumed for a received HF signal, emitter position location can be determined by a single observing site using vertical triangulation. This technique is known as "high frequency direction finding single-site-location" (HFDF SSL) and is used to determine location of HF emitters up to approximately 2,000 km where the sky wave signal may arrive via a 1-hop propagation path.

In the process of measuring the direction of arrival of a signal using an HFDF SSL, two basic errors can occur, one due to the uncertainty of measuring the exact direction

of arrival of the signal, and the other due to path deviations which make the direction of arrival different from the true direction of the transmitter. The first error depends on the accuracy of techniques and equipment used, and the second on the precision in determining characteristics of the ionosphere at the reflection point, at time of measurement.

This thesis will analyze the HFDF SSL error in measuring the direction of arrival of the signal, how this error is generated by the antenna array and its effect on emitter location. The characteristics of the two antenna arrays used by a specific HFDF SSL system that implements the phase-interferometer technique will be studied to find their effects on the HFDF SSL error.

B. DF TECHNIQUES

Direction finding systems can be classified in two broad categories according to the manner in which their antenna systems obtain and process information from the arriving signal of interest. These categories are scalar DF and vector (or phasor) DF systems [Ref. 1].

Scalar DF systems measure only one component of the signal of interest (such as amplitude or phase), and use the information of the measured component to determine azimuth and/or elevation angles of arrival of the signal. Vector DF systems measure simultaneously two or more components of the received signal and try to determine the characteristics of the individual rays that compose the incoming wave-field. A disadvantage of this kind of system is that a single incident wave may be defined by as

many as four parameters [Ref. 1]; thus it must have a sufficient number of antenna ports and sufficient measuring and processing capabilities so that the desired number of unknown parameters can be resolved.

Scalar DF systems are generally much simpler than vector systems and therefore are better suited for tactical use. Current scalar DF systems can be classified into three basic types:

- 1) Spinning DF
- 2) Doppler DF
- 3) Interferometer DF

1. Spinning DF

These systems, also called rotating DF systems, measure the amplitude of a signal received by a highly directive antenna or antenna array. The receive pattern of the antenna array is rotated mechanically or electronically until a null or peak is directed towards the incoming signal. The angular position of the antenna (or its pattern) provides information to compute the line of bearing to the transmitter. Spinning DF systems are by far the most commonly used type of DF systems.

Most spinning DF systems use a small aperture antenna (small antenna size compared to a wavelength) in order to achieve a receive pattern with sharp nulls, but this technique has the disadvantage of a low overall gain and the null occurs where the gain is at minimum. To overcome this limitation the patterns of two or more elements can be combined to produce sharper beamwidths and allow the use of the maximum gain portion

of the antenna receiving pattern. To achieve this, small aperture antenna elements must be used and the overall gain is still low.

Even though large aperture antenna arrays have been used to improve the gain of the system, spinning DF systems still have the disadvantage of not being instantaneous since the amount of time the antenna beam points to a certain azimuth is a small fraction of one complete rotation. This characteristic of spinning DF can induce errors in short-duration signals if the scan rate is not high enough. For a high scan rate the system has to have a wide bandwidth.

2. Doppler DF

Doppler DF systems constitute a variation of the spinning DF technique where frequency modulation is superimposed on the received signal by mechanically rotating a single omnidirectional antenna element rapidly around the perimeter of a circle [Ref. 2]. The frequency deviation or Doppler Frequency is proportional to the scan rate and the size of the circle of rotation.

A common version of this technique obtains an electronically simulated Doppler effect by smoothly commutating between fixed identical antenna elements positioned around a ring. The requirement to rotate (or commutate) the antenna elements results in the disadvantage of not being instantaneous.

An additional requirement is that the diameter of the antenna circle must be several wavelengths in order to obtain adequate resolution. This characteristic makes Doppler systems better suited for very high frequency (VHF) and above.

3. Interferometer DF

DF systems based on interferometers compare values of a specified signal parameter measured on two identical antennas (or groups of antennas) to derive the angle of arrival (AOA) of the signal. The most common parameters used for Interferometer DF measurements are amplitude, time of arrival, and phase.

DF Interferometers use the fact that the measurement of the selected parameter at each antenna would yield the same value if the signal arrived equally spaced from both antennas, creating a difference null for this direction of arrival of the signal. Any other condition will yield a difference output value which is proportional to its divergence from the null case.

Even though the three parameters mentioned are intimately related, the most common interferometer used for DF is the phase-interferometer. This study will concentrate on a specific implementation of this technique on an HFDF SSL system. The characteristics of a phase-interferometer will be covered in greater depth in the next chapter.

C. PURPOSE OF THE THESIS

The purpose of this thesis is to investigate the magnitude of the error induced in a phase-interferometer HFDF SSL system by the antenna. The research will include the analysis of two HFDF SSL antenna arrays and the DF algorithm employed by the Southwest Research Institute of San Antonio, Texas (SWRI) in its land-based HFDF SSL

system. The Numerical Electromagnetics Code (NEC) will be used to model the antenna characteristics, array geometry, and ground conditions and to simulate real DF operation.

To provide framework for the analysis of the system, a tactical scenario will be developed. This scenario will include the characteristics of medium range military land operations, as well as land based anti-guerrilla and anti-drug operations.

Specific areas of investigation described in this paper include: (1) discussion and analysis of phase-interferometers and the effects of ionospheric conditions on HFDF SSL errors; (2) analysis of the characteristics of the antennas selected; (3) modeling and analysis of the antenna array geometries used by SWRI; and (4) analysis and comparison of theoretical and simulated outputs of the HFDF SSL system and the determination of the magnitude of the errors generated by the antenna arrays and their effect on emitter location.

D. TACTICAL SCENARIO

The following theoretical scenario was developed for this research. When possible, it includes the characteristics of typical medium-range military land operations, as well as land-based anti-guerrilla and anti-drug operations. The area of operations is located near the equatorial region and the terrain conditions include the highlands (with altitudes that range from 6,000 to 10,000 feet) and the Amazon jungle. The system is intended to be used all year round and any time of day or night.

The area over which the system (including the antenna array) is to be deployed will usually be constrained to a square of less than 300 by 300 meters. The DF antenna array

should allow for easy assembly and disassembly, so it can be transported to other locations when required.

The expected distance to target emitters will range from 300 to 500 km and the operating frequencies will range from 3 to 15 MHz. Most of the target emitters will be ground-based, but occasionally air-based emitters may be of interest. The type of signals the DF system is expected to work with are single sideband (SSB) and frequency-shift keying (FSK).

II. HIGH FREQUENCY SINGLE-SITE-LOCATION DIRECTION FINDING

A. THE CONCEPT OF A PHASE-INTERFEROMETER

A phase-interferometer is a DF system that uses an array made up of one pair (or more) of identical antenna elements and determines the direction of arrival of a received signal from the relative phase measured between two antenna elements. The antennas used in this kind of systems are generally omnidirectional or have broad beamwidths (on the order of 90 degrees or more). The difference in the phase received by two antennas which are equally displaced from the incoming wave will be zero, creating a phase difference null along the boresight of the interferometer antenna pair.

In a phase-interferometer DF the signal is effectively received at the phase center of each antenna and the position of the phase center relative to each antenna is a function of the angle of arrival of the wave front. If the antennas are identical the distance between the phase centers and the slope of the line connecting them is independent of the angle of arrival of the wave front.

The line connecting the phase centers of two antennas in a phase-interferometer DF is called a baseline. An interferometer can have more than one baseline. An interferometer system that employs only 2 antennas is called a single baseline interferometer and if it employs more than 2 antenna elements it is called multiple baseline interferometer.

Interferometers have the advantage of not requiring pattern scanning as the previous DF systems. They are particularly useful for short-duration signals.

Before the study of details of a phase-interferometer the concept of a "plane wave" must first be defined. Since electromagnetic waves propagate as an expanding sphere as they move away from the transmitter, the shape of the wave front describes a circle in any plane that contains the transmitter. At long distances (many wavelengths away), the case of interest for HFDF SSL, this wave front can be treated as a straight line. When it reaches two antennas whose separation is many times smaller than the distance to the emitter, it will be referred to as a plane wave.

Baseline orientation is defined as the angle between the baseline and geographic true North. For convenience and to simplify the analysis, true North is considered to be aligned with the positive "x" axis of a 3-dimensional coordinate system, as shown in Fig. 1.

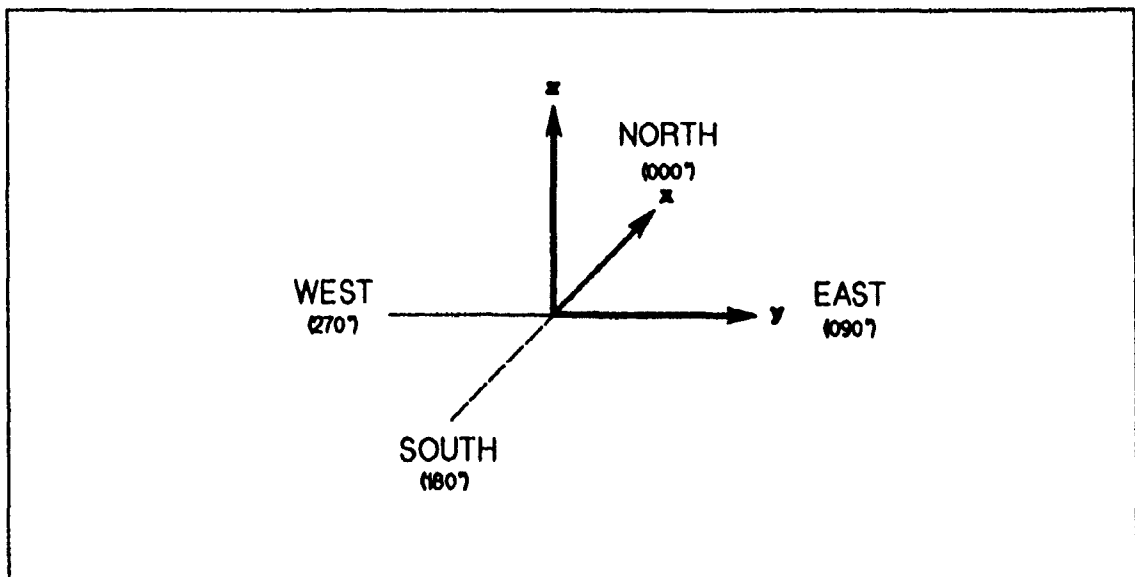


Fig. 1.- Baseline Orientation.

B. PHASE-INTERFEROMETER BASELINE TYPES

1. Single Baseline

A phase-interferometer DF system that employs only two antennas is called a single baseline interferometer and its geometry is shown in Fig. 2. In this interferometer configuration, the incident electric field intensity at antenna 1 will be

$$E_1 = E e^{j(\omega t - \beta x)} , \quad (1)$$

where

E = magnitude of the electric field intensity,

β = free space propagation constant = $2\pi/\lambda$ and

x = distance traveled by the wave.

Similarly the electric field intensity at antenna 2 will be

$$E_2 = E e^{j(\omega t - \beta x - d \cos \theta)} , \quad (2)$$

where

d = distance from antenna 1 to antenna 2 and

ψ = elevation angle of arrival of the plane wave.

Only the relative values of phase are of interest so antenna 1 can be taken to be the reference and the electric field intensities become $E_1 = E$ and $E_2 = E e^{-j\beta d \cos \theta}$.

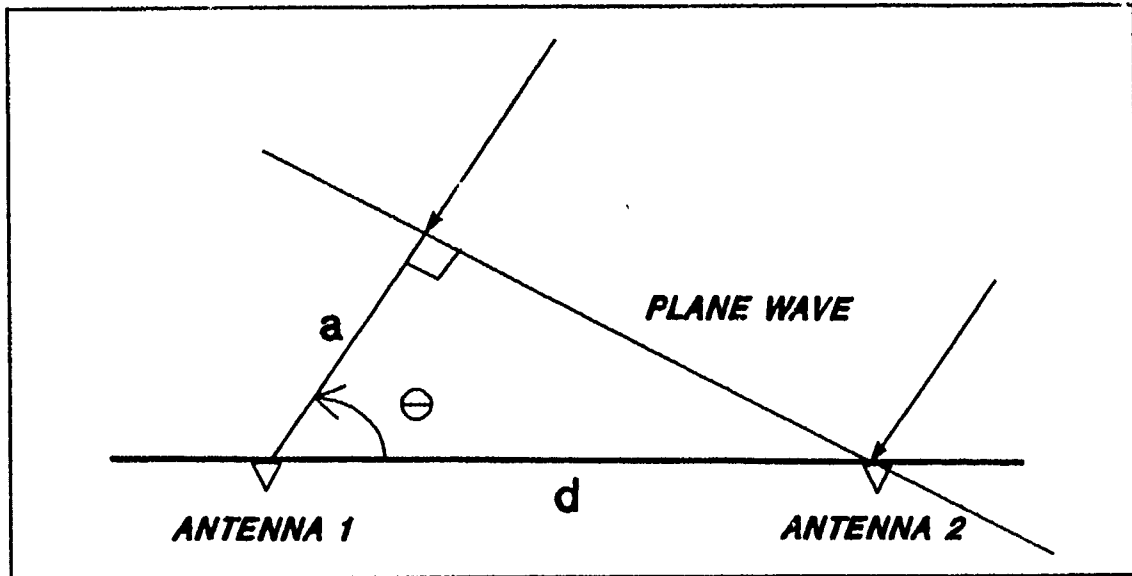


Fig. 2.- Single Baseline Phase Interferometer.

Therefore

$$\frac{E_1}{E_2} = e^{j\beta d \cos\theta} \quad (3)$$

and the signal received at antenna 1 leads the signal received at antenna 2 by the phase angle

$$\Phi_{12} = \beta d \cos\theta \quad (4)$$

From this relation the angle of arrival of the plane wave can be calculated by

$$\theta = \frac{\Phi_{12}}{\beta d} \quad (5)$$

By making the length of the interferometer baseline larger, the angle θ can be determined with greater precision and the effect of phase measurement errors on Φ_{12} will

decrease. On the other hand, a greater number of ambiguities is introduced since Φ_{12} can only be measured within 2π radians. For $0 < \Delta \Phi_{12} < 2\pi$,

$$\cos \theta = \frac{\Delta \Phi_{12} + N(2\pi)}{\left(\frac{2\pi}{\lambda}\right) d} \quad (6)$$

and

$$\frac{d}{\lambda} (\cos \theta) = \frac{\Delta \Phi_{12}}{2\pi} + N \quad (7)$$

The second term of this last expression is called the "interferometer ambiguity", since it gives the number of ambiguities that are introduced in the single baseline interferometer by the choice of baseline length, d/λ . From Fig. 3, for no ambiguities to occur, a baseline length of less than one-half wavelength is needed.

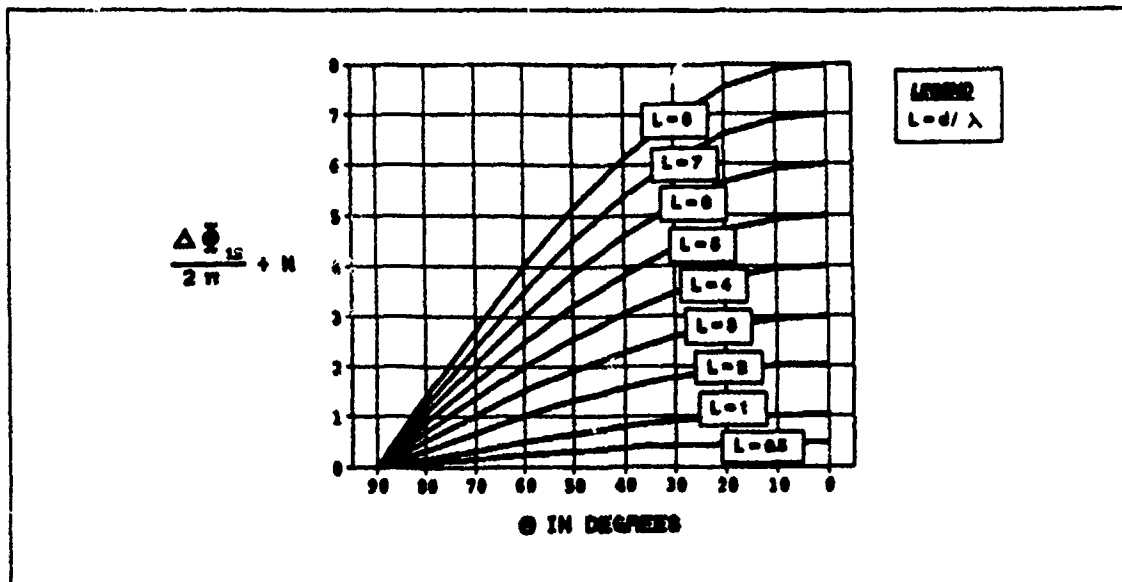


Fig. 3.- Phase Interferometer Ambiguity Function Diagram.

Thus in a single baseline interferometer, an ambiguity of $\pm \pi/2$ about the baseline occurs because of symmetry when the antenna phase centers are separated by more than one-half wavelength. Additional ambiguities occur for elements spaced at distances larger than one wavelength because the value of θ starts repeating when the phase difference, Φ_{12} , exceeds 180° .

To resolve the second kind of ambiguity the antenna phase centers are required to be at a distance less than one-half wavelength. For the first ambiguity to be resolved the field of view of the antenna array can be limited by using subsidiary front and rear pointing antennas and comparing their amplitudes. Alternatively, a second baseline can be used and their phase differences combined.

In a single baseline interferometer when the elevation angle of the incident wave is not zero, the locus of points that produce the same phase delay forms a cone of revolution about the axis of symmetry between antennas 1 and 2. The exact direction of arrival of the incoming signal cannot be determined in this case because various combinations of azimuth, ϕ , and elevation, ψ , can give the same value of phase delay.

Therefore, a two-element phase system provides the possibility of measuring the angle of arrival, θ , of an elevated wave, but in an ambiguous way. There is also a lack of sensitivity to elevation angles near broadside for a 2-element antenna array. To accurately determine the angle of arrival of a wave both in azimuth and elevation, the phase measurements of two or more interferometer baselines must be combined.

2. Multiple Baselines

Interferometers with more than one baseline allow the use of longer baselines to increase the aperture of the array while keeping at least one short baseline (less than one-half wavelength) to resolve ambiguities.

By increasing the aperture of the array, the angle of arrival of a signal can be determined with greater precision. The resolution of a multiple baseline interferometer is given by the widest antenna pair (baseline).

This study will analyze a multiple baseline phase-interferometer antenna array developed by SWRI. In this interferometer the 3-dimensional angle of arrival of a plane wave is resolved by using the phase across two apertures that are not parallel.

Consider the coordinate system for a non-parallel baseline interferometer, as shown in Fig. 4, with three antennas located at $P_0(0,0,0)$, $P_1(x_1,y_1,z_1)$, and $P_2(x_2,y_2,z_2)$.

Antenna P_0 is the reference antenna and its phase center is located at the earth's surface. The computed values of azimuth and elevation will be referenced to a plane which is tangent to the earth's surface at P_0 .

Let the shortest distance between a normal to the plane wave that goes through antenna P_0 and the point P_1 be $P_A P_1$. Similarly, let the shortest distance between a normal to the plane wave, passing through antenna P_0 and the point P_2 be $P_B P_1$.

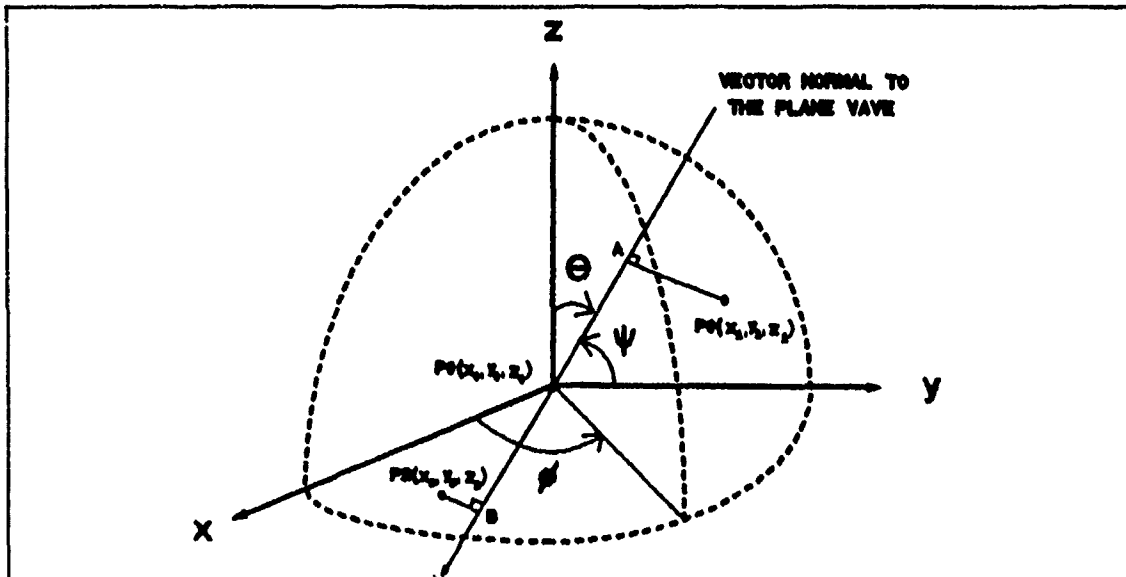


Fig. 4.- Coordinate System for Non-Parallel Baseline Interferometer.

Assuming a plane wave arriving from azimuth, ϕ , and elevation, ψ , where $\psi = 90^\circ - \theta$, the phase difference induced on each base line is given by

$$\text{Phase difference } P_0 P_1 = \beta(\overline{P_0 P_A}) = P_{01} \quad (8)$$

$$\text{Phase difference } P_0 P_2 = \beta(\overline{P_0 P_B}) = P_{02} \quad (9)$$

where

$\overline{P_0 P_A}$ = distance from P_0 to P_A and

$\overline{P_0 P_B}$ = distance from P_0 to P_B .

To derive an expression for $\overline{P_0 P_A}$, the coordinates of point P_A must first be found. From Fig. 4,

$$\tan\phi = \frac{y_A}{x_A} , \quad (10)$$

therefore

$$y_A = x_A \tan\phi ; \quad (11)$$

in addition

$$\cos\phi = \frac{x_A}{\sqrt{x_A^2 + y_A^2}} ; \quad (12)$$

then

$$\sqrt{x_A^2 + y_A^2} = \frac{x_A}{\cos\phi} \quad (13)$$

and finally

$$\tan\psi = \frac{z_A}{\sqrt{x_A^2 + y_A^2}} = \frac{z_A}{\left(\frac{x_A}{\cos\phi} \right)} . \quad (14)$$

The coordinates of P_A can now be expressed as

$$\left(x_A , X_A \tan\phi , \frac{x_A \tan\psi}{\cos\phi} \right) ; \quad (15)$$

therefore the distance $\overline{P_A P_1}$ becomes

$$(\overline{P_A P_1})^2 = (x_A - x_1)^2 + (y_A - y_1)^2 + (z_A - z_1)^2 \quad (16)$$

and

$$(\overline{P_A P_1})^2 = (x_A - x_1)^2 + (x_A \tan \phi - y_1)^2 + \left(\frac{x_A \tan \psi}{\cos \phi} - z_1 \right)^2 . \quad (17)$$

Next, to minimize this distance

$$\frac{d(\overline{P_A P_1})^2}{dx} = 0 . \quad (18)$$

Using this expression and solving for x_A , y_A and z_A yields

$$x_A = x_1 \cos^2 \phi \cos^2 \psi + y_1 \cos \phi \sin \phi \cos^2 \psi + z_1 \cos \phi \cos \psi \sin \psi , \quad (19)$$

$$y_A = x_A \tan \phi , \quad (20)$$

and

$$z_A = x_A \sec \phi \tan \psi . \quad (21)$$

The distance $\overline{P_O P_A}$ can then be found by

$$\overline{P_O P_A} = \sqrt{x_A^2 + y_A^2 + z_A^2} \quad (22)$$

or

$$\overline{P_O P_A} = x_1 \cos \phi \cos \psi + y_1 \sin \phi \cos \psi + z_1 \sin \psi . \quad (23)$$

The same procedure can be repeated for $\overline{P_O P_B}$ to find

$$\overline{P_O P_B} = x_2 \cos \phi \cos \psi + y_2 \sin \phi \cos \psi + z_2 \sin \psi . \quad (24)$$

For a plane wave arriving from azimuth, ϕ , and elevation, ψ , it is possible to express the phase difference induced in each baseline measurement as the distance a wave travels between points P_A and P_B to point P_o , as

$$P_{o1} = \frac{2\pi}{\lambda} (x_1 \cos\phi \cos\psi + y_1 \sin\phi \cos\psi + z_1 \sin\psi) \quad (25)$$

and

$$P_{o2} = \frac{2\pi}{\lambda} (x_2 \cos\phi \cos\psi + y_2 \sin\phi \cos\psi + Z_2 \sin\psi) \quad (26)$$

In practice, the values of the coordinates of the three antennas and the frequency of the incoming signal are known, and the phase difference P_{o1} and P_{o2} can be measured. The two equations and two unknowns can be solved for the azimuth, ϕ , and elevation, ψ , of the incoming wave.

To simplify the process, the following variables can be defined as

$$a_1 = \left(\frac{P_{o1}}{\beta} \right) x_2 - \left(\frac{P_{o2}}{\beta} \right) x_1, \quad (27)$$

$$a_2 = \left(\frac{P_{o1}}{\beta} \right) y_2 - \left(\frac{P_{o2}}{\beta} \right) y_1, \quad (28)$$

$$a_3 = \left(\frac{P_{01}}{\beta} \right) z_1 - \left(\frac{P_{02}}{\beta} \right) z_2 , \quad (29)$$

$$b_1 = z_1 x_2 - z_2 x_1 , \quad (30)$$

$$b_2 = z_1 y_2 - z_2 y_1 , \quad (31)$$

and

$$c = y_1 x_2 - y_2 x_1 . \quad (32)$$

Solving the set of simultaneous equations in terms of these variables yields the following expression for the elevation angle of arrival

$$\psi = \sin^{-1} \left(\frac{a_1 b_1 + a_2 b_2 + c \sqrt{b_1^2 + b_2^2 + c^2 - a_1^2 - a_2^2 - a_3^2}}{b_1^2 + b_2^2 + c^2} \right) \quad (33)$$

and for the azimuth angle of arrival

$$\phi = \tan^{-1} \left(\frac{a_1 - b_1 \sin \psi}{-a_2 + b_2 \sin \psi} \right) . \quad (34)$$

C. IONOSPHERIC CONSIDERATIONS

1. Propagation Modes

The ionosphere plays an essential role in the determination of target location when using an HFDF SSL system. The ionosphere is the region of the atmosphere composed of gases which are primarily ionized by solar radiation in the ultra-violet to

X-ray range. It extends from about 50 km to 1000 km in altitude and is an amorphous, nonhomogeneous, and extremely turbulent plasma [Ref. 3].

The ionosphere is usually modeled as a series of layers that vary in height and electron density. For all practical purposes 3 layers have been identified in the ionosphere: D, E, and F.

The D-layer extends from 50 km to 90 km and exists only during daylight hours. It is an absorptive layer, where the lower HF frequencies are attenuated more than higher frequencies.

The E-layer extends from 90 km to 130 km and although at night it is quite weak, it is considered a permanent layer. During daylight it is used for short-to-medium range propagation.

In the E-region height at about 100 km, a highly ionized layer occurs at various times known as the Sporadic E (Es) layer. This transient layer of short duration appears during daylight allowing unexpected propagation of high frequencies.

The F-layer is the most important layer for long distance communications. It exists at 130 and 500 km altitude and is a permanent layer. Throughout the year in low latitudes and during the summer in high latitudes, the F region splits into two layers, F_1 and F_2 , after sunrise.

The lower layer, F_1 , is at a height of approximately 200 km and is present only during daylight hours. The higher layer, F_2 , occurs at approximately 300 km and has the highest ionization density.

A plot of ionospheric electron density versus height is shown in Fig. 5.

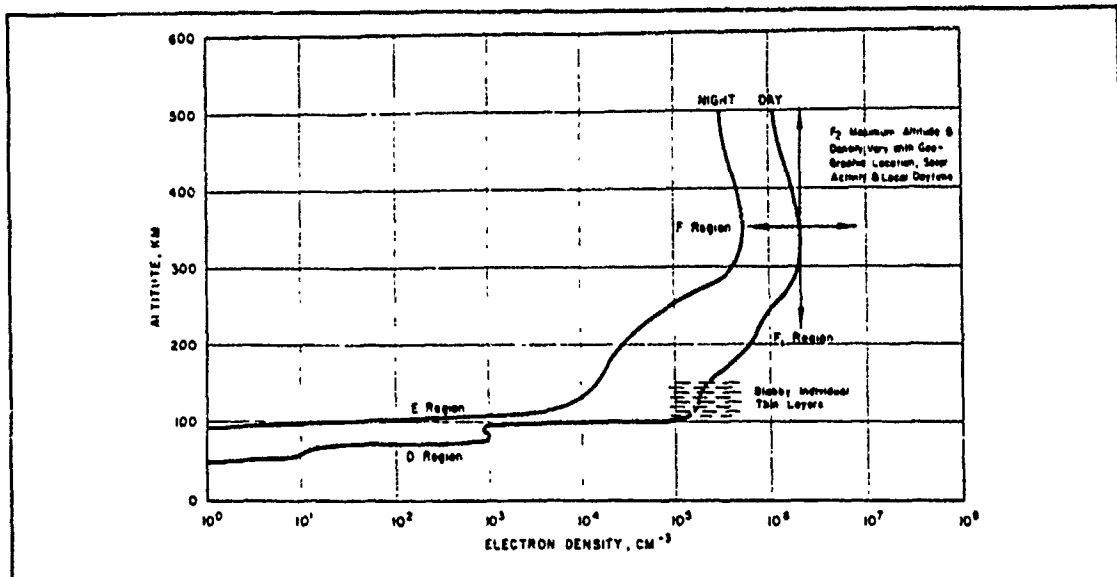


Fig. 5.- Electron Density of the Ionosphere.

During daylight, the lower frequencies of the HF band are highly attenuated by the D-layer and efficient long distance communication is in the range of 10 to 20 MHz. At night, higher frequencies are not reflected from the weaker nighttime ionosphere and the lower portion of the HF band (2 to 10 MHz) must be used.

To comply with the tactical scenario the HFDF SSL system must then be able to cover 2 to 20 MHz.

The term "propagation mode" refers to the path of the signal through the ionosphere and the number of reflections (hops) that occur between the transmitter and receiver (emitter to HFDF SSL in this case). Propagation modes are identified by numbers and letters which represent the number of hops and the name of the layer where each reflection occurs.

Examples

$2F_2$ = A path with 2 reflections from the F_2 -layer.

F_2Es = One reflection from the F_2 -layer followed by a reflection from the Sporadic E-layer (also called an N-type reflection).

F_2EsF_2 = One reflection from the F_2 -layer followed by a reflection from the Sporadic E-layer and then another F_2 -hop (called an M-type reflection).

Proper identification of the mode of propagation is critical for HFDF SSL operation. Incorrect path assumptions create errors in final position determination.

2. Ionospheric Tilts and other Effects

Variations of the ionization gradient with geographical position are usually called "ionospheric tilts". Because the effective tilt of an ionospheric layer depends on the depth of penetration of a ray into the layer, a tilted layer should not be considered as a tilted mirror [Ref. 2]. The tilt depends on the layer as well as the ray path and varies from ray to ray. Ionospheric tilts can be lateral or longitudinal with respect to the path between the emitter and the HFDF SSL.

Several methods are proposed for obtaining information on ionospheric tilts and for correcting their effects on azimuth and elevation angles measured at an HFDF SSL. The Chapman model and numerical maps based on monthly median predictions of ionospheric parameters are two methods that do not require real-time measurements. The use of a "check" transmitter of known position, the direct measurement of local tilt by a pulsed sounder and doppler measurements or ionospheric profiles from vertical or oblique incidence sounders provide real-time information on tilts. A more detailed treatment of

each of these methods is found in Ref. 2. The DF system in this study uses a vertical incidence sounder to determine tilt characteristics of the layer of interest.

For a single isolated propagation mode, the ionosphere acts as a mirror and the spread of rays within a given mode is quite small. When complex mode structures are present they produce large number of ray paths. The received signal is then the vector sum of randomly varying ray components and the resulting signal intensity varies randomly. This effect is known as fading and is present in both short and long range propagation paths, but for this study only the 300 to 500 km paths are considered. In addition to fading, sky waves can exhibit changes in direction of arrival, both in azimuth and in elevation [Ref. 4]. These changes can be rapid fluctuations generally attributed to lack of homogeneity of the ionosphere, or long-term fluctuations due to large scale ionospheric disturbances. Small variations in the characteristics of the ionosphere can arise from traveling ionospheric disturbances (TID) and from other temporal irregularities.

Time averaging can be used to counteract signal variations and to resolve the dominant propagation mode when using a phase-interferometer HFDF SSL. The DF system of this study uses a sliding window of 20 frames which is the average observation over a one-second period [Ref. 5].

The earth's magnetic field is another important factor to consider in HFDF SSL operation since it modifies the phenomena of ionospheric refraction. It "splits" an incident wave into two polarization components, each with different propagation velocities and attenuations. These components are called the ordinary and extraordinary waves. The extraordinary wave suffers much higher absorption, thus useful sky wave propagation

almost always takes place through the ordinary wave [Ref. 6]. For transverse or quasi-transverse propagation, the usual mode for HF sky-wave propagation except near the magnetic poles, the critical frequency of the ordinary wave is the same as that calculated neglecting the earth's magnetic field [Ref. 6]. Only the reflected ordinary wave must be considered in this study.

The earth's magnetic field also changes the polarization of the reflected wave with respect to the incident wave. A plane-polarized incident wave is converted into an elliptically-polarized reflected wave. When the direction of propagation forms an acute angle with the direction of the magnetic field, the reflected ordinary wave will be left-hand elliptically polarized, and the extraordinary wave right-hand elliptically polarized. If the angle is obtuse, the reverse case is true. Generally in the northern hemisphere the downcoming ordinary wave is polarized in the left-hand sense and in the southern hemisphere it is polarized in the right-hand sense [Ref. 6]. The incoming sky wave will then have vertical and horizontal electrical field components and since the interferometer compares the signal received by two identical antennas, the polarization of the antennas is not a critical issue. Antenna polarization can become an important issue if both receive antennas are not correctly aligned with each other or if the polarization characteristics are not the same.

An extensive analysis of polarization error of a two element interferometer has appeared in the Russian literature [Ref. 7]. These studies show that significant phase errors, approaching 180° , can occur independent of spacing error, when the antennas do not have identical polarization characteristics.

D. HFDF SSL VERTICAL TRIANGULATION

The goal of an HFDF SSL is to determine the position of a transmitter with a moderate degree of accuracy and over a reasonably wide range of distances, operating frequencies and ionospheric conditions. From measurements of the angle of arrival of a signal position fixing is achieved using a technique called vertical triangulation. Utilizing a single station makes the system simple and inexpensive to install and maintain, compared to a network of DF stations.

Appleton and Barnett first used vertical triangulation in HF propagation in 1924 [Ref. 8], using the geometry of Fig. 6. They applied a thin-ionosphere approximation model, assuming a mirror reflection at point L. From the distance, d , and elevation angle of arrival, ψ , they deduced the height of the ionosphere.

This procedure also assumes a uniform ionosphere, a flat earth and straight ray paths. Later studies have demonstrated that the structure of the ionosphere is not uniform. Refraction bends ray paths and the effect of curvature of the earth must be included for long distances.

The HFDF SSL problem of emitter location is solved from receiver site information. Knowing the elevation and azimuth angles of arrival of the signal and the height of the ionosphere, the bearing and distance to the emitter are determined. For accurate measurements, the effects of ray refraction in the atmosphere, earth curvature and ionospheric structures should be included. Ray path determination is simple up to the point where rays enter the ionosphere. The exit path from the ionosphere to the HFDF SSL station depends on the electron density distribution.

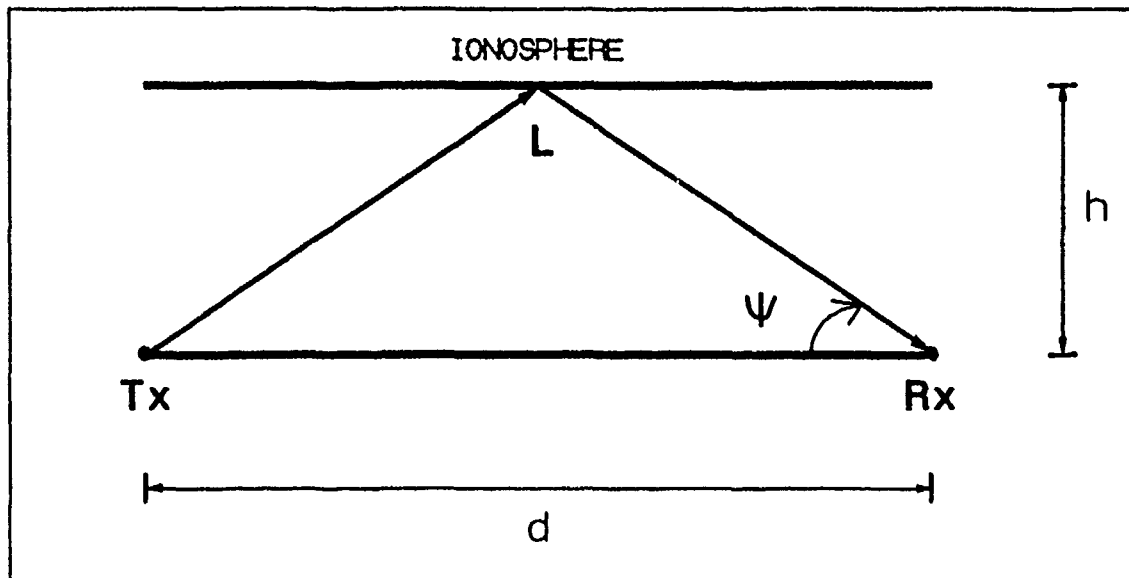


Fig. 6.- Vertical Triangulation Using Appleton's Model.

If this distribution were accurately known, ray tracing methods for calculating emitter-receiver distance are available as computer codes. Unfortunately, the electron density structure of the ionosphere is rarely known with sufficient precision to determine the amount of ionospheric penetration which has occurred.

A vertical sounder can be used to determine the virtual height (h') of the apparent reflection point as shown in Fig. 7. With the virtual height and the angle of arrival of the incoming signal, vertical triangulation is used to calculate distance to the emitter.

The HFDF SSL system under study uses a sounder to obtain ionospheric information for the tactical scenario developed in Chapter I. With 300 to 500 km ranges expected, vertical triangulation can be performed using the flat-earth, flat-ionosphere approximation [Ref. 9].

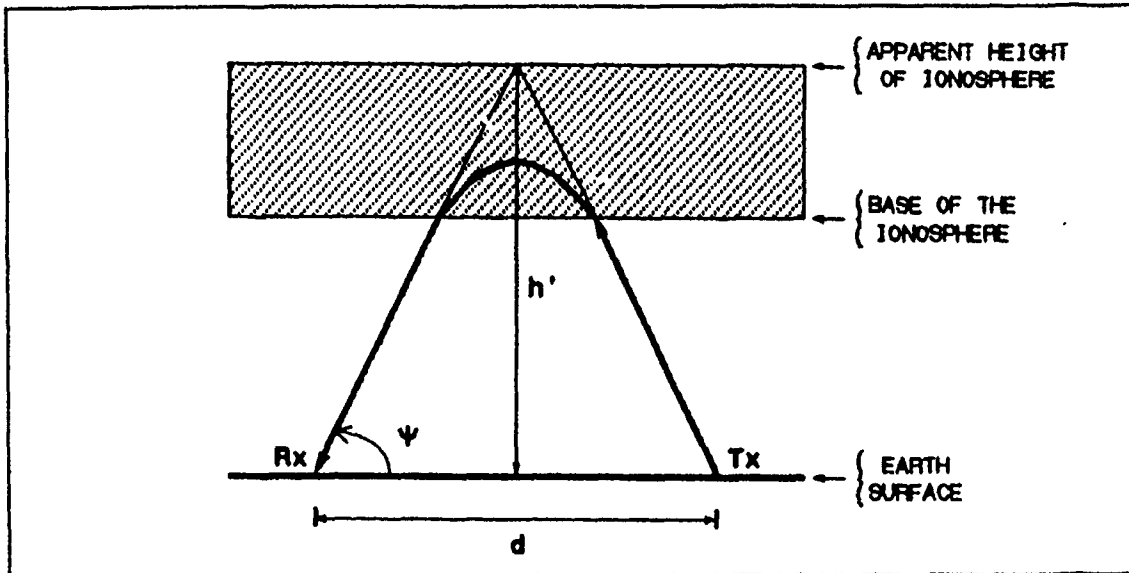


Fig. 7.- Signal Geometry for the Flat Earth Flat Ionosphere Approximation.

The distance to the emitter is:

$$d = \frac{2(h')}{\tan \psi} , \quad (35)$$

where

h' = virtual height of the ionosphere,

d = distance between emitter and receiver and

ψ = elevation angle of arrival of the signal.

From this expression a family of curves of virtual height versus elevation angle for various distances are produced in Fig. 8.

E. TYPICAL HFDF SSL PATHS

Based on ionospheric considerations of this chapter and the tactical scenario of Chapter I, the characteristics of typical HFDF SSL paths can be established.

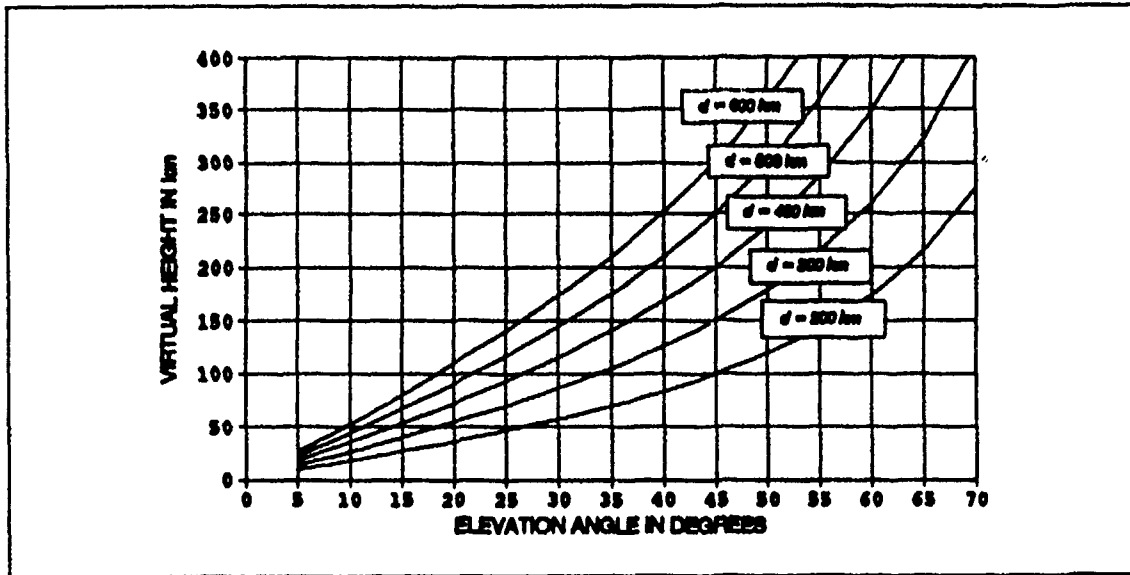


Fig. 8.- Transmission Curves Parametric in Distance (d) for Flat-Earth Flat-Ionosphere.

The objective of this research is to analyze the effects of errors introduced in the HFDF SSL process by the antenna array. For this investigation the assumptions are (1) the virtual height of the ionosphere is known and (2) the effects of ionospheric tilts can be accounted for.

To determine the performance of the antenna arrays, values of the minimum and maximum elevation angles of arrival of the incoming waves must be determined. Using the transmission curves of Fig. 8, for virtual heights of the E-layer and the F_2 -layer at distances between 300 and 500 km, it is seen that elevation angles of arrival vary from 25° to 65° .

III. NEC MODELING

A. BACKGROUND

The Numerical Electromagnetics Code (NEC) is designed for modeling of the electromagnetic response of general structures. NEC was developed by the Lawrence Livermore National Laboratory for the Naval Ocean Systems Center (NOSC). It uses an electric field integral equation to model wire-like objects, and a magnetic field integral equation to model closed surfaces with time harmonic excitation [Ref. 10]. For structures containing both wires and surfaces the two equations are coupled together.

NEC solves the integral equations numerically via the Method of Moments. Finitely conducting ground effects can be included in the model, in addition to free space and perfect ground conditions. Two alternative models are provided for finitely conducting ground. The Reflection Coefficient Approximation uses image fields modified by Fresnel reflection coefficients and is valid for structures located at least 0.1 wavelengths above ground. The Sommerfeld integral formulation for the near field at the interface provides an accurate solution for elements above, below, or penetrating the ground, but with a substantial cost in computational resources.

NEC permits excitation by voltage sources on the structure or by incident plane waves of specified polarization. Outputs include radiation patterns, power and directive gains, feed point impedances, ohmic losses, efficiency, wire and surface currents and

charge density, maximum couplings, near E and H fields, scattering cross section, and average gains. A detailed description of the code is found in Ref. 11.

B. SWRI HFDF SSL SYSTEM DESCRIPTION

The HFDF SSL system modeled in this thesis employs the phase-interferometer technique. A two orthogonal-baseline antenna array determines the three-dimensional angle of arrival of a signal as described in Chapter II. The system has been developed by SWRI [Ref. 12], and is designed to be a real-time computer-controlled HFDF SSL. It provides DF capabilities for ground and sky wave HF propagation for the 2 to 30 MHz frequency range at ranges up to 1100 km. The system is intended for tactical/portable operation. The system block diagram is shown in Fig. 9. Three main components can be identified as:

- (1) two, seven-element interferometer antenna arrays,
- (2) automatic DF acquisition, processing and display system and
- (3) ionospheric sounder system.

This research study will concentrate on the analysis of the two antenna arrays. The DF processing algorithm used by SWRI is used in the evaluation of the effects of errors induced by the antenna arrays under different ground conditions.

1. Low Band Antenna Array

The low band antenna array is intended to cover 2 to 10 MHz by seven identical vertical, square crossed loops. The antenna elements are placed in an "L" shaped array as shown in Fig. 10. Each orthogonal arm of the array contains three antennas

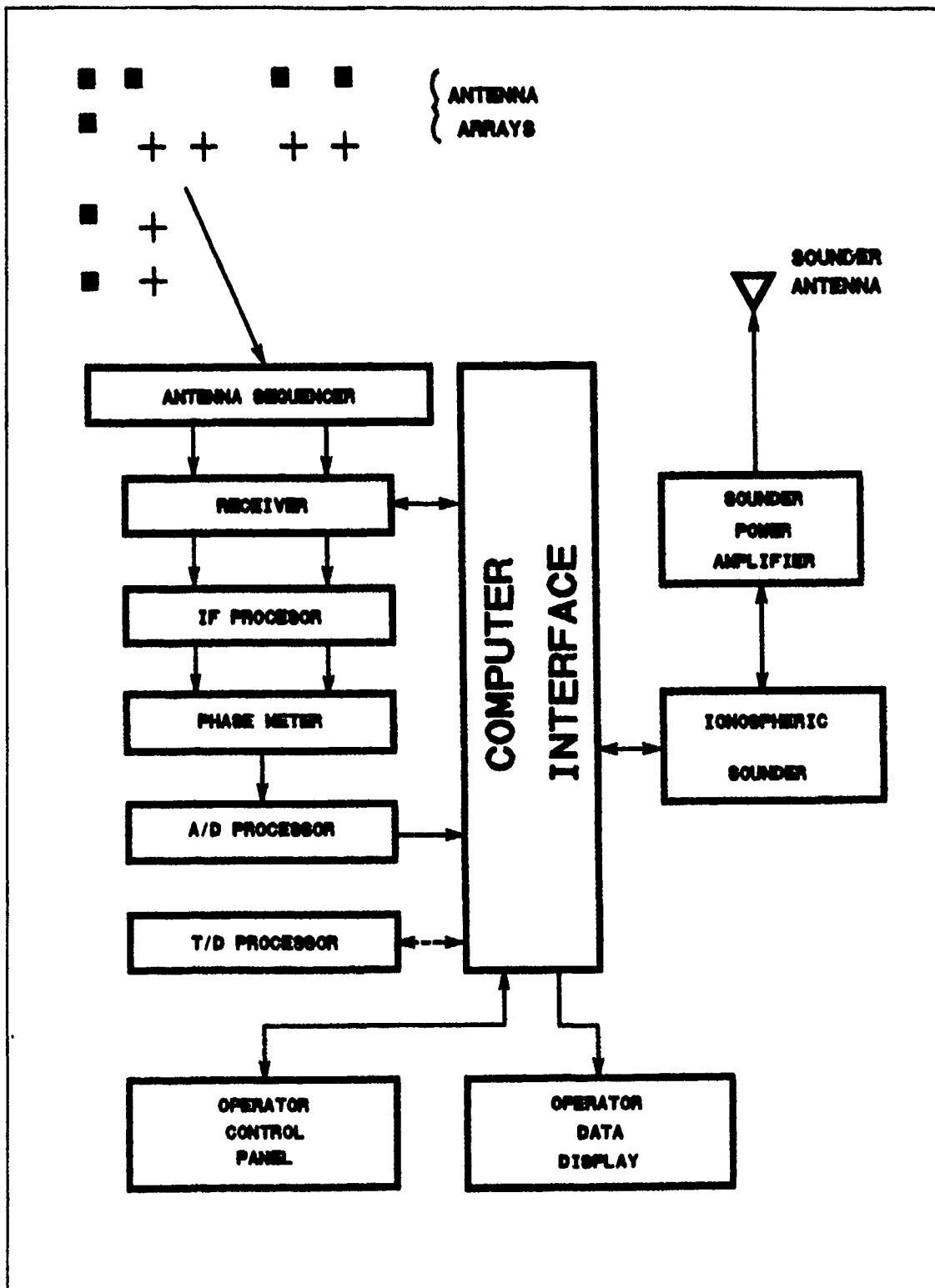


Fig. 9.- SWRI Phase Interferometer Block Diagram.

which are placed along a line at different distances. A central antenna (reference) is located on the vertex of the array and allows multiple baselines to be selected on the interferometer. It is diagonally symmetric, that is, each baseline on one arm (formed by the central reference antenna and one of the antennas of the arm) has an image on the other arm. Because of this characteristic the system can compare the phase of one baseline with its equivalent on the other arm and by applying phase-interferometer techniques it can find the angle of arrival of a signal.

The shortest baseline of the low band array is 13 meters long, less than one-half wave length at 10 MHz (15 meters). This is the highest frequency of the array for unambiguous operation. The characteristics of the low band elements are:

Antenna type:	Crossed Loops
Orientation:	Vertical
Element shape:	Square loop
Frequency range:	1.5 - 10 MHz
Size:	5 foot / side
Number of elements:	2 orthogonal loops
Height above:	0.15 m
Vertical distance between elements:	0.05 m
Cross section:	0.05 m
Material:	Aluminum and fiberglass

The geometry of a single element of the array is detailed in Fig. 11.

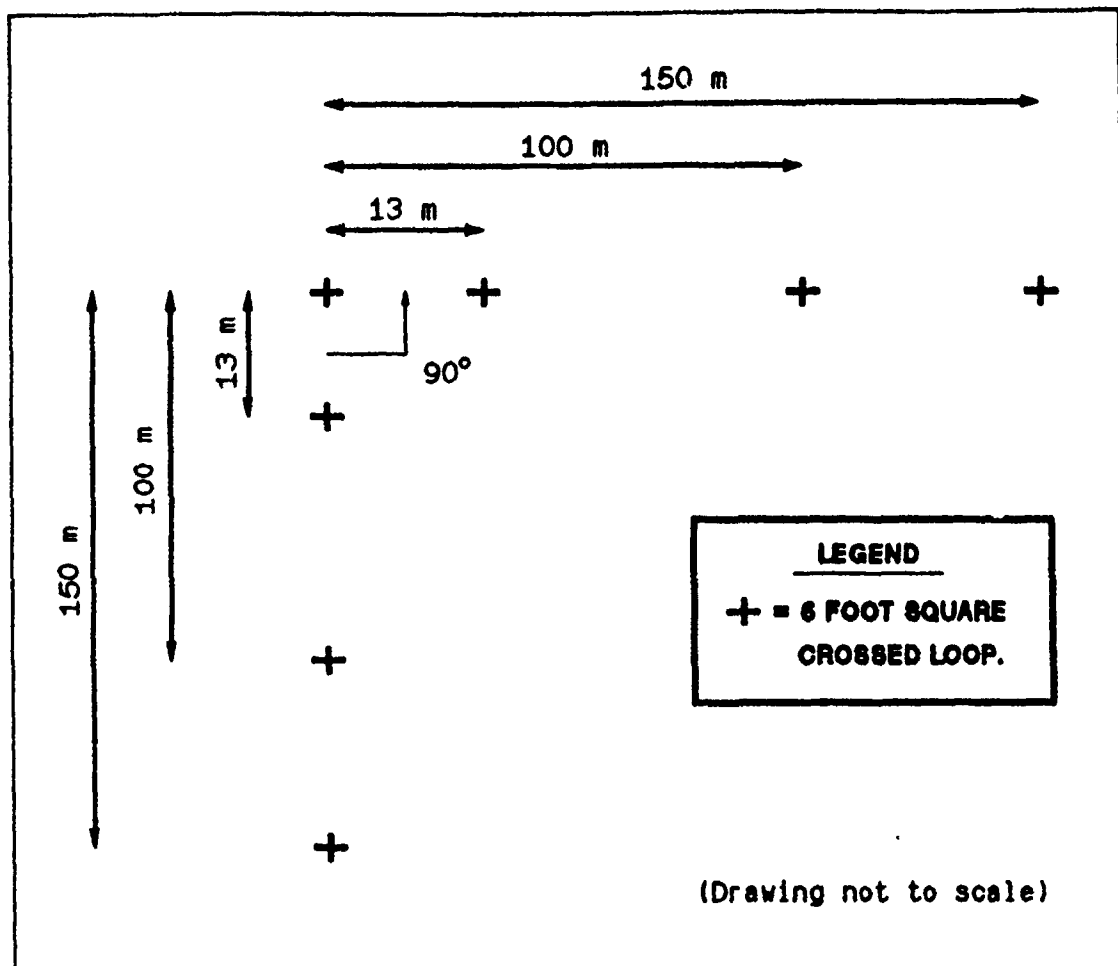
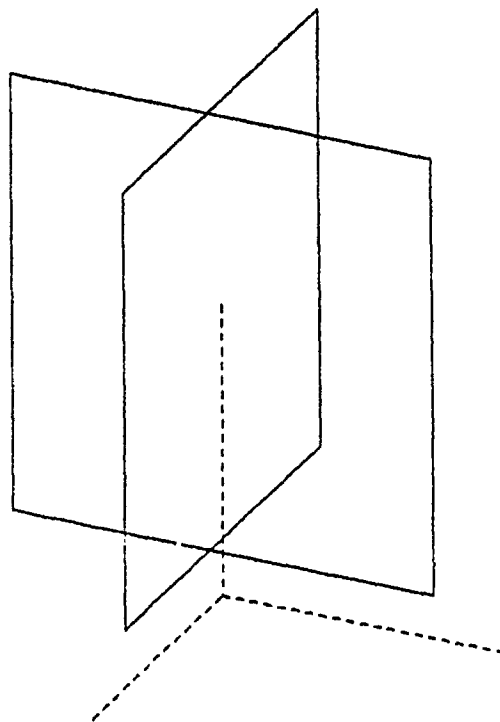


Fig. 10.- Interferometer Low Band Antenna Array.

2. High Band Antenna Array

The high band antenna array, designed for 10 to 30 MHz has seven identical, vertical monopoles, placed over a wire mesh ground screen (counterpoise). It is also an "L" shaped array but with different dimensions than the low band one. It is also diagonally symmetric as shown in Figure 12.

CROSSED SQUARE LOOP ANTENNA



THETA = 65.00 PHI = 25.00 ETA = 90.00

Fig. 11.- 5 Ft Square Crossed Loop.

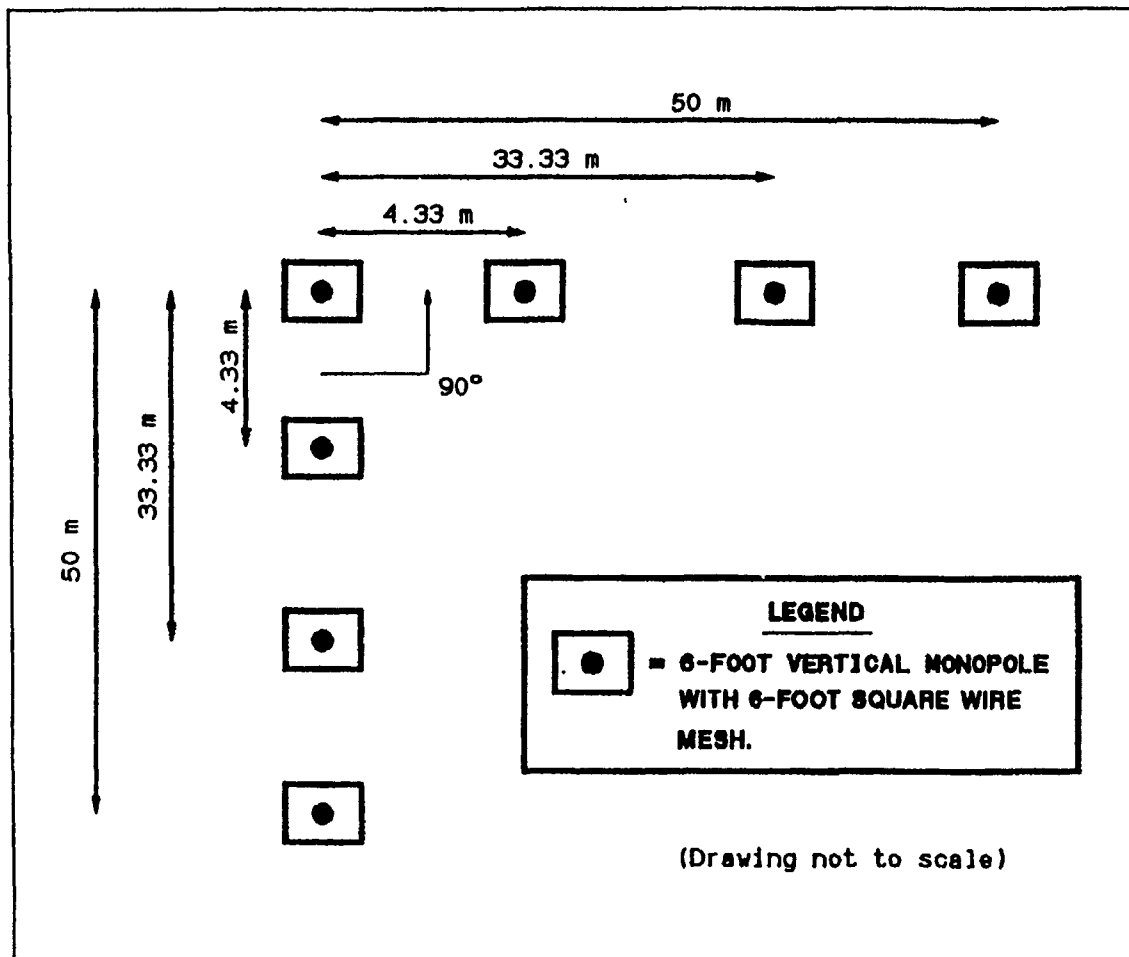


Fig. 12.- Interferometer High Band Antenna Array.

The shortest baseline of the array is 4.33 m, and is used to resolve ambiguities. This is less than one-half wavelength at 30 MHz, the highest frequency of operation. The characteristics of the high band array elements are

Antenna type:	Monopole
Orientation:	Vertical
Frequency range:	10 - 30 MHz
Size:	6 feet

Height over ground:	0.15 m
Cross section:	0.05 m
Material:	Aluminum fiberglass
Ground screen:	6 x 6 feet grid with 6 inches spacing
Screen radials:	6 feet radials every 45°
Radial wire diameter:	0.01 m

The shape of a single element of the high band antenna array is shown in Fig. 13.

C. COMPUTER MODEL DEVELOPMENT

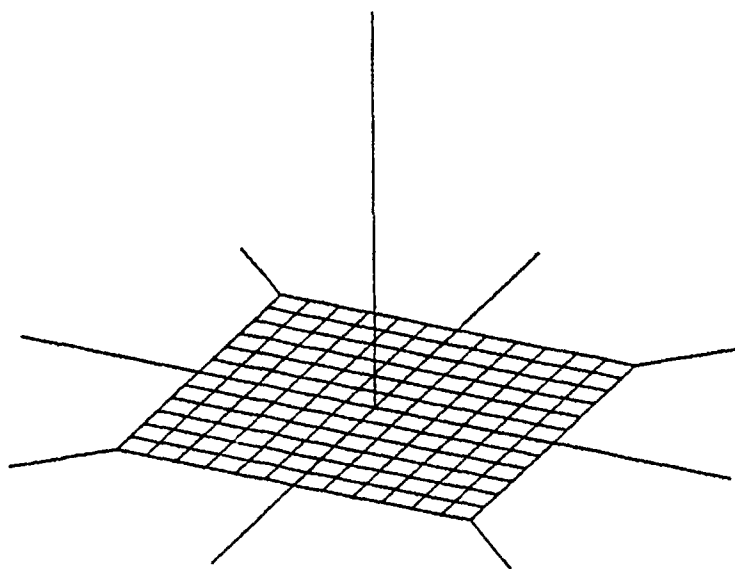
1. Dimensions Considerations

The first step in developing a numerical model of the two antenna arrays is to define the geometry of the elements and their physical location within the array.

The second step is selecting the length of wire segments used to model each antenna structure within the guidelines of the NEC code specifications. Since current is computed at the center of each segment, the length of the segments partially determines the resolution of the currents in a NEC model. Critical regions of the antenna require smaller segment lengths.

The maximum segment length recommended in NEC is $< 0.1 \lambda$. Additionally, the NEC segment length for 32-bit double precision applications is $> 10^{-8} \lambda$.

VERTICAL MONOPOLE WITH WIRE MESH



THETA = 65.00 PHI = 25.00 ETA = 90.00

Fig. 13.- 6 Ft Monopole With 6 Ft Sq. Wire Mesh and Radials.

Applying these two constraints to 2-20 MHz the segment length limits were calculated as:

<u>Frequency</u>	<u>Wavelength</u>	<u>Maximum</u>	<u>Minimum</u>
2 MHz	150 m	< 15 m	$0.15 * 10^{-5}$ m
5 MHz	60 m	< 6 m	$0.6 * 10^{-6}$ m
10 MHz	30 m	< 3 m	$0.3 * 10^{-6}$ m
15 MHz	20 m	< 2 m	$0.2 * 10^{-6}$ m
20 MHz	15 m	< 1.5 m	$0.15 * 10^{-6}$ m

From these calculations for the worst case conditions, the segment lengths should be within the range of 0.15×10^{-5} m to 3 m for the low band array and 0.3×10^{-6} m to 1.5 m for the high band array. The model was adjusted to verify that it contained the minimum number of segments to reduce computation time, while maintaining the segment lengths within the limits of acceptable calculation accuracy. The segment lengths of the model were selected to be from 0.51 m to 1.72 m for low band and from 0.15 m to 0.91 m for high band. In addition, segment lengths were selected to comply with a NEC restriction for errors of less than 1% as

$$\text{Segment length} / \text{wire radius} > 2.$$

Segment length limits had previously been selected so dimensions of the radius of all the wires in the model were held to

$$\text{low band} < 0.25 \text{ m and}$$

$$\text{high band} < 0.07 \text{ m.}$$

The maximum wire radius used in the computer model was 0.05 m for both arrays, less than the NEC requirement above. Also, when modeling structures over ground NEC imposes a restriction for wires placed horizontally close to ground as

$$(h^2 + a^2)^{1/2} > 10^{-6}\lambda, \quad (36)$$

where

h = height of the horizontal wire over ground,

a = wire radius and

λ = wavelength.

Only the high band antenna array contained horizontal wires close to ground (the wire mesh). For these conditions and 20 MHz, the worse-case frequency, the wire height of the mesh was set 0.001 m above ground to satisfy NEC guidelines for horizontal wires near ground.

2. Symmetry Considerations

NEC includes capability for exploitation of structure symmetry to simplify model development and to reduce computational requirements. Both arrays exhibit partial diagonal symmetry and by using the Numerical Green's Function (NGF) option of NEC, the symmetric portions of the structures can be evaluated and the factored interaction matrix saved in a file for later use. The complete solution can be obtained without repeating calculations for the symmetric data on file. This feature is particularly useful for the high band model because of the large number of segments involved in modeling the wire mesh for every monopole of the array.

3. Ground considerations

The Sommerfeld method of ground interaction was used to provide an accurate solution for the wires close to ground in both arrays. "Poor" ground and "good" ground parameters were used in addition to free space and perfect ground to thoroughly cover effects which were influenced by installation conditions. The ground constants chosen are the following

GROUND CONDITION	CONDUCTIVITY (σ)	RELATIVE DIELECTRIC CONSTANT (ϵ_r)
Good Ground	0.01 mhos/m	30
Poor Ground	0.001 mhos/m	5

These ground parameters were used with a separate program called SOMNTX to generate a ground interaction data file, containing values required by NEC when using the Sommer-feld option.

D. NEC DATASETS

The NEC datasets constructed for the high and low band antenna arrays used by the HFDF SSL phase-interferometer are listed in Appendix A.

IV. PERFORMANCE OF THE ANTENNAS

An HFDF SSL system is always used to analyze the performance of the antennas in the receive mode so the Reciprocity Theorem was used to characterize the arrays for all performance parameters except feed point receive-current phases. When calculating angle of arrival, the more resource-consuming receive mode of excitation had to be used.

A. ANTENNA INPUT IMPEDANCE

Input impedance is an important performance parameter of an antenna and because its value depends on the electrical configuration and dimensions of the antenna it provides an indication of the validity of a numerical antenna model.

To verify the accuracy of the crossed-loop NEC model the impedance from NEC was compared to values calculated by a theoretical method.

In the 2 to 10 MHz frequency range, the 5 foot square loops are a small antenna compared to the wavelength. These small loops behave as if they were "magnetic dipoles" with highly inductive input impedance. The method proposed by Ref. 13 was used to calculate the input impedance of the vertical square loops. This method assumes that the square loop can be analyzed as a shorted transmission line of wire radius which is very small compared to the loop dimensions and to the wavelength. The reactive part of the input impedance is a function of the loop perimeter wire radius. Thus an equivalent transmission line shorted at one end can be used to determine its impedance. Using this

model, the input impedance of the shorted lossless transmission line is equal to the reactive part (X_{in}) of the input impedance of the loop as

$$X_{in} = jZ_0 \tan(kl) , \quad (36)$$

where

k = wave number or propagation coefficient and

l = transmission line length.

Without losing generality, the transmission line length, l , can be approximated as half the perimeter and the characteristic impedance of the transmission line (Z_0) then becomes

$$Z_0 = 276 \log \left(\frac{s}{r} \right) , \quad (37)$$

where

l = (loop perimeter)/2,

s = (loop area)/ l and

r = wire radius of the loop.

Applying the preceding formulas at 5 MHz, a wire radius of 0.05 m, and a loop side length of 1.524 m,

$$l = \left(\frac{1.524 \times 4}{2} \right) = 3.048 \text{ m} , \quad (38)$$

$$s = \left(\frac{1.524^2}{3.048} \right) = 0.762 \text{ m} \quad (39)$$

and

$$k = \left(\frac{2\pi}{\lambda} \right) = \left(\frac{2\pi}{60} \right) = 0.104 \text{ m} . \quad (40)$$

Then

$$Z_0 = 276 \log \left(\frac{0.76}{0.05} \right) = 326.5 \text{ Ohms} \quad (41)$$

and

$$\begin{aligned} X_{in} &= j (326.5) \tan [0.104 \times 3.04] \\ &= j 107.9 \text{ Ohms.} \end{aligned} \quad (42)$$

The NEC value for the imaginary part of the input impedance was 110.5 Ohms, which agrees well with the approximate theory.

For the resistive part of the loop input impedance the least squares technique of Ref. 13 yields

$$R_{in} = a \left[\tan \left(\frac{k p}{2} \right) \right]^b \quad (43)$$

where

k = wave number or propagation coefficient and

p = perimeter of the loop.

In addition, $a = 1.126$ and $b = 3.95$ for a square loop. Using this formula, $R_{in} = 0.014$ Ohms. The resistive part of the input impedance from a NEC calculation agrees well at 0.013 Ohms.

The high band antenna array is composed of seven vertical monopoles, each one with an underlying wire mesh. To verify the accuracy of the NEC model, the input impedance of a monopole of the same characteristics was calculated and compared to the NEC result.

The input resistance of an ideal monopole over perfect ground is half the radiation resistance of a dipole whose length is twice the monopole height. From Ref. 14 the radiation resistance of a short dipole is

$$R_{rad} = \frac{2 P_{rad}}{|I_0|^2} = 20 \left(\frac{L \pi}{\lambda} \right)^2 . \quad (44)$$

Since the height of the vertical monopole is 1.83 m, the equivalent length of its dipole counterpart is 3.66 m. By using this length (L) and a frequency of 15 MHz,

$$R_{rad} = 20 \left(\frac{3.66 \pi}{20} \right)^2 = 6.6 \text{ Ohms} . \quad (45)$$

The radiation resistance of the monopole is thus approximately 3.3 Ohms, assuming a lossless case. The value of the input resistance of the monopole calculated by NEC code was 3.74 Ohms, close enough to be considered adequate.

B. SMITH CHART INPUT IMPEDANCE ANALYSIS

An important verification of the behavior of an antenna through a frequency range, is to analyze its input impedance using the Smith Chart. When plotted on a Smith Chart, the input impedance of the antennas should show smooth variation with clockwise rotations and describe a smooth curve, as frequency is increased over the operating range.

The model of the electrically small crossed loop was first tested for the 2 to 5 MHz range for good ground ($\epsilon=30$ and $\sigma=0.01$), poor ground ($\epsilon=5$ and $\sigma=0.001$), perfect ground and free space conditions. The results of the different runs are shown in Table B-1 of Appendix B. Each set of data was then normalized to the lowest value of its set and the resultant input impedances plotted on a Smith Chart.

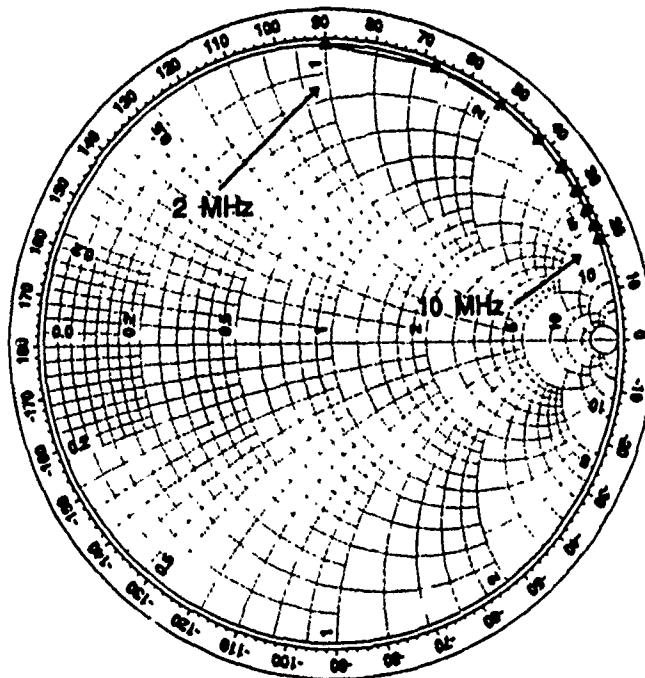
As shown in Fig. 14 and Fig. 15, the input impedances show smooth variation and describe highly reactive curves on the Smith Chart, confirming that the NEC results of the small crossed loop impedance are as expected.

Next, the NEC model of the vertical monopole with wire mesh was used to construct a Smith Chart of input impedance for 10 to 20 MHz for free space, good ground, poor ground, and perfect ground conditions. The results are in Table B-2 of Appendix B. The resulting Smith chart plots are shown in Fig. 16 and Fig. 17 and are as expected.

C. AVERAGE POWER GAIN

Another parameter used to verify numerical antenna models is the average power gain of the antenna. Since it accounts for antenna efficiency, hence radiation resistance,

CROSSED LOOP ON FREE SPACE, 2 TO 10 MHz



CROSSED LOOP OVER PERFECT GROUND, 2 TO 10 MHz

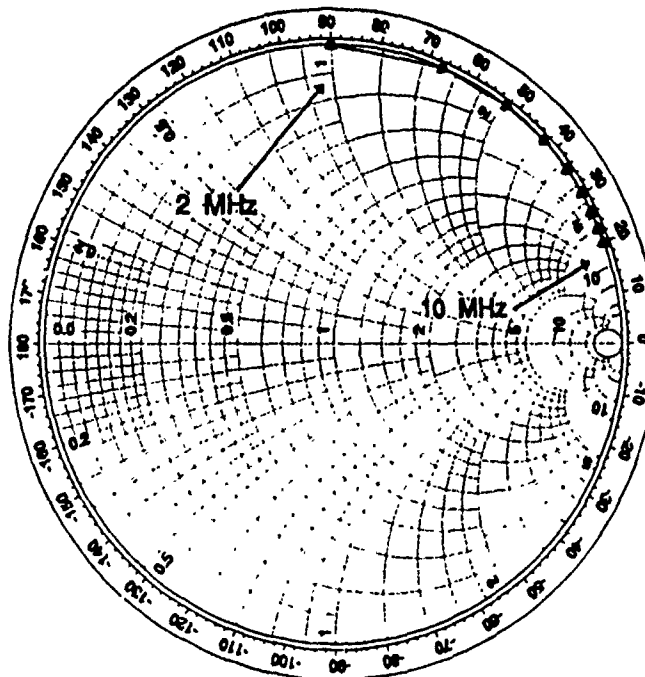
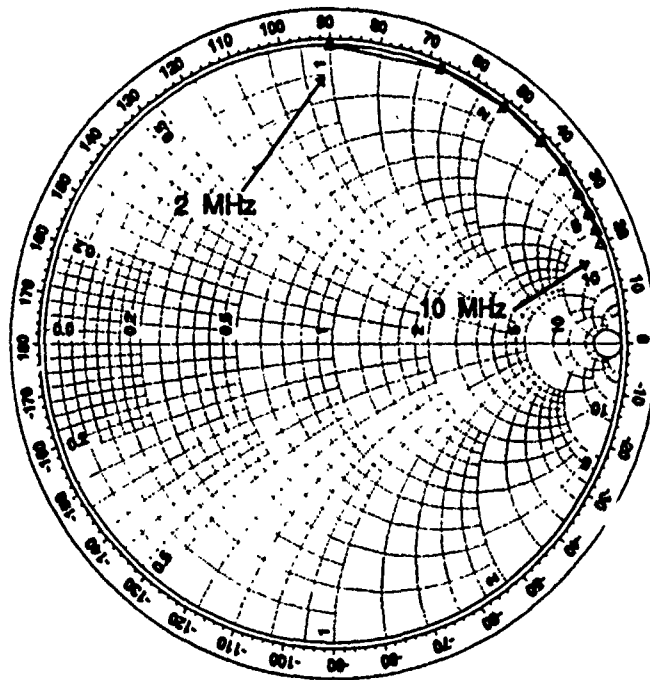


Fig. 14.- Crossed Loop Input Impedance (Free-Sp; Perfect-Gr).

CROSSED LOOP OVER GOOD GROUND, 2 TO 10 MHz



CROSSED LOOP OVER POOR GROUND, 2 TO 10 MHz

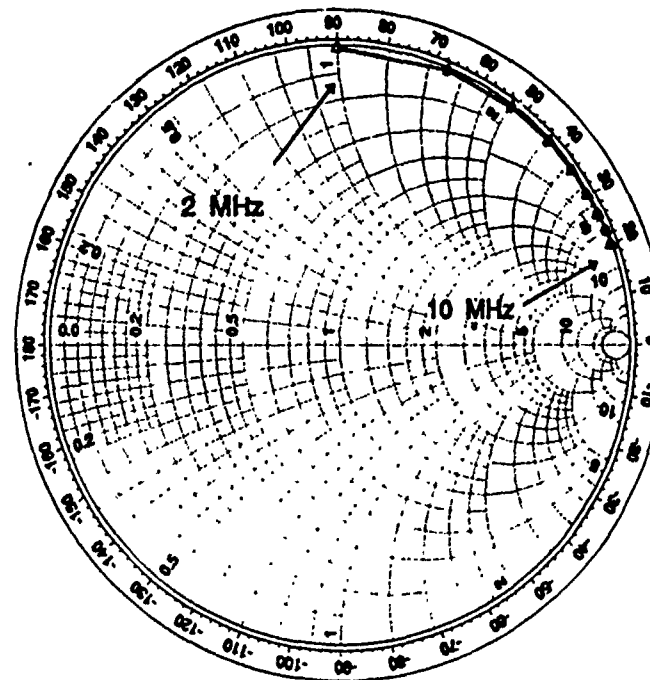
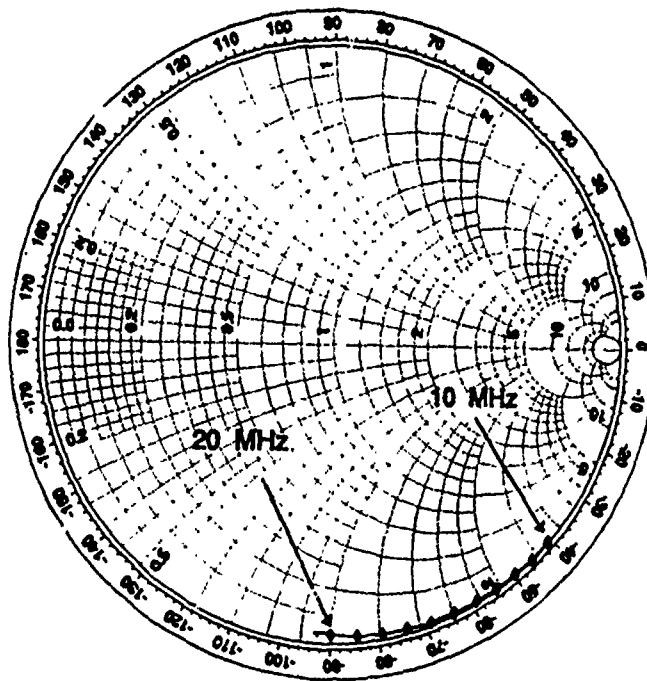


Fig. 15.- Crossed Loop Input Impedance (Good and Poor Ground).

MONOPOLE ON FREE SPACE , 10 TO 20 MHz



MONOPOLE OVER PERFECT GROUND , 10 TO 20 MHz

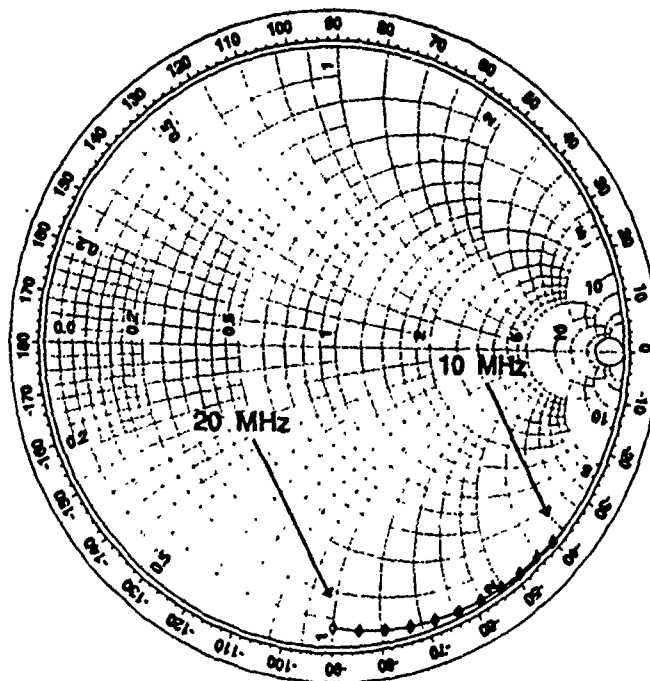
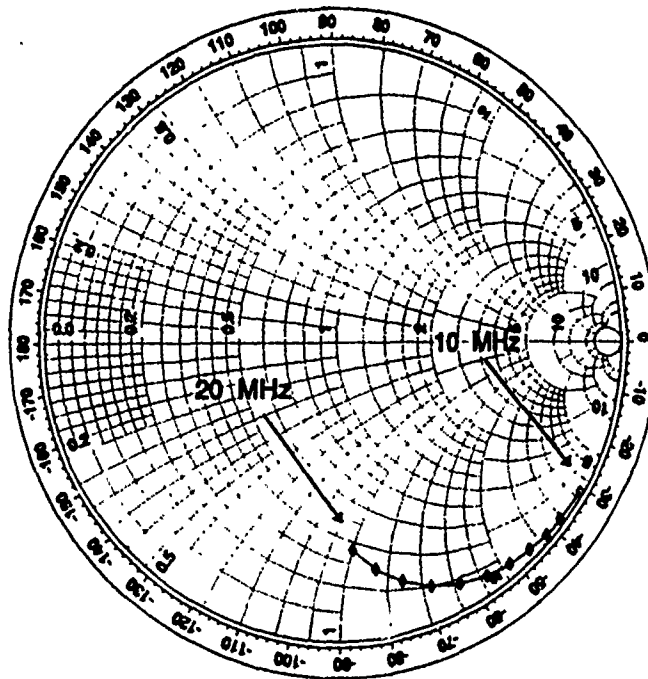


Fig. 16.- Monopole Input Impedance (Free Sp. and Perfect Gr.).

MONOPOLE OVER GOOD GROUND , 10 TO 20 MHz



MONOPOLE OVER POOR GROUND , 10 TO 20 MHz

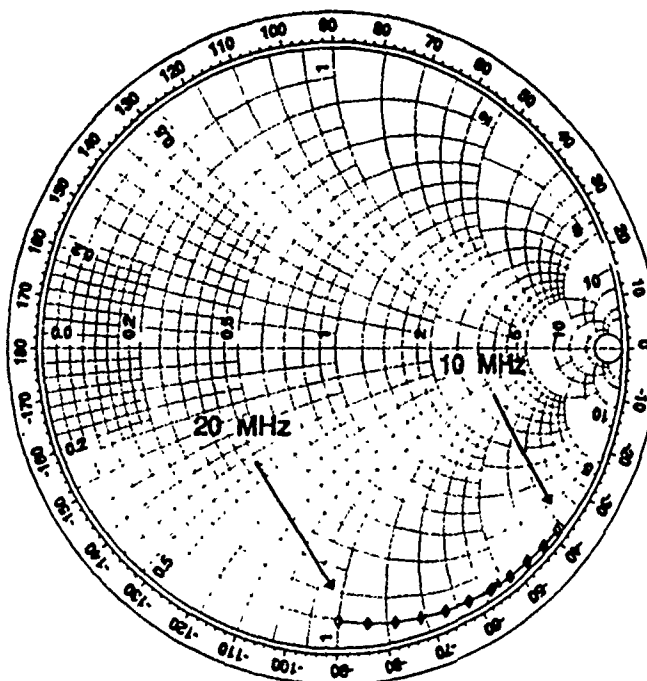


Fig. 17.- Monopole Input Impedance (Good and Poor Ground).

it is a measure of validity of current distribution at the feed point.

The average power gain is defined as the integral of the antenna power gain per unit solid angle,

$$G_{avg} = \frac{1}{\Omega} \int_{\Omega} G_p d\Omega , \quad (46)$$

where

G_{avg} = average power gain,

G_p = antenna power gain and

Ω = solid angle.

When the solid angle is 4π , the average gain can be expressed as

$$G_{avg} = K \left(\frac{P_{rad}}{P_{in}} \right) , \quad (47)$$

where P_{rad} is the total power radiated, P_{in} is the input power at the antenna terminals,

and K is 1 for free space, 2 for perfect ground and between 0 and 1 for lossy ground. P_{rad}

can, in turn, be found by integrating the complex pointing vector, $S = \frac{1}{2} (E \times H^*)$,

as

$$P_{rad} = \frac{1}{2} \text{Re} \iint (E \times H^*) ds , \quad (48)$$

where

E = electric field intensity and

H^* = complex conjugate of the magnetic field intensity.

In the far field,

$$P_{rad} = \frac{R^2}{2} \int_{4\pi} \frac{|E^2|}{\eta} d\Omega \quad \text{for } R \rightarrow \infty, \quad (49)$$

where

η = intrinsic impedance of the medium and

R = distance.

The input power at the antenna terminals can be found by

$$P_{in} = \frac{1}{2} \operatorname{Re} [V_0 I^*(0)], \quad (50)$$

where

V_0 = source voltage and

$I^*(0)$ = complex conjugate of current at antenna terminals.

For a lossless antenna the radiated power is equal to the input power and the efficiency is 100%. The average gain will depend upon K (i.e. the ground conditions). The lossless HFDF SSL antenna elements were first considered in free space where the expected value of the average power gain is 1. For operation over ground, average power gain should be 2. The NEC model was also tested over the two types of lossy ground

specified previously, good ground, $\epsilon=30$ and $\sigma=0.01$, and poor ground, $\epsilon=5$ and $\sigma=0.001$.

The average gains for the NEC models of the crossed loop and monopole antennas with these ground conditions are shown in Figures 18 and 19.

The average gains for the NEC models are well within $\pm 10\%$ of theoretical values for the lossless cases, providing additional confidence of numerical model validity.

D. RADIATION PATTERNS

Radiation patterns were calculated for both antennas to provide a final certification of model validity. Elevation patterns of the crossed loop were obtained for 2, 5 and 10 MHz, under the four ground conditions, free space, perfect ground, good ground, and poor ground. A horizontal radiation pattern for 5 MHz and perfect ground conditions verified the omnidirectionality of the total gain in this plane. The patterns are shown in Appendix C.

Radiation patterns of the vertical monopole with wire mesh counterpoise were produced for 10, 15, and 20 MHz, under the same four ground conditions. The elevation patterns are shown in Appendix D and include the vertical, horizontal, and total power gain curves. An azimuth pattern at 15 MHz and perfect ground verified the omnidirectionality of the total gain of the monopole. This pattern is also shown in Appendix D.

From the preceding, the conclusions are that since long-range HF propagation generally occurs at higher frequencies and lower angles, the choice of using vertical

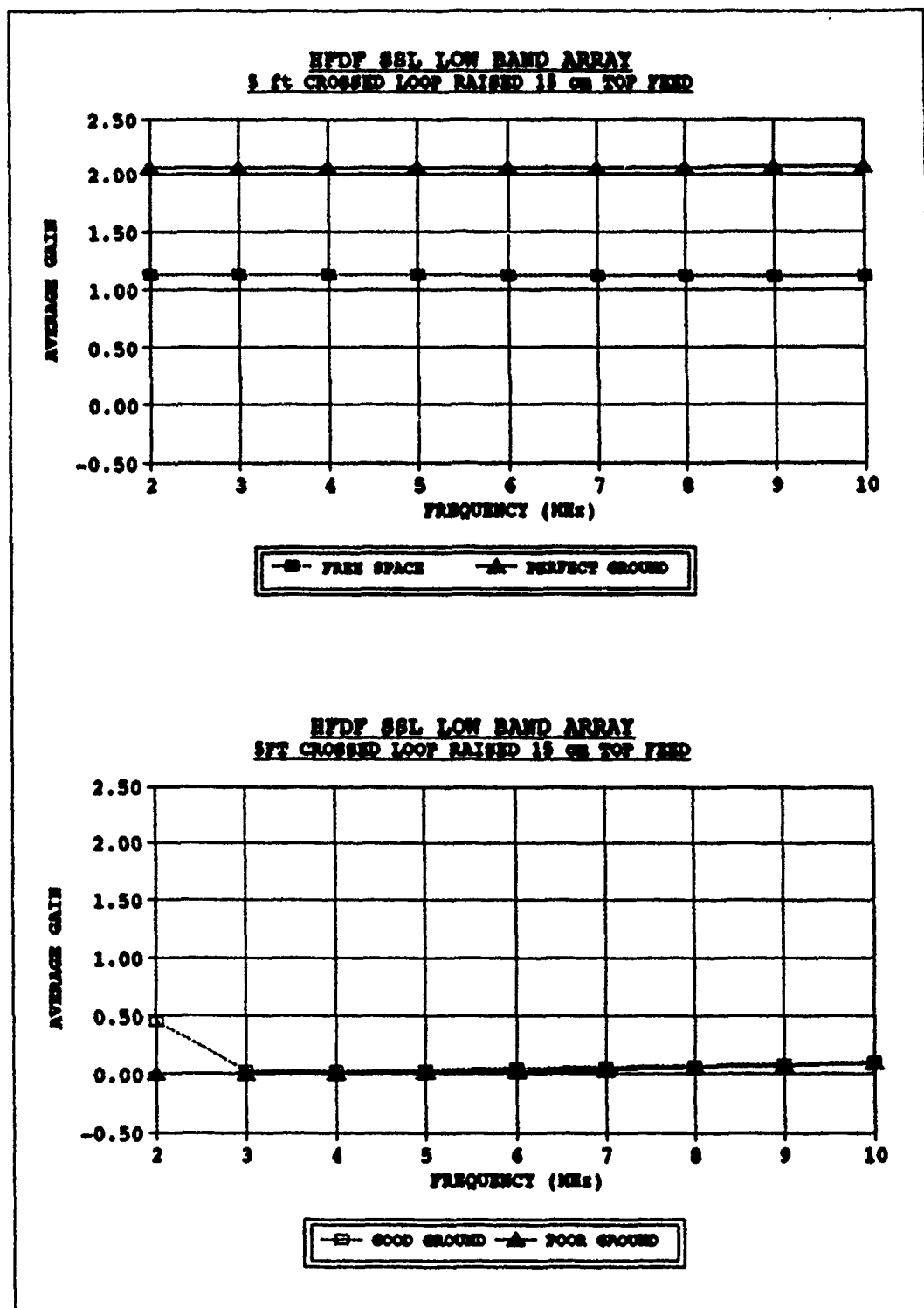


Fig. 18.- Low Band Array Average Gain Versus Frequency.

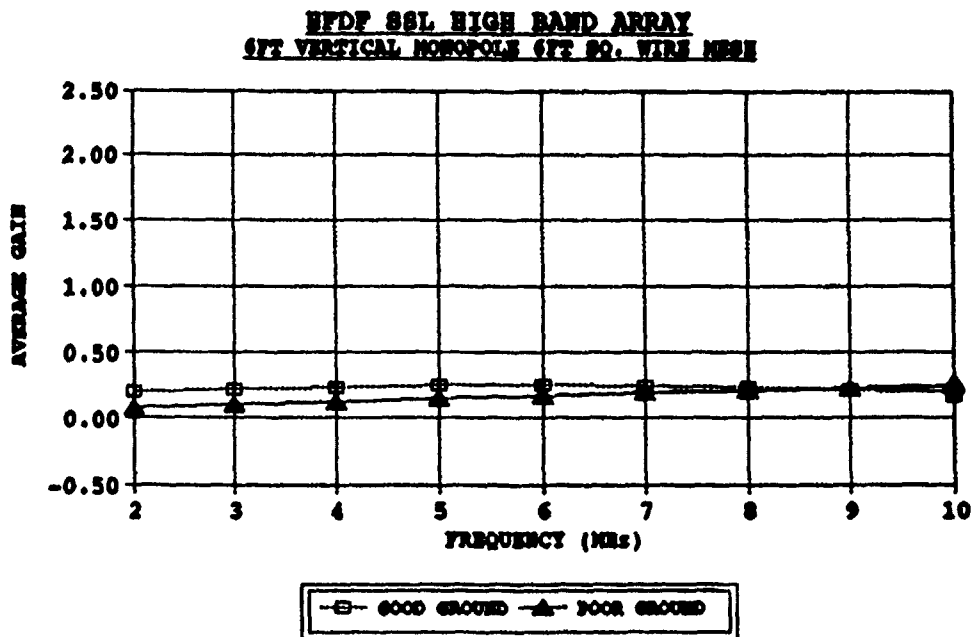
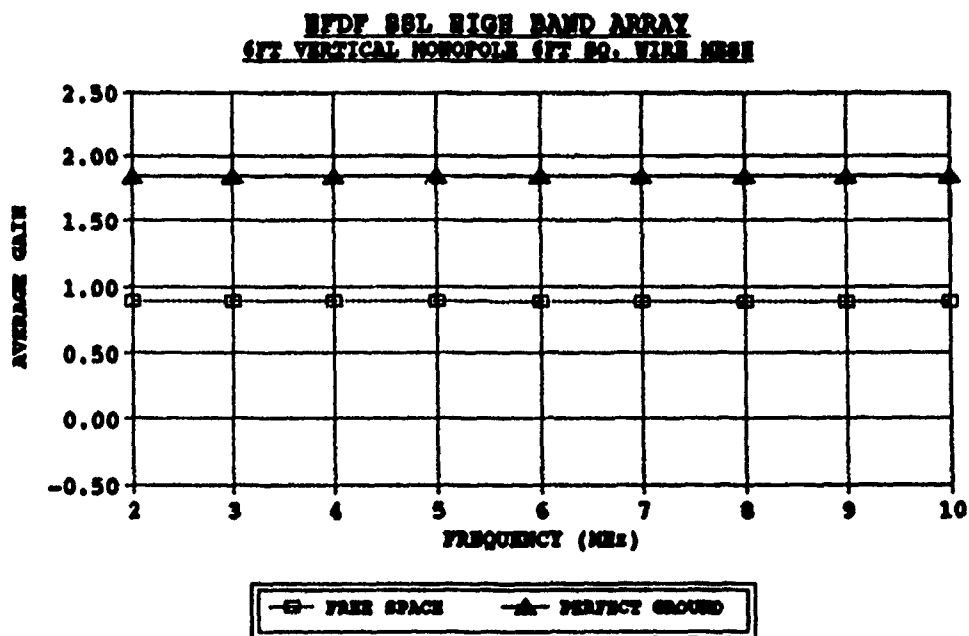


Fig. 19.- High Band Array Average Gain Versus Frequency.

monopoles for the high band array is good. Similarly, the use of the vertical crossed loops is a good choice for the low band array, since shorter range HF propagation uses lower frequencies and high elevation angles.

V. HFDF SSL ERROR ANALYSIS

A. DF MATHEMATICAL MODEL

If the actual location of the antennas in the "L" shaped arrays is included in the equations for angles of arrival from Chapter II, the expressions can be further simplified.

Recognizing that all antennas of the array are located at the same height above the ground and placing the reference antenna which is located at the vertex of the array at the origin of the coordinate system, z_i , b_1 , b_2 and a_2 become zero and can be eliminated from equation 33, reducing the expression for elevation angle of arrival to

$$\psi = \sin^{-1} \left(\frac{\sqrt{c^2 - a_1^2 - a_2^2}}{c} \right) \quad (51)$$

and the azimuth angle to

$$\phi = \tan^{-1} \left(\frac{a_1}{-a_2} \right) . \quad (52)$$

These expressions can be further simplified by aligning the first arm of the interferometer with the y-axis and the second arm with the x-axis.

The antenna coordinates x_1 and y_2 become equal to zero, which when applied to variables defined previously result in

$$a_1 = \left(\frac{\Phi_1}{\beta} \right) x_2, \quad a_2 = - \left(\frac{\Phi_2}{\beta} \right) y_1 \quad \text{and} \quad c = x_2 y_1.$$

The elevation angle of arrival of the wave can thus be expressed as

$$\psi = \sin^{-1} \left[\frac{\sqrt{(x_2 y_1)^2 - \left(\frac{\Phi_1}{\beta} \right)^2 x_2^2 - \left(\frac{-\Phi_2}{\beta} \right)^2 y_1^2}}{x_2 y_1} \right] \quad (53)$$

and the azimuth angle by

$$\phi = \tan^{-1} \left[\frac{\Phi_1 (x_2)}{\Phi_2 (y_1)} \right]. \quad (54)$$

Since the interferometer compares the phase measured at the antennas two at a time, one on each arm of the interferometer array, the antennas on each arm are selected to be equidistant from the reference antenna. Incorporating these facts into the analysis and using the specific geometry of the two antenna arrays, the x-coordinate of the antenna on the first arm of the interferometer is equal to the y-coordinate of the corresponding antenna on the second arm, so $x_2 = y_1$.

Replacing these values in equations 53 and 54 and simplifying, the elevation angle of arrival becomes

$$\psi = \sin^{-1} \left[\frac{\sqrt{(x_2)^2 - \left(\frac{\Phi_1}{\beta}\right)^2 - \left(\frac{-\Phi_2}{\beta}\right)^2}}{x_2} \right] \quad (55)$$

or

$$\psi = \cos^{-1} \left[\frac{1}{\beta x_2} \sqrt{\Phi_1^2 + \Phi_2^2} \right] \quad (56)$$

and the azimuth angle,

$$\phi = \tan^{-1} \left(\frac{\Phi_1}{\Phi_2} \right) . \quad (57)$$

B. BEARING AMBIGUITY RESOLUTION

In both of the antenna arrays the distance between the reference antenna and the first antenna of each arm is less than one-half wavelength at the lowest frequency (longest wavelength), so the phase difference between these antennas will be less than 180° . As explained in Chapter II, the phase difference is measured as modulo 180° , therefore no ambiguity in the measurement will occur. A different situation occurs with the rest of the antenna pairs of the array where the phase difference between each element and the

reference antenna can be more than 180° and ambiguity in the measurement of the angle of arrival occurs. A means of determining the number of 180° differences is needed for finding the exact baseline phase.

Each arm of the interferometer has three baselines formed by the reference antenna and each of the antennas of the arm. The "short-baseline" is formed by the first antenna of the arm; the "intermediate-baseline" is formed by the second antenna; and the third antenna forms the "long-baseline". To find the exact phase difference of the intermediate baseline, the short-baseline phase must be measured first. The number of 180° phase rotations are computed using the formula

$$N = \left[\alpha_s \left(\frac{d_i}{d_s} \right) - \alpha_i \right], \quad (58)$$

where

α_s = short-baseline phase,

α_i = intermediate-baseline phase (unresolved),

d_s = short-baseline length,

d_i = intermediate-baseline length, and

$[]$ = nearest integer function.

The resolved intermediate-baseline phase can then be calculated by

$$\Phi_i = N (180^\circ) + \alpha_i . \quad (59)$$

Using the same procedure the resolved long-baseline phase can be calculated by replacing intermediate-baseline values with the corresponding long-baseline values.

Considering the validity of the phase measurements completes the mathematical model. When the received signal is not a single plane wave, phase measurements may correspond to phases of different components of the incoming wave (different propagation modes) or to the vector sum of several components arriving at the antenna. If the resulting phase measurements differ greatly from one another, as when two different propagation modes are being received, they do not provide required information to unambiguously define the angle of arrival.

To solve this ambiguity, the system uses a Quasi-Single Phase Wave (QSPW) test to categorize measured phases into "phase-linear" and "non-phase-linear" values. The QSPW test interpolates the resolved long-baseline phase to the intermediate-baseline phase and checks for agreement within an acceptable phase window. This acceptable window is usually set to 30° . The computation performed on each arm of the interferometer can be expressed as

$$\left| \Phi_i - \Phi_L \left(\frac{d_i}{d_L} \right) \right| \leq \alpha_w, \quad (60)$$

where

Φ_i = resolved Intermediate Phase,

Φ_L = resolved long phase,

d_i = intermediate baseline length,

d_L = long baseline length, and

α_w = acceptable phase window.

If this condition is satisfied on both legs of the array simultaneously, the azimuth and elevation calculated with these values is said to be a "phase linear frame". The wave can then be considered a Quasi-Single plane wave, which is a good approximation of a plane wave.

C. SELECTION OF ANGLES OF ARRIVAL FOR MODEL COMPARISON

A set of angles of arrival of incoming waves must be defined to effectively test both antenna arrays. For the azimuth plane, a set of angles that exploits the 180° symmetry of both arrays is selected. The resultant set of angles is shown in Fig. 20.

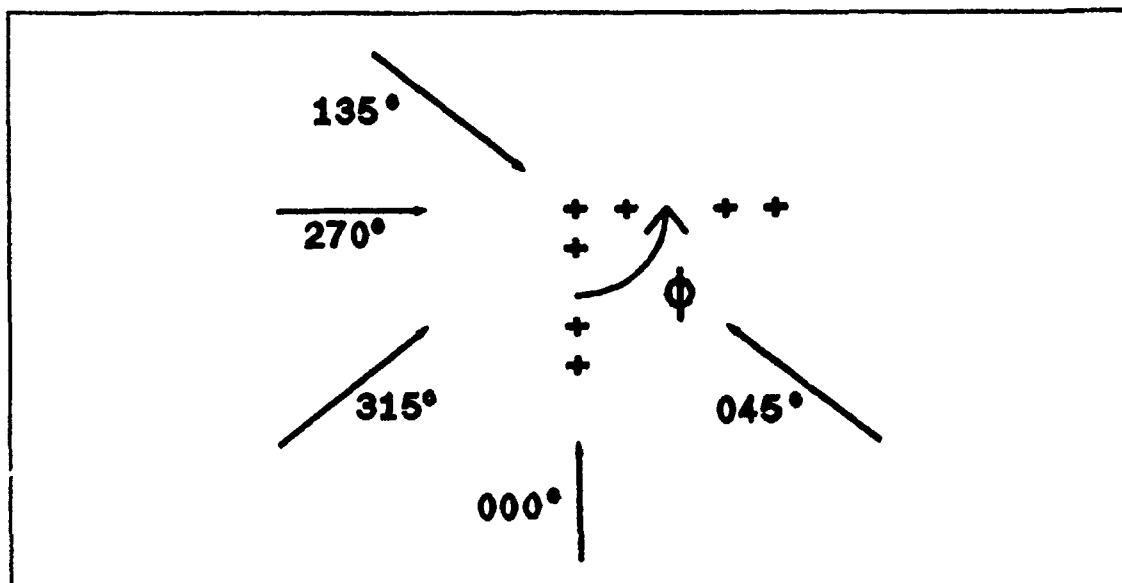


Fig. 20.- Test Azimuth Angles.

Next, the elevation plane which corresponds to $\theta = 90^\circ$ in spherical coordinates is considered. Elevation angles of arrival for testing the arrays are suggested by the tactical scenario described in Chapter I and the typical HFDF SSL paths outlined in Chapter II. From these conditions a set of angles is chosen which thoroughly tests the array in the elevation plane, as is shown in Fig. 21.

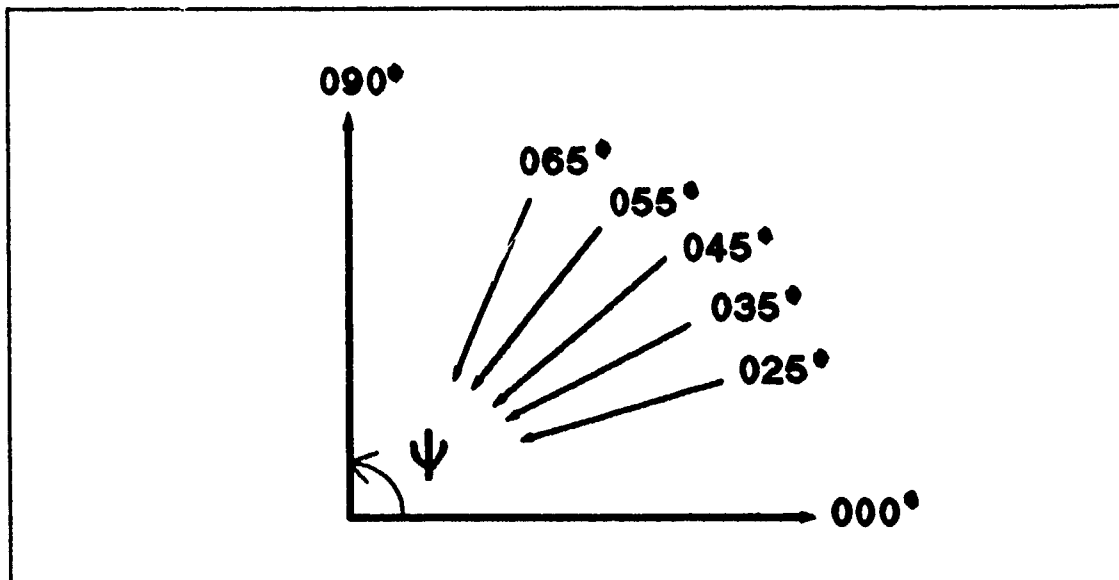


Fig. 21.- Test Elevation Angles

D. SSL ARRAY PHASE ERROR ANALYSIS

To find the amount of error induced by the pairs of antennas in the arrays in the phase measurements, the selected azimuth and elevation angles were combined to define directions of arrival of plane waves. These "test" waves are "incident waves" for NEC calculations.

The phase of currents induced in the different antennas of the arrays, when excited by each of the incident waves, were calculated via NEC and compared with phase values from the mathematical model. The mathematical model does not include the effects of

antenna coupling, wave scattering, or ground conditions, while NEC does include them. The difference between the phases produced by the two models is referred to as the "phase error".

To select a reasonable number of multiple combinations of azimuth, elevation, frequency, antenna pair, and ground conditions, the following cases were selected:

LOW BAND ARRAY

- Frequency: 5 MHz
- Ground condition: Good ground and poor ground
- Antenna pair: Longest baseline
- Azimuth: -135°, -090°, -045°, 000° and 045°
- Elevation (90- θ): 025°, 035°, 045°, 055°, and 065°

HIGH BAND ARRAY

- Frequency: 15 MHz
- Ground condition: Perfect ground
- Antenna pair: Longest baseline
- Azimuth: -135°, -090°, -045°, 000° and 045°
- Elevation (90- θ): 025°, 035°, 045°, 055°, and 065°

The different runs are summarized in the following subsections. Figures showing results of phase error calculations are contained in Appendix E.

1. Low Band Array Phase Errors

Fig. E-1 presents phase errors induced by the longest baselines of arm-1 (y axis), and arm-2 (x axis), of the low band array, at 5 MHz over good ground, for an azimuth 000° and varying elevation from 025° to 065° .

The elevation angle of the incident wave was set to 045° and the azimuth angle varied between -135° and 045° . Fig. E-2 shows the phase errors induced by the longest baselines of both arms of the low band array.

Ground conditions for the above cases were changed to poor ground and the analysis repeated. Fig. E-3 and Fig. E-4 show the resultant phase errors for the same array.

From these figures, it is seen that for the low band array phase errors calculated for arm-1 and for arm-2 of the interferometer with good ground conditions were comparable with poor ground conditions. This indicates that phase errors induced by the low band antenna array did not change significantly with ground conditions.

There is a similar phase error in both arms of the interferometer for an incident wave as an azimuth angle of 045° as well as from -135° . The symmetry of the incident wave, with respect to both arms of the interferometer, is maintained for the low band elements the same as it is for high band at these azimuth angles.

The smallest phase errors occur at the highest incident wave elevation angles. This conforms to the electromagnetic properties of the crossed loop antennas which have good gain at high elevation angles, and poor gain at lower angles.

2. High Band Array Phase Errors

Fig. E-5 shows phase errors produced by the longest baselines of arm-1 (y-axis), and arm-2 (x-axis) of the high band antenna at 15 MHz over good ground and for an incident wave azimuth of 000° , and elevation angle varying between 025° and 065° . Fig. E-6 shows phase errors from the same baselines of the high band array for identical ground and frequency conditions, an elevation angle of 045° and azimuth angles from -135° to 045° . The effects of changing the ground conditions to poor ground are shown in Fig. E-7 and Fig. E-8. These values for arm-1 varied significantly from those calculated for poor ground case. A similar effect is observed for arm-2. Ground conditions do have a significant effect on phase errors for the high band antenna array.

When the incident wave arrives from an azimuth of 045° and -135° a similar value of phase error occurs in both arms of the high band interferometer. This confirms symmetry of the incident wave with respect to arms of the interferometer.

For good ground conditions the phase errors of both high band array arms are larger at high incident wave elevation angles. For poor ground conditions the largest phase errors were at lower incident wave elevation angles. These results suggest that stronger antenna element coupling and inter-element scattering occurs for good ground than for poor ground.

E. EFFECT OF SSL PHASE ERROR IN AOA MEASUREMENT

The preceding antenna phase errors do not directly represent the final angle of arrival (AOA) errors. The actual azimuth and elevation errors also depend on specific

algorithm sensitivity to these phase errors. As explained in Chapter II, a longer baseline decreases the effects of phase measurement errors in determining the angle-of-arrival (AOA) For this reason only the longest baselines were used to determine the AOA measurements, with the shorter baselines used to eliminate ambiguities. Thus, the system implements a wide aperture array while maintaining required ambiguity resolution capabilities.

The magnitude of the AOA errors were determined by comparing NEC phase values with those of the math model. The figures showing the results of the AOA error calculations, for both the low band and high band interferometer array, are contained in Appendix F.

Fig. F-1 shows the azimuth and elevation error induced in the HFDF SSL system by the low band antenna array. These errors were calculated for a frequency of 5 MHz, good ground 045° azimuth incidence varying elevation angles between 025° and 065°. Fig. F-2 shows the HFDF SSL error in azimuth and elevation for the same conditions but fixing the incident elevation angle at 045° and varying azimuth between -135° and 045°. Similarly, Fig. F-3 and Fig. F-4 show the corresponding azimuth and elevation error for the low band array over poor ground and the same conditions of incident waves for the previous two cases.

From an analysis of these figures it is observed that the HFDF SSL azimuth and elevation errors induced by the low band antenna array are approximately one order of magnitude less than the individual phase errors from which they are calculated. The

largest azimuth and elevation error of the low band array was less than 0.2° for all cases analyzed.

Fig. F-5 summarizes errors for the high band antenna array at 15 MHz, good ground, and an azimuth incidence angle of 045° and elevation angles between 025° and 065° . Corresponding azimuth and elevation errors for a fixed elevation of angle of the of 045° and varying azimuth angles from -135° to 045° are shown in Fig. F-6. Equivalent error calculations were made for the high band array, for poor ground conditions and appear in Fig. F-7 and Fig. F-8.

There is a tendency of the system to produce larger azimuth errors at high elevation angles of arrival of the incident wave for the high band antenna array, under good and poor ground conditions. Azimuth errors of the high band array were approximately one order of magnitude less than phase errors for all ground conditions and angles of arrival of the incident wave. The largest azimuth and elevation error induced by the high band array was found to be less than 0.5° for all cases analyzed.

The lowest phase errors occur when the incident wave arrives at 045° or at -135° for both the low and high band arrays. This result shows that the "L" shape geometry of the antenna arrays has two preferred angles of arrival at 045° and -135° for the specific orientation of the antenna array shown in Fig. 1.

In general, azimuth and elevation errors were slightly smaller for the low band antenna than for the high band.

F. HFDF SSL ERROR AND SSL FOOTPRINT

The accuracy of an HFDF SSL system is measured by comparing the predicted transmitter location to the actual position. Emitter position errors can be observed after the application of the vertical triangulation technique to the angle of arrival of the incoming wave.

Many factors can generate errors in HFDF SSL systems. This study was concerned only with errors introduced by the antenna array; therefore, the lateral and range errors introduced in the position of the emitter by bearing errors found in the previous sections are considered.

When the virtual height of the ionosphere is assumed to be known and in addition, a no-tilt case is assumed, the lateral error is only a function of the azimuth error introduced in the HFDF SSL by the antenna array. Likewise, range error is dependent upon the elevation angle error. Furthermore, the lateral and range errors form what is called the HFDF SSL "footprint".

This footprint is usually elliptical in shape with the size of its major axis determined by range error, while the minor axis is proportional to the lateral error.

The HFDF SSL errors for the system under consideration can then be estimated by applying the flat-earth flat-ionosphere model described in Chapter II, to the maximum azimuth and elevation errors calculated in the previous section for each antenna array.

A value of 0.2° was used for the low band array, and 0.5° for the high band array. Lateral and range errors of the HFDF SSL system were calculated for the largest and

smallest emitter distances of the tactical scenario and the maximum dimensions of the minor and major axes of the HFDF SSL footprint were then determined.

For the low band array the maximum dimensions of the major (range error) and minor (lateral error) axes of the HFDF SSL footprint are:

<u>EMITTER-SSL DISTANCE</u>	<u>PROPAGATION MODE</u>	<u>MAJOR AXIS (RANGE ERROR)</u>	<u>MINOR AXIS (LATERAL ERROR)</u>
300 km	E	4.3 km	2.1 km
300 km	F ₂	5.3 km	2.1 km
500 km	E	8.9 km	3.5 km
500 km	F ₂	7.1 km	3.5 km .

For the high band array the maximum dimensions of the major (range error) and minor (lateral error) axes of the footprint are:

<u>EMITTER-SSL DISTANCE</u>	<u>PROPAGATION MODE</u>	<u>MAJOR AXIS (RANGE ERROR)</u>	<u>MINOR AXIS (LATERAL ERROR)</u>
300 km	E	10.7 km	5.2 km
300 km	F ₂	13.1 km	5.2 km
500 km	E	22.4 km	8.7 km
500 km	F ₂	17.7 km	8.7 km .

The maximum HFDF SSL lateral and range errors occur for the high band array where the targeted emitter is located at the larger distance specified by the tactical scenario, and the incoming wave has an E-propagation mode. The smallest lateral and range errors occur when the system uses the low band array, the targeted emitter is

located at the shortest distance specified by the tactical scenario and the incoming wave has an E-propagation mode.

VI. CONCLUSIONS AND RECOMMENDATIONS

A. CONCLUSIONS

The characteristics of two HF antenna arrays which are part of a phase-interferometer HFDF SSL system that operates in the 2 to 30 MHz band were analyzed using the Numerical Electromagnetics Code (NEC) and comparing the results with the ideal case.

The larger the aperture of the antenna array compared with the wavelength of the incoming signal, the better its resolution when determining the angle of arrival of an elevated, incoming wave. Therefore, in the HFDF SSL system of this study, the longest baselines of the phase-interferometer were selected to determine AOA while the shorter baselines were used to eliminate ambiguities.

The analysis included a comparison between the effects of the different ground conditions. Special consideration was given to good ground ($\epsilon_r = 30$ and $\sigma = 0.01$) and poor ground ($\epsilon_r = 5$ and $\sigma = 0.001$) cases. The high band antenna array (10 to 20 MHz), suffered the maximum coupling and strongest inter-element scattering for good ground, where it produced the largest phase errors. For the low band antenna array (2 to 10 MHz), changing ground conditions do not affect the phase errors substantially.

There is a consistently lower phase error induced by the low band array for 2 to 10 MHz than for the high band array using vertical monopoles with a wire grid mesh counterpoise for the 10 to 20 MHz band.

The "L" shape of the geometry of the two antenna arrays had two preferred azimuth angles of arrival for incoming waves. These azimuth angles were 045° and -135° , respectively (see Fig. 1). Waves arriving from these angles induced an almost negligible azimuth error in the DF system.

Angle of arrival errors for the high band array were less than 0.5° and were under 0.2° for the low band antenna system.

The dimensions of the minor and major axes of the HFDF SSL footprint were calculated for the minimum and maximum emitter distances considered in the tactical scenario. The major axis was called range error and the minor axis was called lateral error. The maximum HFDF SSL lateral and range error of this system are 8.7 km and 22.4 km respectively. These error values occur when the system uses the high band array, the targeted emitter is located at the largest distance specified by the tactical scenario (500 km), and the incoming wave has an E-propagation mode.

The smallest lateral and range error were found to be 2.1 km and 4.3 km respectively. They arise when the system uses the low band array, the targeted emitter is located at the shortest distance specified by the tactical scenario (300 km), and the incoming wave has an E-propagation mode.

The Numerical Electromagnetics Code (NEC) proved to be an excellent tool for the analysis of this electromagnetic problem. It was particularly useful because of its ability to simulate the antenna structures, the environment where they are located, and the incoming plane waves used to test the HFDF SSL system.

B. RECOMMENDATIONS

Future analysis of the effects of the HFDF SSL azimuth and elevation errors found in this study, when using actual ionospheric characteristics of the near-equatorial region, is needed.

Comparison between theoretical calculations performed in this study and measurements of the actual system can provide information for assessing the errors induced by other components of the system and better insight into capabilities and limitations.

APPENDIX A

NEC DATASETS

1) HIGH BAND ANTENNA ARRAY

CM	HIGH BAND 7 VERTICAL MONOPOLES ARRAY	
CM		
CM	6-FOOT VERTICAL MONOPOLES	
CM		
CM	0.5 FEET ABOVE THE GROUND	
CM		
CM	FEED POINT AT BOTTOM OF EACH MONOPOLE	
CM		
CM	GROUND SCREEN 6 FEET X 6 FEET WITH 6 INCH SPACING	
CM		
CM	ADDITIONAL 6 FEET RADIALS EVERY 45 DEGREES	
CM		
CM	SCREEN UP 0.001 METERS FROM GROUND	
CM		
CM	OVER GOOD GROUND	
CE		
GW111,1,	.1524,0.,0.,.1524,.9144,0.,0.01,	BUILD ONE SECTOR
GW111,1,	.3048,0.,0.,.3048,.9144,0.,0.01,	OF THE 6 FOOT
GW111,1,	.4572,0.,0.,.4572,.9144,0.,0.01,	SQUARE WIRE MESH,
GW111,1,	.6096,0.,0.,.6096,.9144,0.,0.01,	0.5 FEET BETWEEN
GW111,1,	.7620,0.,0.,.7620,.9144,0.,0.01,	WIRES.
GW111,1,	.9144,0.,0.,.9144,.9144,0.,0.01,	
GW111,1,0,	.1524,0.,.9144,.1524,0.,0.01,	
GW111,1,0,	.3048,0.,.9144,.3048,0.,0.01,	
GW111,1,0,	.4572,0.,.9144,.4572,0.,0.01,	
GW111,1,0,	.6096,0.,.9144,.6096,0.,0.01,	
GW111,1,0,	.7620,0.,.9144,.7620,0.,0.01,	
GW111,1,0,	.9144,0.,.9144,.9144,0.,0.01,	
GW111,1,	.9144,.9144,0.,1.293,1.293,0.,0.01,	CREATE CORNER RADIAL
GM0,3,0,	.0.,.90,0.,0.,0.,111.111,	GENERATE THE OTHER 3 SECTORS
GW111,4,0,	,-1.8288,0.,0.,1.8288,0.,0.01,	ADD Y AXIS ADDITIONAL RADIALS
GW111,4,	-1.8288,0.,0.,1.8288,0.,0.,0.01,	ADD X AXIS ADDITIONAL RADIALS
GM0,0,0,	.0.,0.,0.,0.,0.001,111.111,	MOVE WIRE MESH UP .001 METERS
GW111,3,0,	.0.,0.,0.15,0.,0.,1.9788,.05,	CREATE 6 FOOT MONOPOLE
GW111,1,0,	.0.,0.,0.001,0.,0.,0.15,0.05,	CONNECT MONOPOLE TO WIRE MESH
GM0,0,0,	.0.,0.,0.,4.33,0.,111.111,	MOVE STRUCTURE TO Y=4.33 M
GM1,1,0,	.0.,0.,0.,29.0,0.,111.111,	CREATE ANTENNA 2 AT Y=33.33 M
GM1,1,0,	.0.,0.,0.,16.67,0.,112.112,	CREATE ANTENNA 3 AT Y=50 M
GM0,0,0,	.0.,45,0.,0.,0.,111.113,	ROTATE STRUCTURE 45 DEG UP
GX3,100,		REFLECT STRUCTURE OVER Y AXIS
GM0,0,0,	.0.,-45,0.,0.,0.,111.116,	ROTATE STRUCTURE 45 DEG DOWN
GP		SUPPRESS GEOMETRY PRINTING
GE1		END GEOMETRY DEFINITION
GN2,0,0,0,	30.,0.01	GOOD GROUND CONDITIONS
FR0,1,0,0,	15.,	FREQUENCY 15 MHZ
WG,		CALCULATE GREEN'S FUNCTION
NX,		START NEXT STRUCTURE
CM	START NEXT STRUCTURE	COMMENTS
CM		
CM	ADD ANTENNA ZERO	
CE		
GF,		

GW120,1,.1524,0.,0.,.1524,.9144,0.,0.01,	BUILD ONE SECTOR
GW120,1,.3048,0.,0.,.3048,.9144,0.,0.01,	OF THE 6 FOOT
GW120,1,.4572,0.,0.,.4572,.9144,0.,0.01,	SQUARE WIRE MESH,
GW120,1,.6096,0.,0.,.6096,.9144,0.,0.01,	0.5 FEET BETWEEN
GW120,1,.7620,0.,0.,.7620,.9144,0.,0.01,	WIRES.
GW120,1,.9144,0.,0.,.9144,.9144,0.,0.01,	
GW120,1,0.,.1524,0.,.9144,.1524,0.,0.01,	
GW120,1,0.,.3048,0.,.9144,.3048,0.,0.01,	
GW120,1,0.,.4572,0.,.9144,.4572,0.,0.01,	
GW120,1,0.,.6096,0.,.9144,.6096,0.,0.01,	
GW120,1,0.,.7620,0.,.9144,.7620,0.,0.01,	
GW120,1,0.,.9144,0.,.9144,.9144,0.,0.01,	
GW120,1,.9144,.9144,0.,1.293,1.293,0.,0.01,	CREATE CORNER RADIAL
GM0,3,0.,0.,90.,0.,0.,0.,120.120,	GENERATE THE OTHER 3 SECTORS
GW120,4,0.,-1.8288,0.,0.,1.8288,0.,0.01,	ADD Y AXIS ADDITIONAL RADIALS
GW120,4,-1.8288,0.,0.,1.8288,0.,0.01,	ADD X AXIS ADDITIONAL RADIALS
GM0,0,0.,0.,0.,0.,0.,0.,120.120,	MOVE WIRE MESH UP .001 METERS
GW120,3,0.,0.,0.15,0.,0.,1.9788,.05,	CREATE 6 FOOT MONOPOLE
GW120,1,0.,0.,0.001,0.,0.,0.15,0.05,	CONNECT MONOPOLE TO WIRE MESH
GP	SUPPRESS GEOMETRY PRINTING
GE1	END GEOMETRY DEFINITION
PT1,111,61,0	ANTENNA 1
EX1,5,5,0,25,-135,0,10,45	
XQ,	
PT1,112,61,0	ANTENNA 2
EX1,5,5,0,25,-135,0,10,45	
XQ,	
PT1,113,61,0	ANTENNA 3
EX1,5,5,0,25,-135,0,10,45	
XQ,	
PT1,114,61,0	ANTENNA 4
EX1,5,5,0,25,-135,0,10,45	
XQ,	
PT1,115,61,0	ANTENNA 5
EX1,5,5,0,25,-135,0,10,45	
XQ,	
PT1,116,61,0	ANTENNA 6
EX1,5,5,0,25,-135,0,10,45	
XQ,	
PT1,120,61,0	ANTENNA 0
EX1,5,5,0,25,-135,0,10,45	
XQ,	
EN	END DATASET

2) LOW BAND ANTENNA ARRAY

CM LOW BAND 7 CROSSED SQUARE LOOP ARRAY
 CM
 CM 5-FOOT SQUARE LOOPS
 CM
 CM 0.5 FEET ABOVE THE GROUND
 CM
 CM ORTHOGONAL LOOP 2 INCHES ABOVE AXIAL LOOP
 CM
 CM FEED POINT AT TOP OF EACH LOOP
 CM
 CM OVER GOOD GROUND
 CE
 GW11,3,0.,-.762,1.524,0.,.762,1.524,.05, CREATE Y AXIS LOOP TOP

GW11,1,0.,.762,1.524,0.,.762,0.,.05,
 GW11,1,0.,.762,0.,0.,-.762,0.,.05,
 GW11,1,0.,-.762,0.,0.,-.762,1.524,.05,
 GW11,3,-.762,0.,1.574,.762,0.,1.574,.05,
 GW11,1,.762,0.,1.574,.762,0.,0.05,.05,
 GW11,1,.762,0.,0.05,-.762,0.,0.05,.05,
 GW11,1,-.762,0.,0.05,-.762,0.,1.574,.05,
 GM0,0,0.,0.,0.,0.,.15,11.11,
 GM0,0,0.,0.,0.,0.,.13,0.,11.11,
 GM1,1,0.,0.,0.,0.,.87,0.,11.11,
 GM1,1,0.,0.,0.,0.,.50,0.,12.12,
 GM1,1,0.,0.,0.,.13,-.150,0.,13.13,
 GM1,1,0.,0.,0.,.87,0.,0.,14.14,
 GM1,1,0.,0.,0.,.50,0.,0.,15.15,
 GM4,1,0.,0.,0.,-.150,0.,0.,16.16,
 GE1
 GN2,0,0,0,30,0.01
 FR0,1,0,0,5.,
 PT1,11,2,0
 EX1,5,5,0,25,-135,0,10,45
 XQ,
 PT1,11,8,0
 EX1,5,5,0,25,-135,0,10,45
 XQ,
 PT1,12,2,0
 EX1,5,5,0,25,-135,0,10,45
 XQ,
 PT1,12,8,0
 EX1,5,5,0,25,-135,0,10,45
 XQ,
 PT1,13,2,0
 EX1,5,5,0,25,-135,0,10,45
 XQ,
 PT1,13,8,0
 EX1,5,5,0,25,-135,0,10,45
 XQ,
 PT1,14,2,0
 EX1,5,5,0,25,-135,0,10,45
 XQ,
 PT1,14,8,0
 EX1,5,5,0,25,-135,0,10,45
 XQ,
 PT1,15,2,0
 EX1,5,5,0,25,-135,0,10,45
 XQ,
 PT1,15,8,0
 EX1,5,5,0,25,-135,0,10,45
 XQ,
 PT1,16,2,0
 EX1,5,5,0,25,-135,0,10,45
 XQ,
 PT1,16,8,0
 EX1,5,5,0,25,-135,0,10,45
 XQ,
 PT1,20,2,0
 EX1,5,5,0,25,-135,0,10,45
 XQ,
 PT1,20,8,0
 EX1,5,5,0,25,-135,0,10,45
 XQ,
 EN

CREATE Y LOOP SIDE
 CREATE Y LOOP BOTTOM
 CREATE Y LOOP SIDE
 CREATE X LOOP TOP
 CREATE X LOOP SIDE
 CREATE X LOOP BOTTOM
 CREATE X LOOP SIDE
 MOVE STRUCTURE UP .15 METERS
 MOVE STRUCTURE TO Y=13 M
 CREATE ANTENNA 2 AT Y=100 M
 CREATE ANTENNA 3 AT Y=150 M
 CREATE ANTENNA 4 AT X=13 M
 CREATE ANTENNA 5 AT X=100 M
 CREATE ANTENNA 6 AT X=150 M
 CREATE ANTENNA ZERO
 END GEOMETRY DEFINITION
 GOOD GROUND CONDITIONS
 FREQUENCY 5 MHZ
 ANTENNA 1 (X AXIS ELEMENT)

 ANTENNA 1 (Y AXIS ELEMENT)

 ANTENNA 2 (X AXIS ELEMENT)

 ANTENNA 2 (Y AXIS ELEMENT)

 ANTENNA 3 (X AXIS ELEMENT)

 ANTENNA 3 (Y AXIS ELEMENT)

 ANTENNA 4 (X AXIS ELEMENT)

 ANTENNA 4 (Y AXIS ELEMENT)

 ANTENNA 5 (X AXIS ELEMENT)

 ANTENNA 5 (Y AXIS ELEMENT)

 ANTENNA 6 (X AXIS ELEMENT)

 ANTENNA 6 (Y AXIS ELEMENT)

 ANTENNA 0 (X AXIS ELEMENT)

 ANTENNA 0 (Y AXIS ELEMENT)

 END NEC DATASET

APPENDIX B

ANTENNA INPUT IMPEDANCE

TABLE B-1

5FT SQ CROSSED LOOP TOP FEED

FREQ. MHZ	IMPEDANCE LOOP-1 (Y AXIS)		IMPEDANCE LOOP-2 (X AXIS)	
	<u>REAL</u>	<u>IMAGINARY</u>	<u>REAL</u>	<u>IMAGINARY</u>
GOOD GROUND (EPS=30, SIG=0.01)				
2	0.026	46	0.02	45
3	0.20	70	0.11	67
4	0.55	93	0.35	91
5	0.97	118	0.66	115
6	1.6	144	1.08	141
7	2.2	171	1.59	167
8	3.1	201	2.27	195
9	4.4	232	3.20	226
10	6.0	266	4.44	258
POOR GROUND (EPS=5, SIG=0.001)				
2	0.59	46	0.30	45
3	0.93	69	0.51	67
4	1.22	92	0.70	90
5	1.51	116	0.90	114
6	1.82	141	1.12	139
7	2.14	168	1.37	165
8	2.49	195	1.73	193
9	3.22	226	2.16	222
10	3.94	259	2.71	255
PERFECT GROUND				
2	0.001	43	0.001	42
3	0.003	64	0.003	64
4	0.011	86	0.011	86
5	0.026	109	0.026	109
6	0.055	133	0.055	133
7	0.10	158	0.10	158
8	0.18	184	0.18	184
9	0.30	212	0.30	212
10	0.47	242	0.47	242
FREE SPACE				
2	0.000	43	0.000	43
3	0.002	65	0.002	65
4	0.005	87	0.005	87
5	0.013	110	0.013	110
6	0.028	135	0.028	135
7	0.055	160	0.055	159
8	0.10	186	0.10	186
9	0.17	215	0.17	215
10	0.29	246	0.29	246

TABLE B-2

6 FT VERTICAL MONOPOLE, 6FT SQ WIRE MESH

<u>FREQ.</u> <u>MHZ</u>	<u>IMPEDANCE</u>	
	<u>REAL</u>	<u>IMAGINARY</u>
GOOD GROUND (EPS=30, SIG=0.01)		
10	12	-541
11	13	-479
12	14	-426
13	16	-380
14	19	-339
15	22	-302
16	26	-268
17	32	-237
18	40	-209
19	49	-184
20	59	-163
POOR GROUND (EPS=5, SIG=0.001)		
10	15	-574
11	14	-511
12	14	-458
13	14	-412
14	14	-371
15	15	-335
16	15	-303
17	16	-274
18	17	-247
19	18	-222
20	18	-199
PERFECT GROUND		
10	3.2	-553
11	3.2	-493
12	4.6	-443
13	5.4	-399
14	6.3	-361
15	7.2	-327
16	8.3	-297
17	9.4	-270
18	10.5	-245
19	11.8	-222
20	13.1	-201
FREE SPACE		
10	1.6	-656
11	2.0	-586
12	2.4	-526
13	2.8	-475
14	3.2	-431
15	3.7	-391
16	4.3	-356
17	4.9	-324
18	5.5	-295
19	6.2	-268
20	6.9	-243

APPENDIX C

CROSSED LOOP RADIATION PATTERNS

HFDF SSL 5FT CROSSED LOOP OVER PERFECT GROUND
ELEVATION PATTERN (2MHZ)

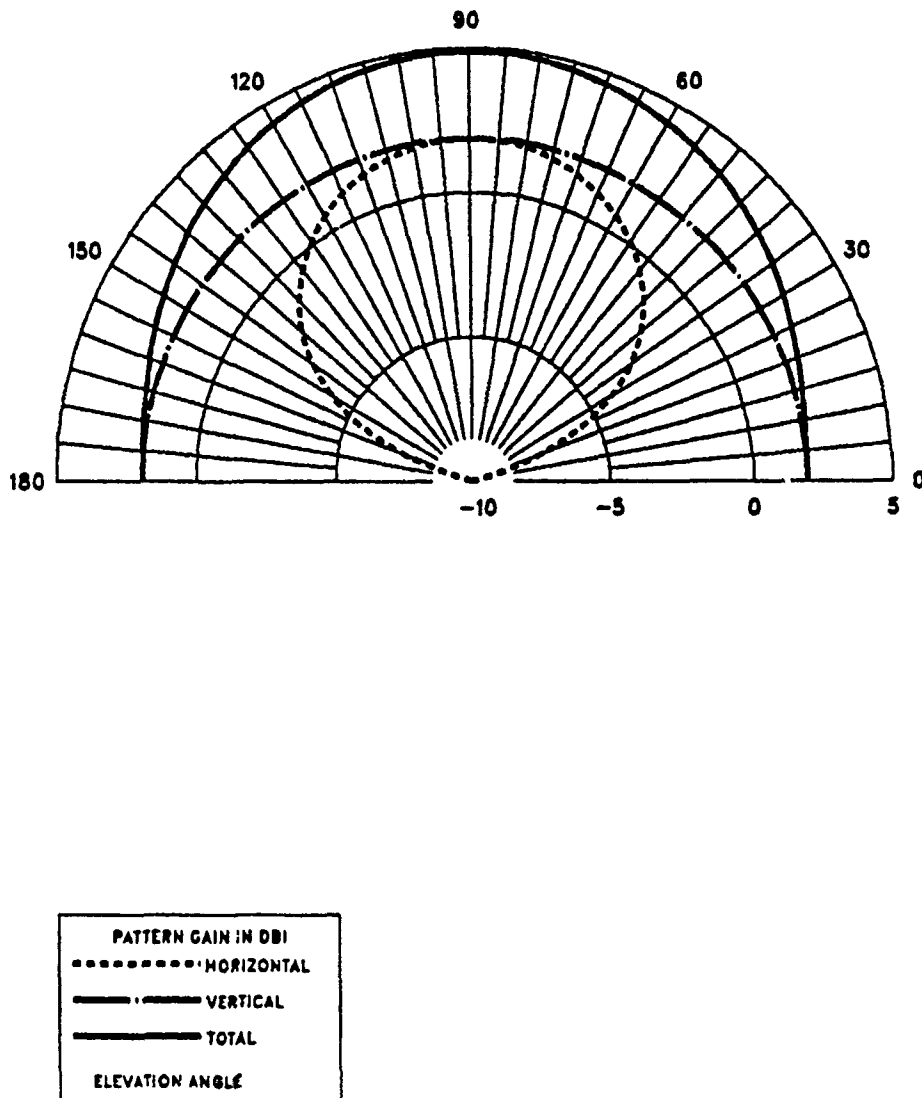


Figure C-1

HFDF SSL 5FT CROSSED LOOP OVER GOOD GROUND
ELEVATION PATTERN (2MHZ, EPS=30, SIG=0.01)

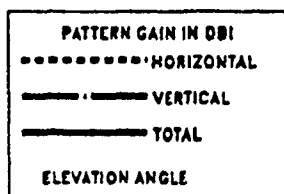
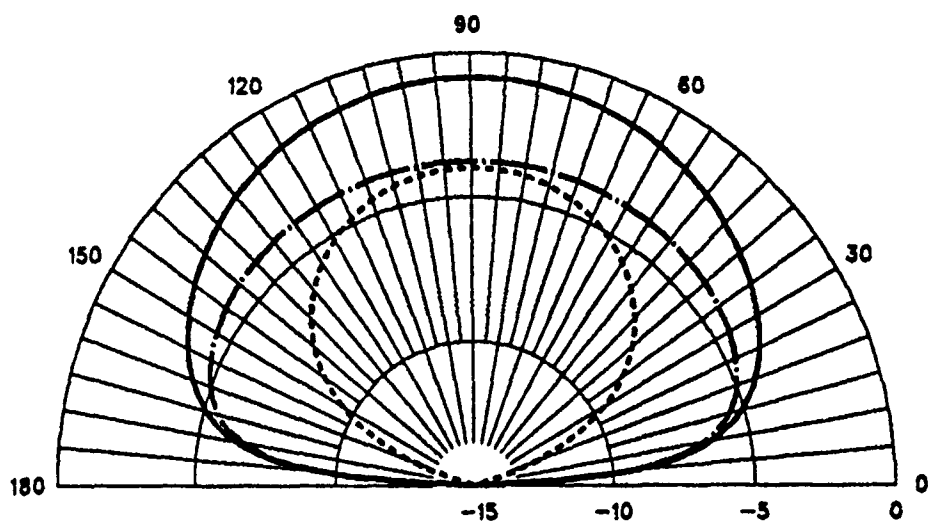


Figure C-2

HFDF SSL 5FT CROSSED LOOP OVER POOR GROUND
ELEVATION PATTERN (2MHZ, EPS=5, SIG=0.001)

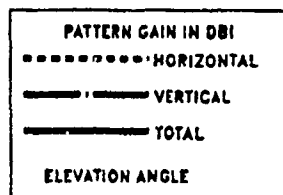
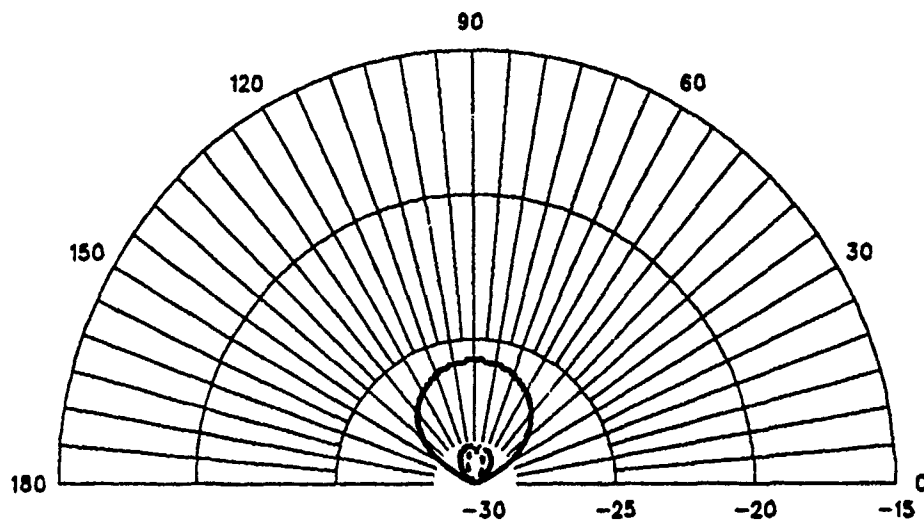


Figure C-3

HFDF SSL 5FT CROSSED LOOP OVER PERFECT GROUND
ELEVATION PATTERN (5MHZ)

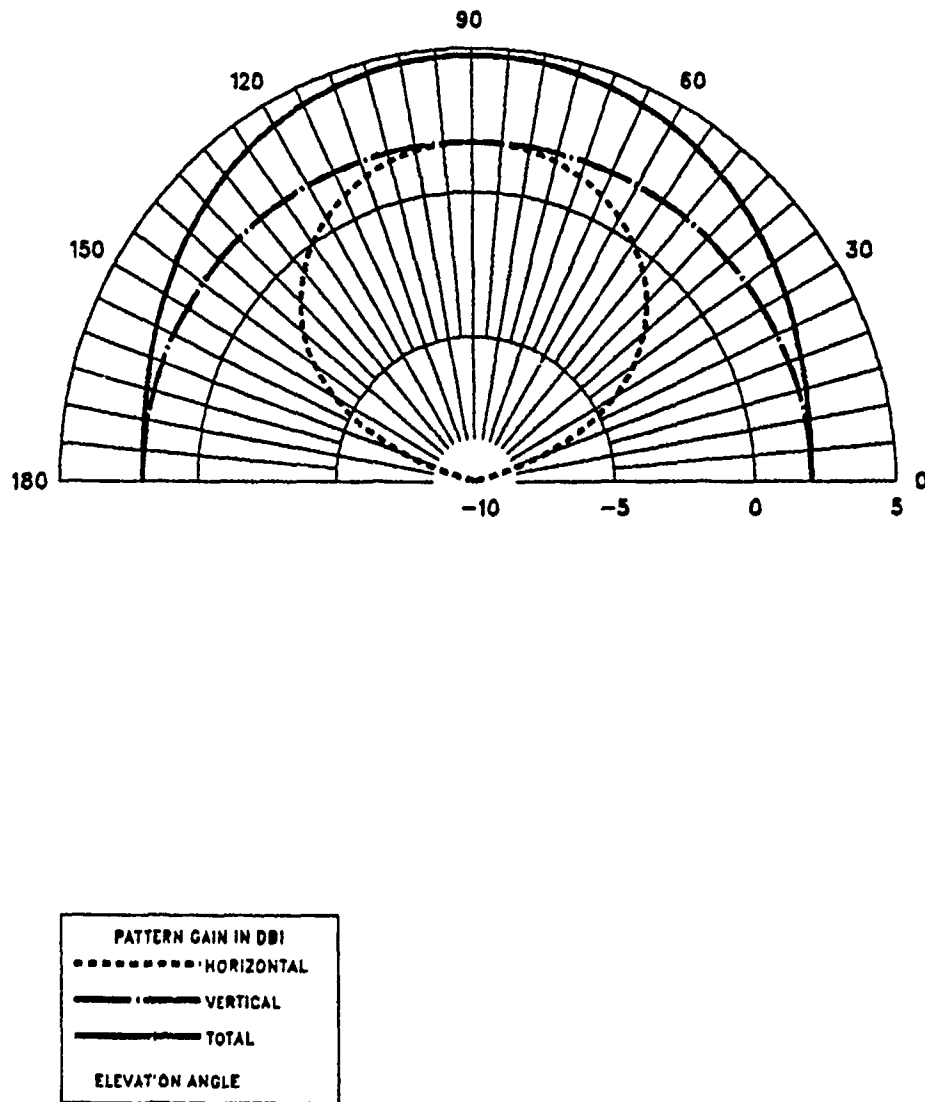


Figure C-4

HFDF SSL 5FT CROSSED LOOP OVER GOOD GROUND
ELEVATION PATTERN (5MHZ, EPS=30, SIG=0.01)

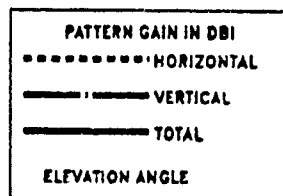
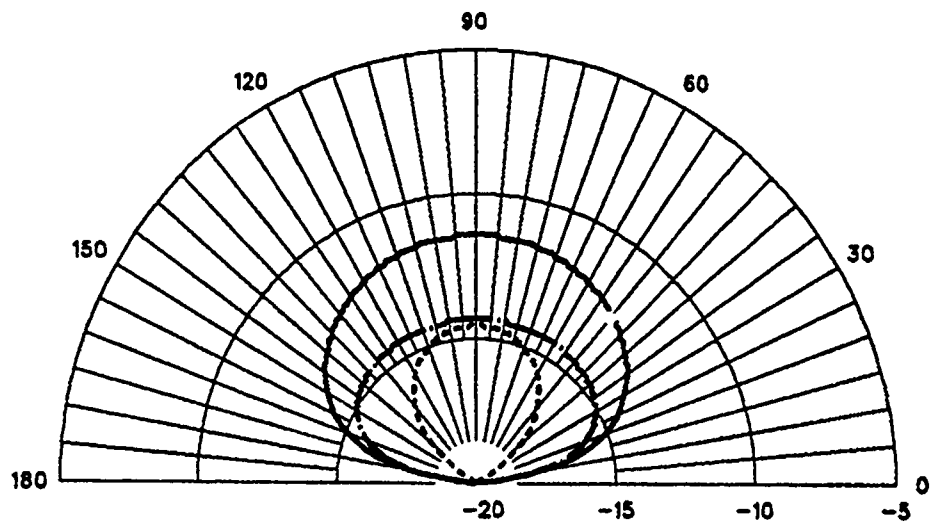


Figure C-5

HFDF SSL 5FT CROSSED LOOP OVER POOR GROUND
ELEVATION PATTERN (5MHZ, EPS=5, SIG=0.001)

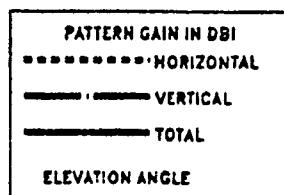
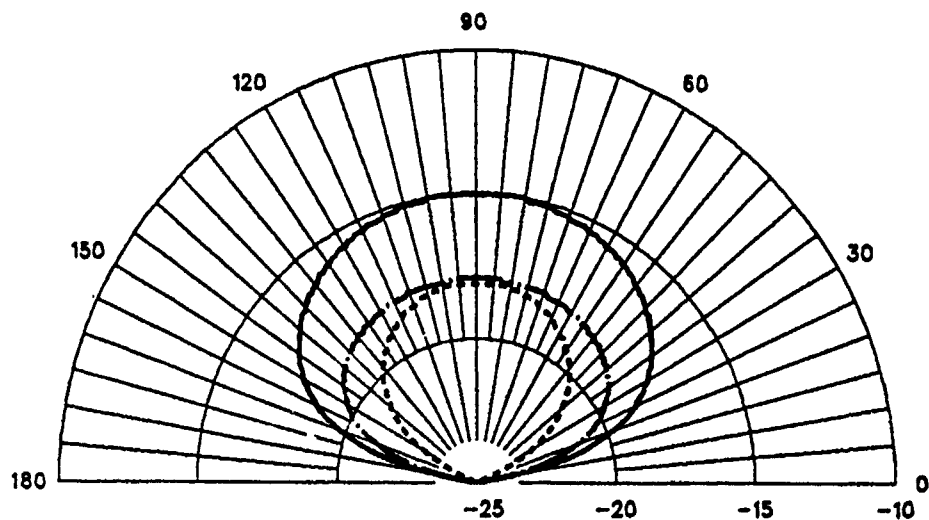


Figure C-6

HFDF SSL 5FT CROSSED LOOP OVER PERFECT GROUND
ELEVATION PATTERN (10MHZ)

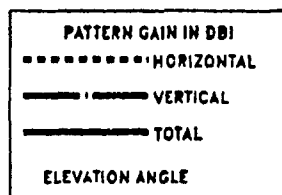
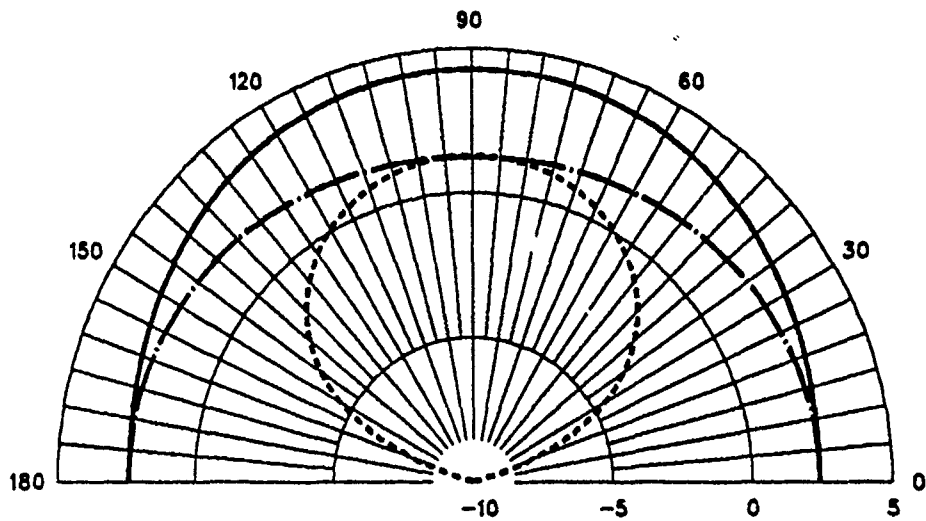


Figure C-7

HFDF SSL 5FT CROSSED LOOP OVER GOOD GROUND
ELEVATION PATTERN (10MHZ, EPS=30, SIG=0.01)

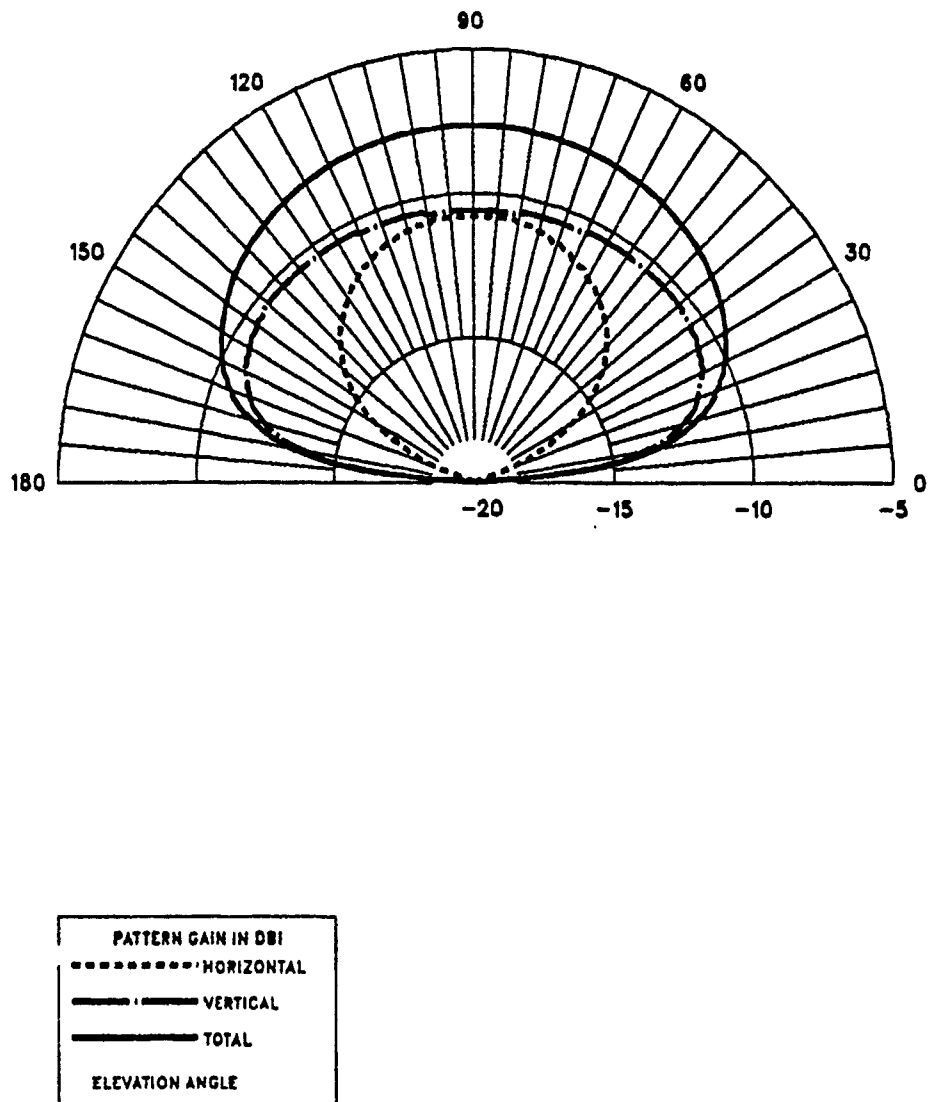


Figure C-8

HFDF SSL 5FT CROSSED LOOP OVER POOR GROUND
ELEVATION PATTERN (10MHZ, EPS=5, SIG=0.001)

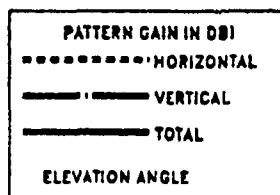
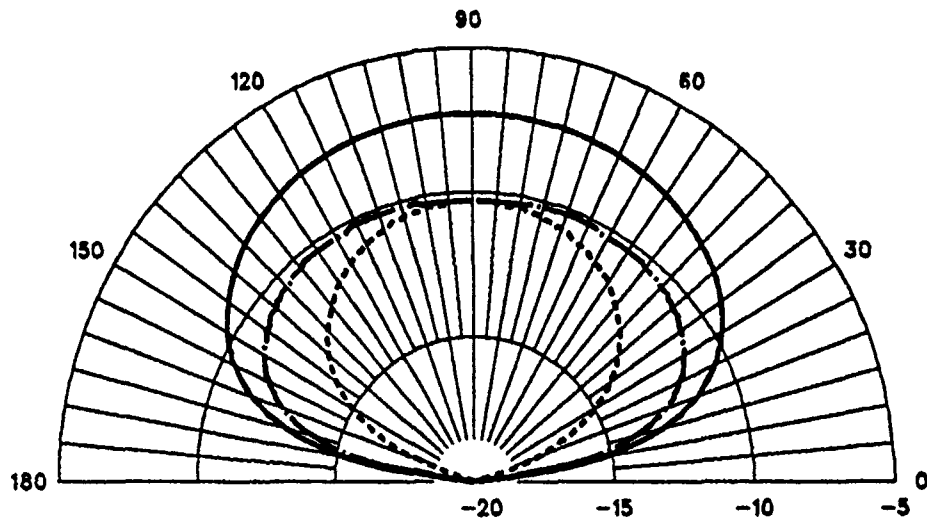


Figure C-9

HFDF SSL 5FT CROSSED LOOP OVER PERFECT GROUND
HORIZONTAL PATTERN (5MHZ)

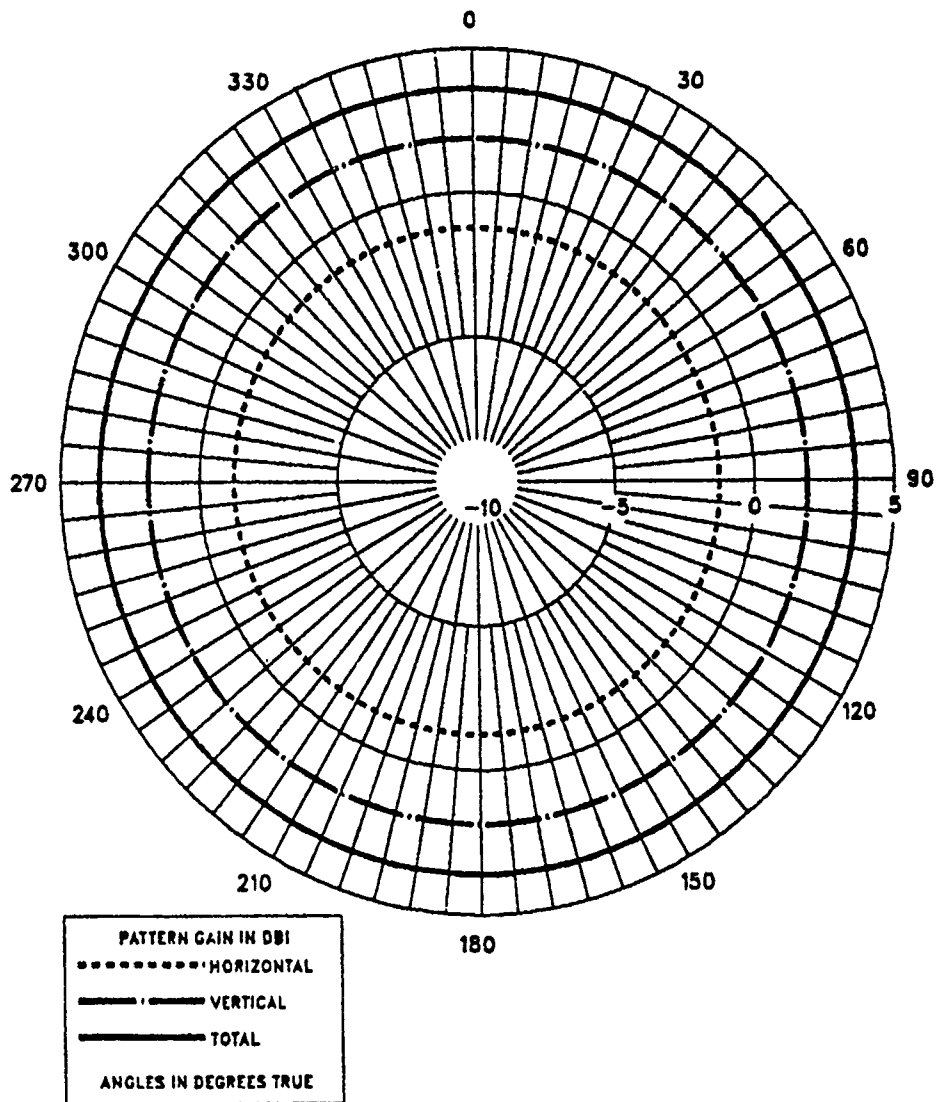


Figure C-10

APPENDIX D

VERTICAL MONOPOLE RADIATION PATTERNS

HFDF SSL 6FT MONOPOLE, 6FT SQ WIRE MESH, OVER PERFECT GROUND
ELEVATION PATTERN (10MHZ)

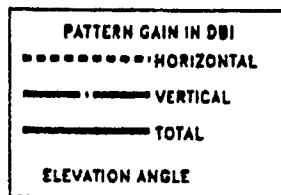
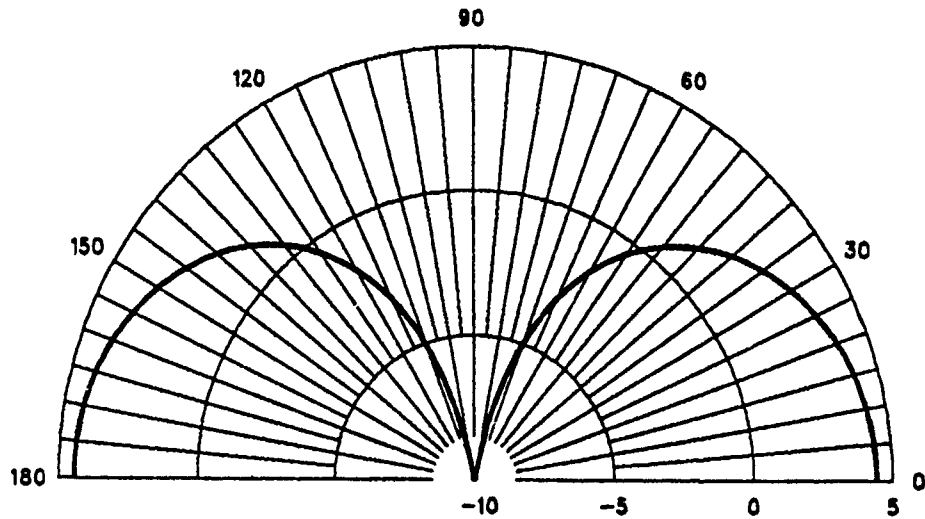


Figure D-1

HFDF SSL 6FT MONOPOLE, 6FT SQ WIRE MESH, OVER GOOD GROUND
ELEVATION PATTERN (10MHZ, EPS=30, SIG=0.01)

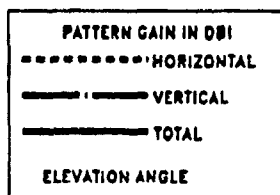
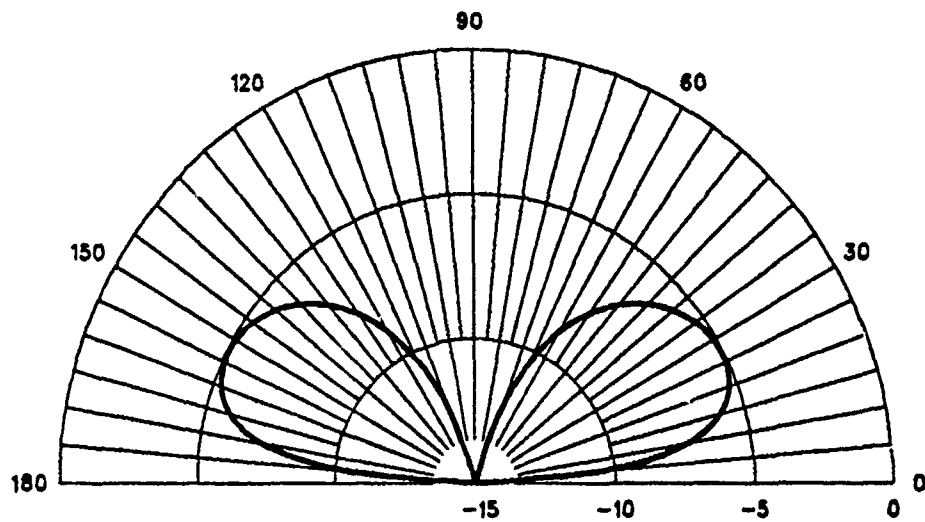


Figure D-2

HFDF SSL 6FT MONOPOLE, 6FT SQ WIRE MESH, OVER POOR GROUND
ELEVATION PATTERN (10MHZ, EPS=5, SIG=0.001)

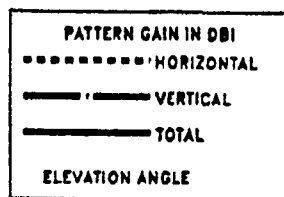
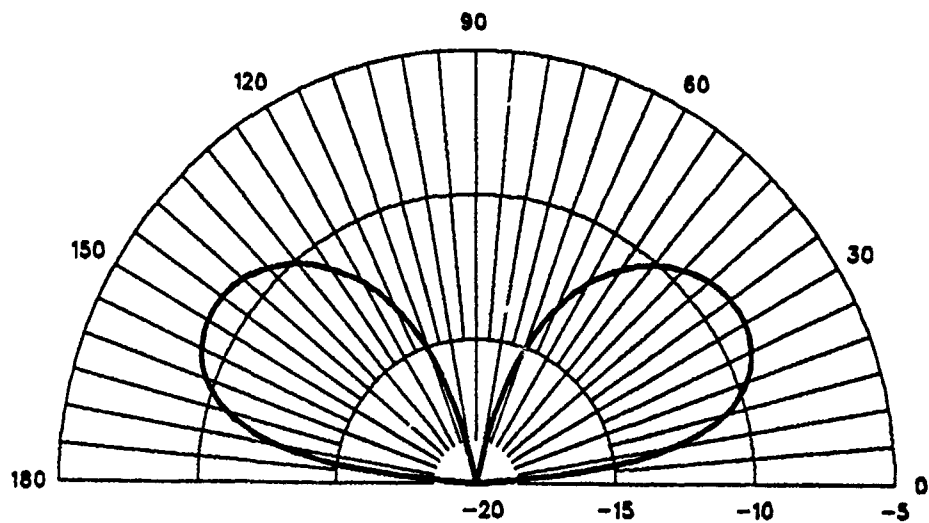


Figure D-3

HFDF SSL 6FT MONOPOLE, 6FT SQ WIRE MESH, OVER PERFECT GROUND
ELEVATION PATTERN (15MHZ)

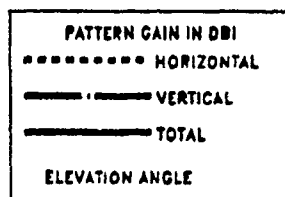
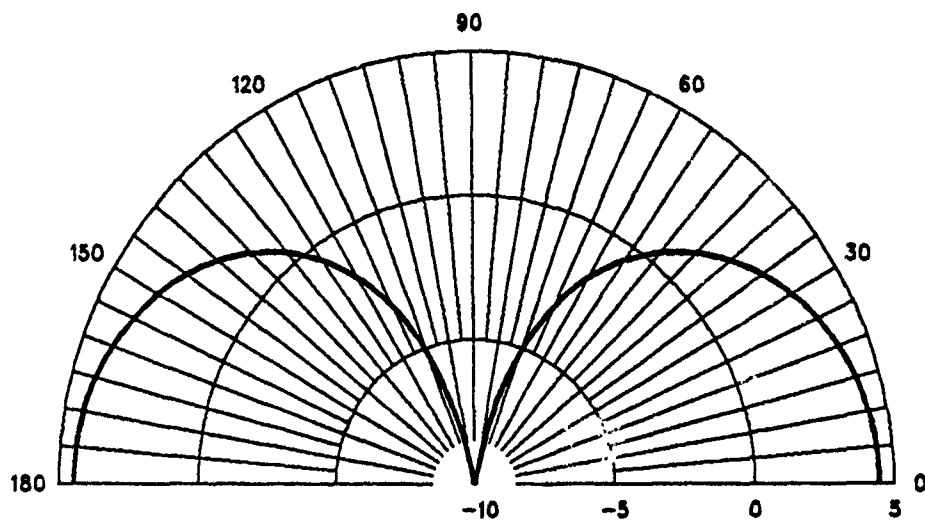


Figure D-4

HFDF SSL 6FT MONOPOLE, 6FT SQ WIRE MESH, OVER GOOD GROUND
ELEVATION PATTERN (15MHZ, EPS=30, SIG=0.01)

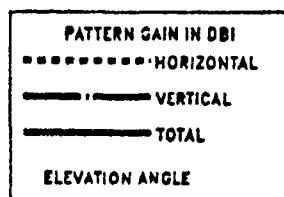
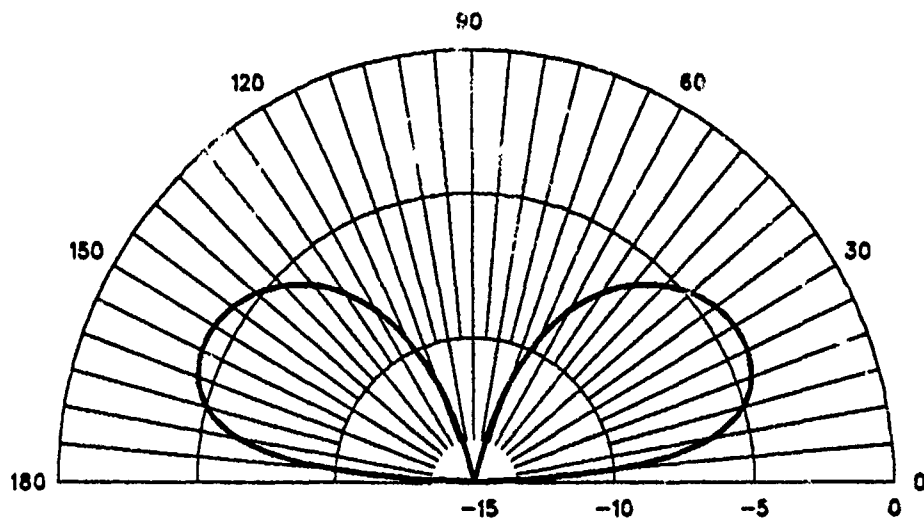


Figure D-5

HFDF SSL 6FT MONOPOLE, 6FT SQ WIRE MESH, OVER POOR GROUND
ELEVATION PATTERN (15MHZ, EPS=5, SIG=0.001)

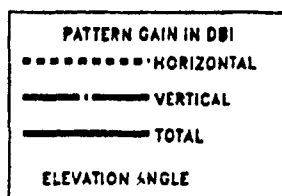
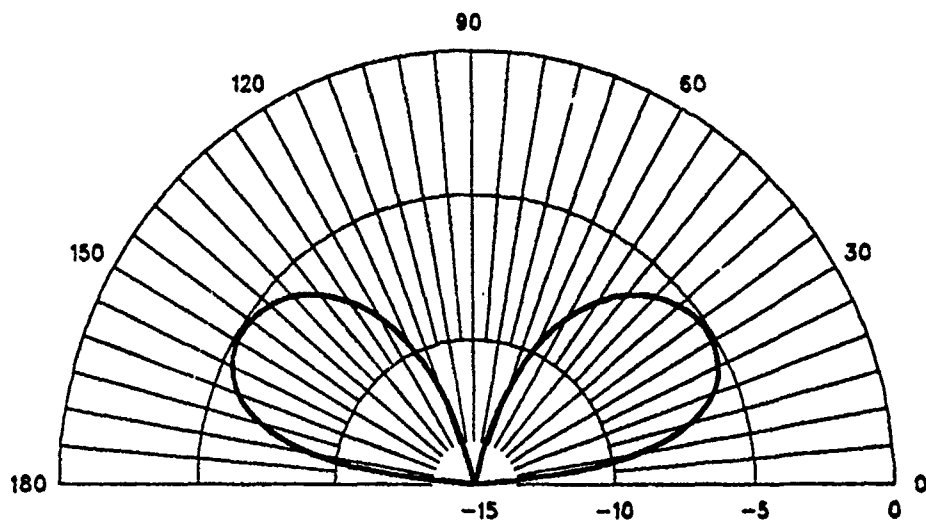


Figure D-6

HFDF SSL 6FT MONOPOLE, 6FT SQ WIRE MESH, OVER PERFECT GROUND
ELEVATION PATTERN (20MHz)

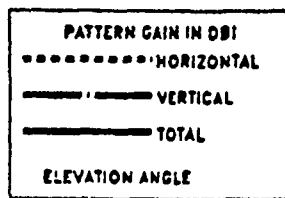
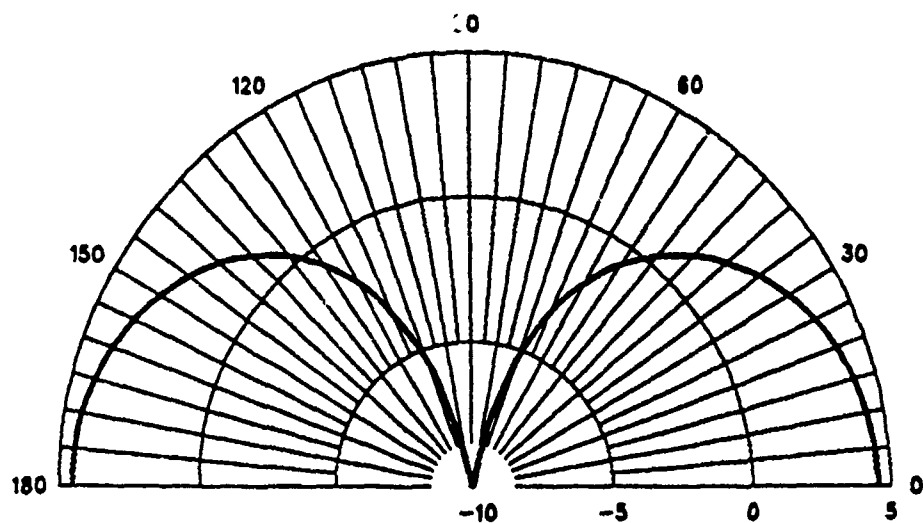


Figure D-7

HFDF SSL 6FT MONOPOLE, 6FT SQ WIRE MESH, OVER GOOD GROUND
ELEVATION PATTERN (20MHZ, EPS=30, SIG=0.01)

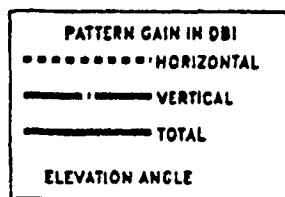
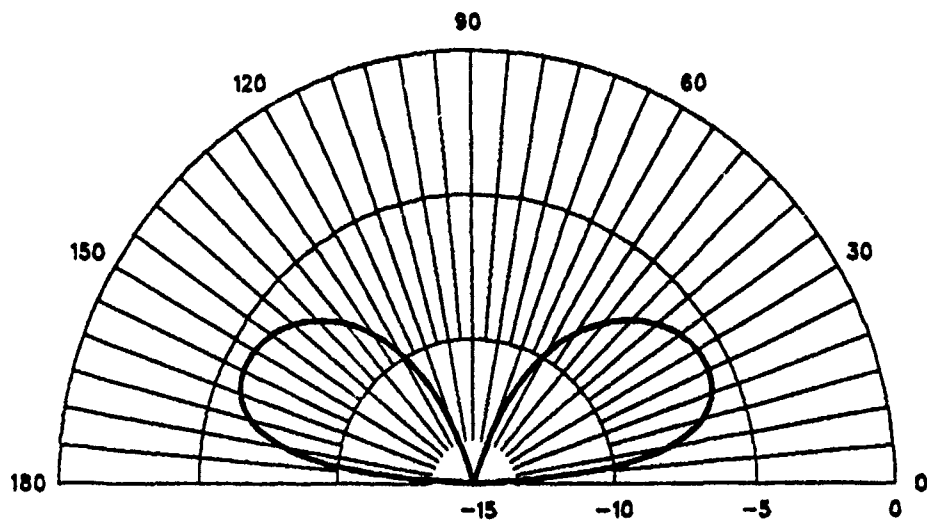


Figure D-8

HFDF SSL 6FT MONOPOLE, 6FT SQ WIRE MESH, OVER POOR GROUND
ELEVATION PATTERN (20MHZ, EPS=5, SIG=0.001)

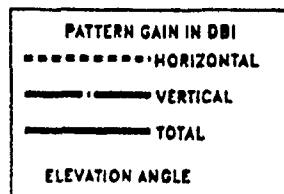
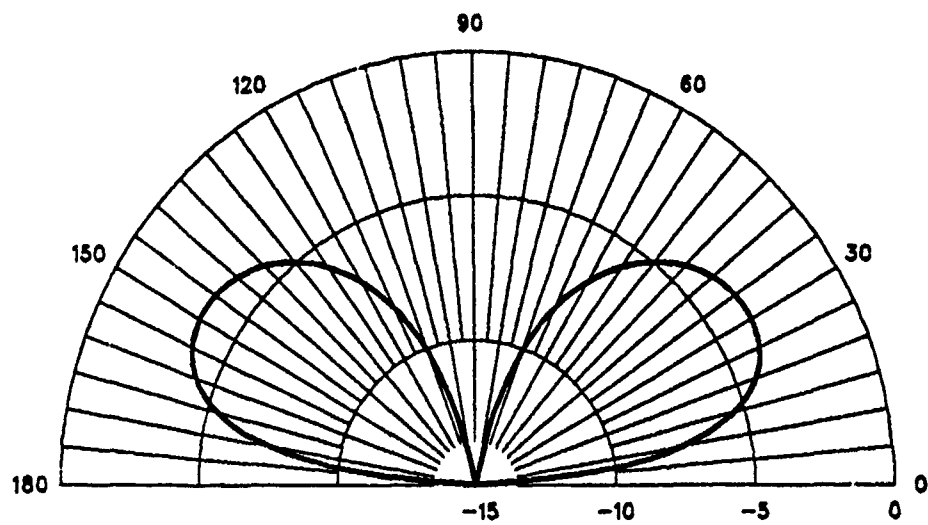


Figure D-9

HFDF SSL 6FT MONOPOLE, 6FT SQ WIRE MESH, OVER PERFECT GROUND
HORIZONTAL PATTERN (15MHZ)

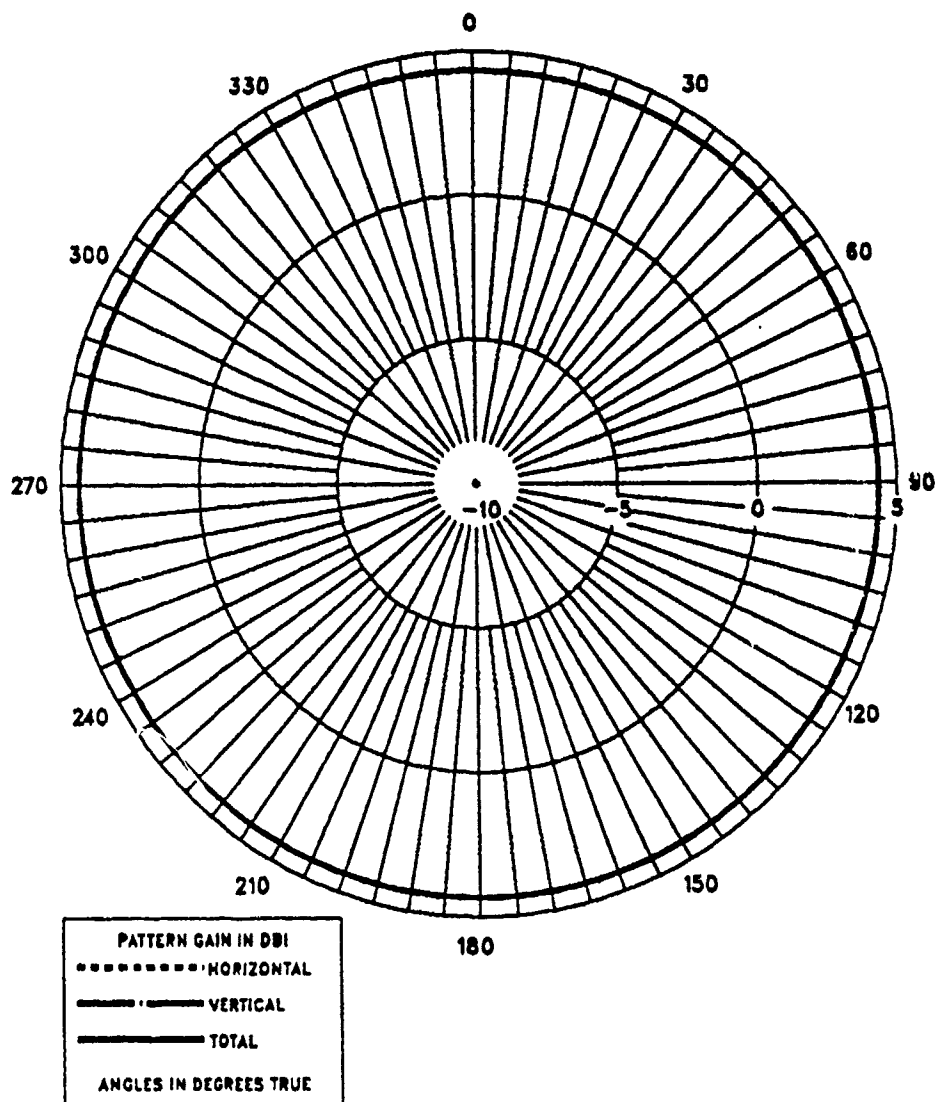


Figure D-10

APPENDIX E

PHASE ERROR ANALYSIS

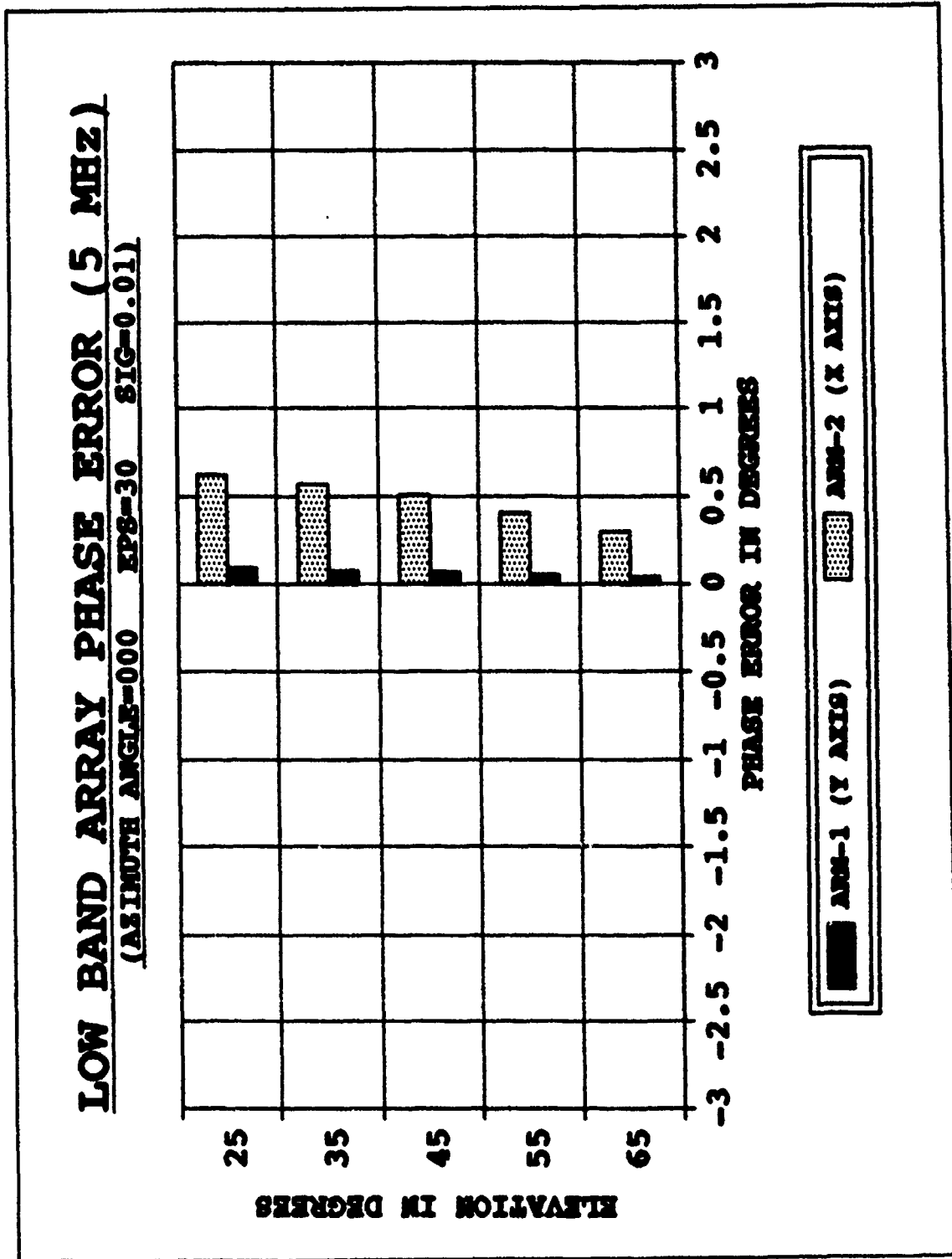


Figure E-1

LOW BAND ARRAY PHASE ERROR (5 MHz) **(ELEVATION ANGLE=045 EP8=30 SIG=0.01)**

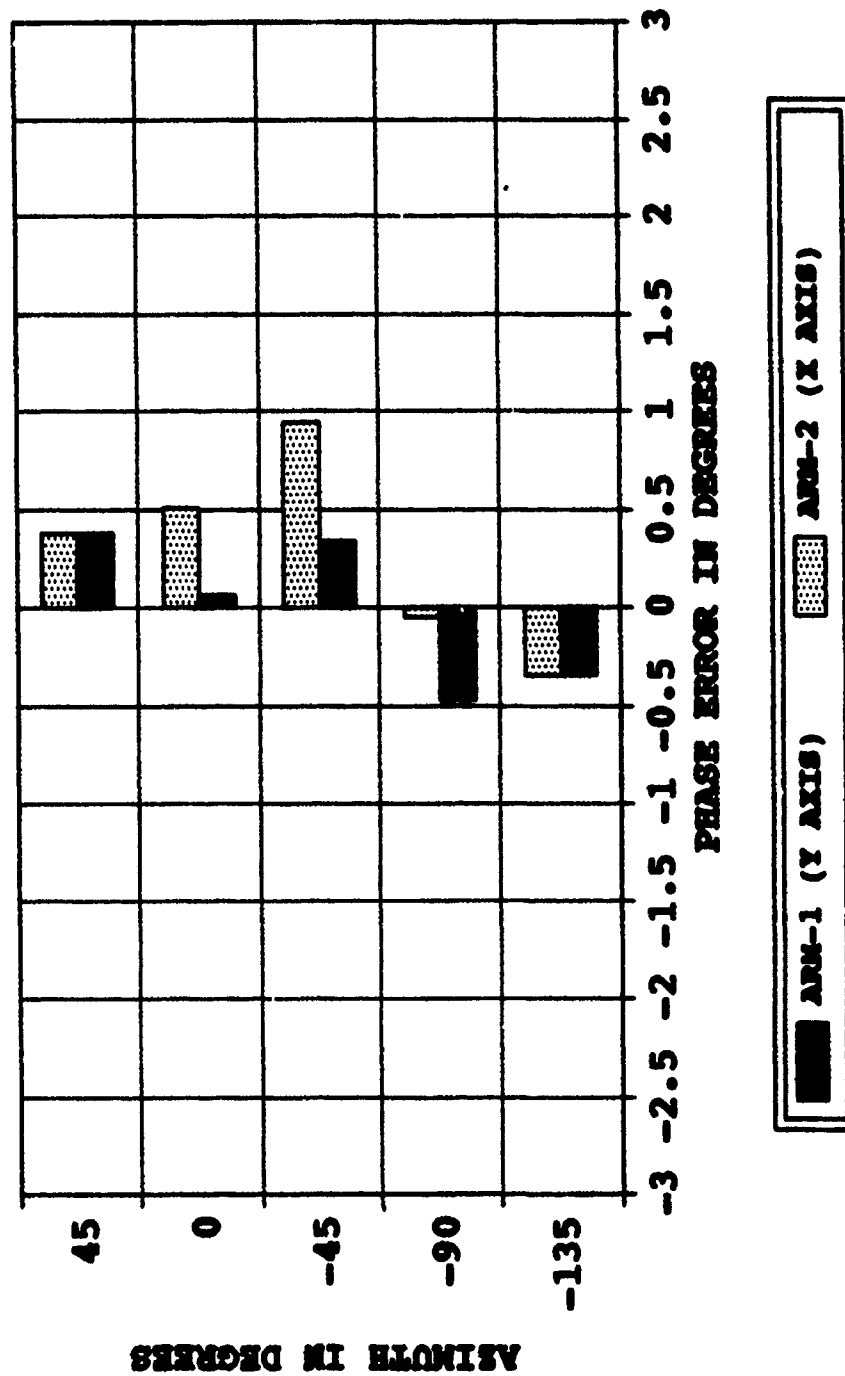


Figure E-2

LOW BAND ARRAY PHASE ERROR (5 MHz)

(AZIMUTH ANGLE=000 EPS=5 SIG=0.001)

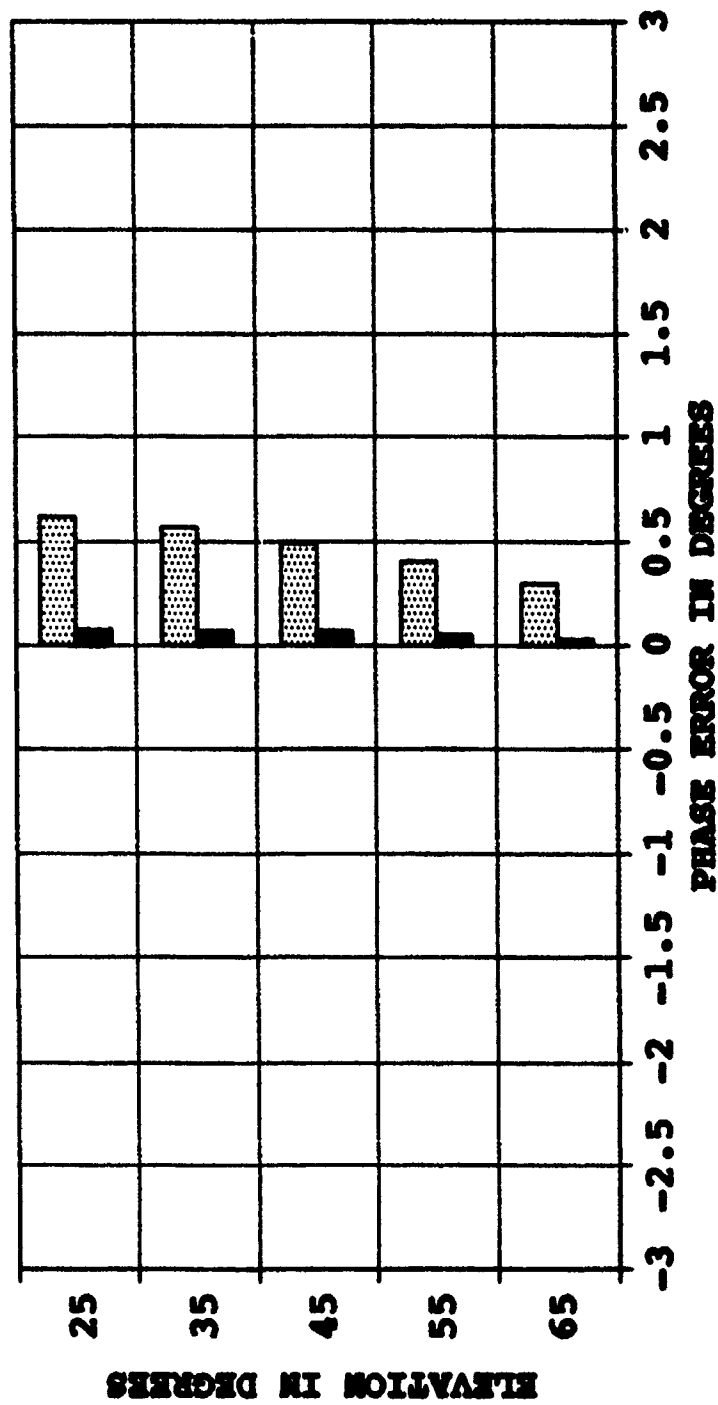


Figure E-3

LOW BAND ARRAY PHASE ERROR (5 MHZ)
(ELEVATION ANGLE=045 EPS=5 SIG=0.001)

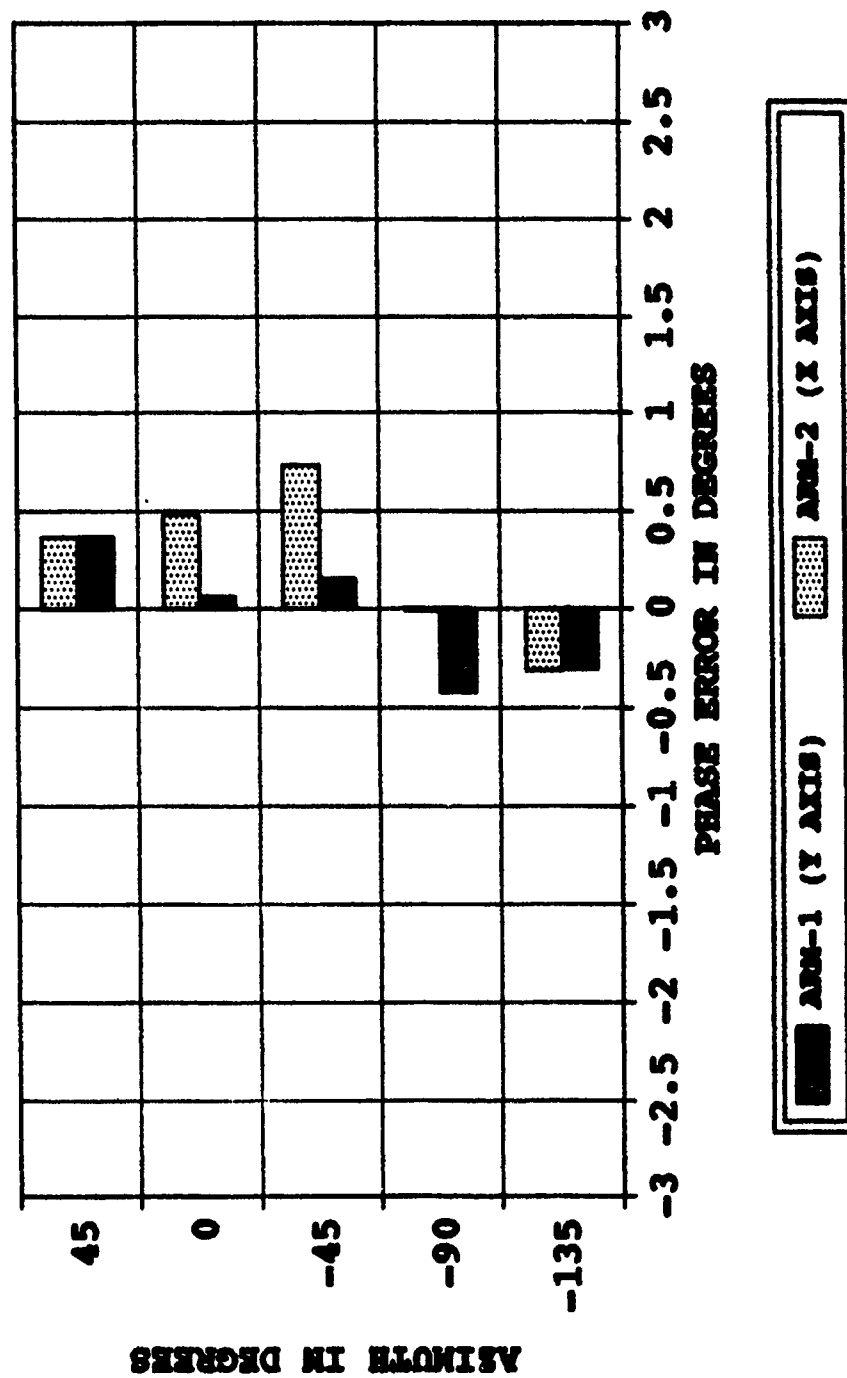


Figure E-4

HIGH BAND ARRAY PHASE ERROR (15 MHZ)

(AZIMUTH ANGLE=000 EPS=30 SIG=0.01)

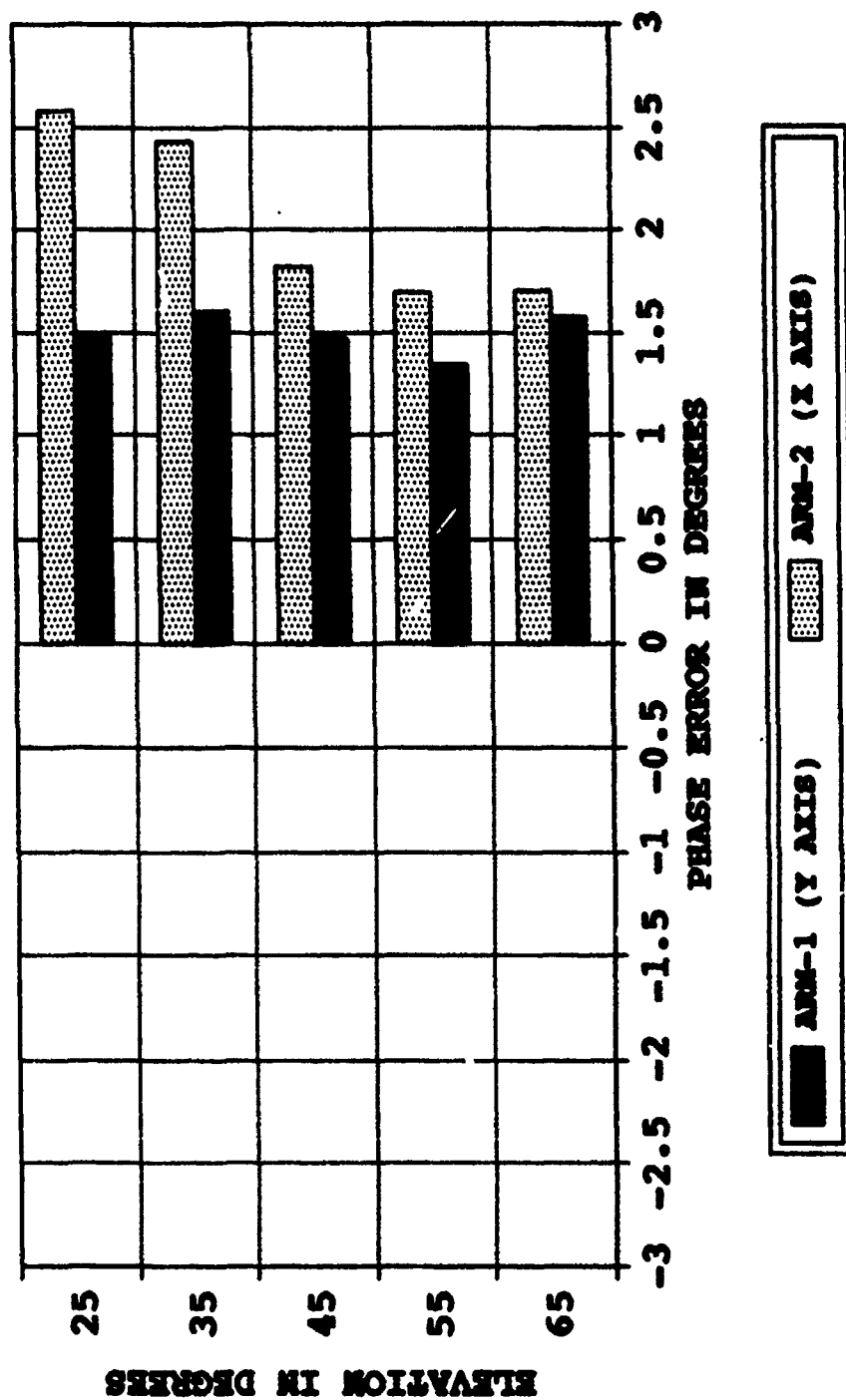


Figure E-5

(ELEVATION ANGLE=045 EPS=30 SIG=0.01)

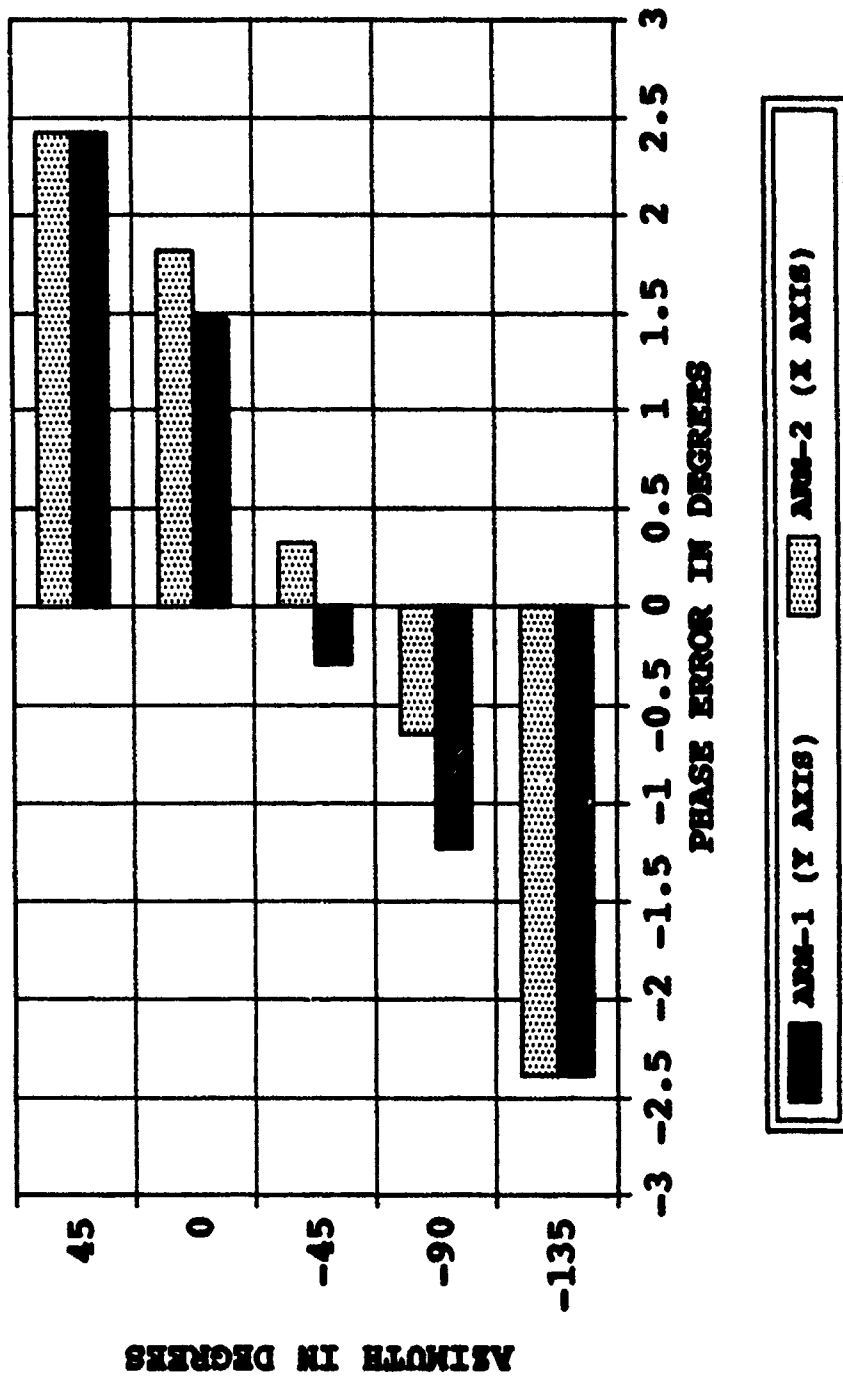


Figure E-6

HIGH BAND ARRAY PHASE ERROR (15 MHZ) **(AZIMUTH ANGLE=000 KP8=5 SIG=0.001)**

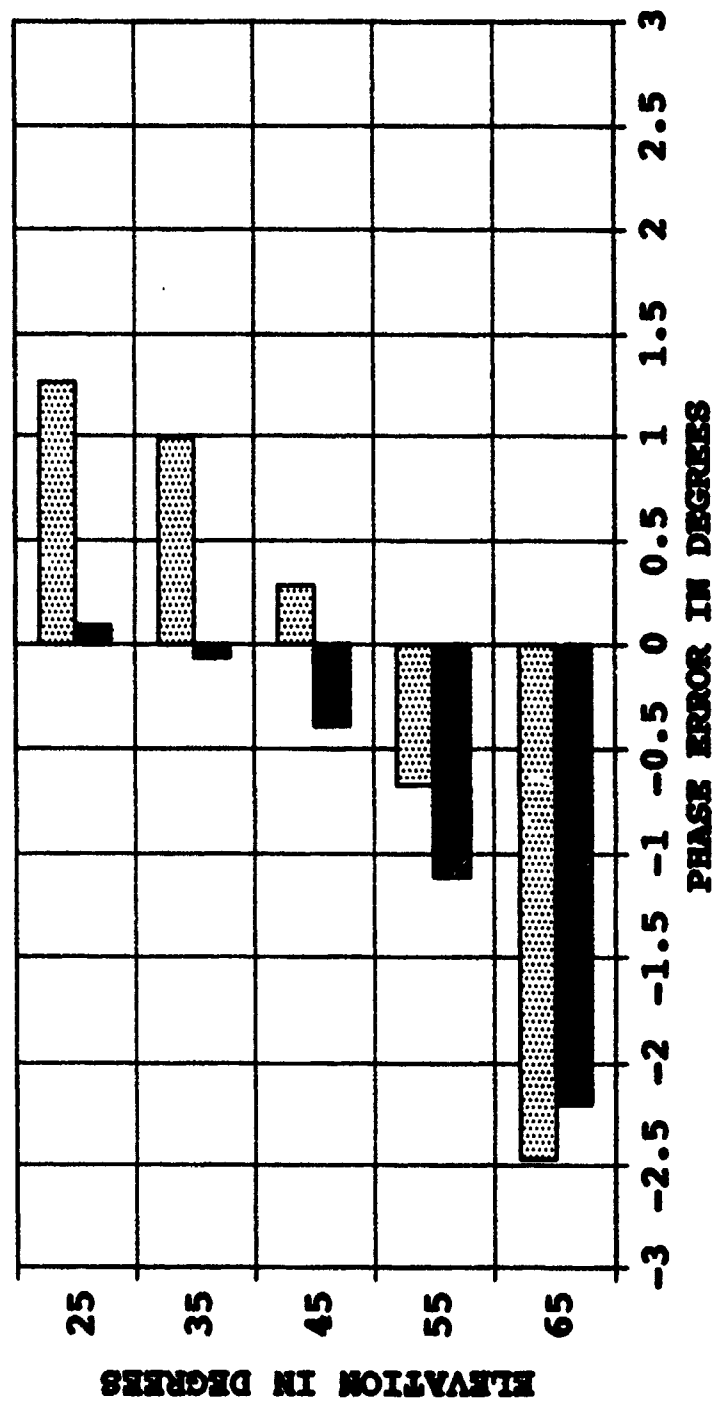


Figure E-7

HIGH BAND ARRAY PHASE ERROR (15 MHZ)

(ELEVATION ANGLE-045 FPS-5 SIG-0.001)

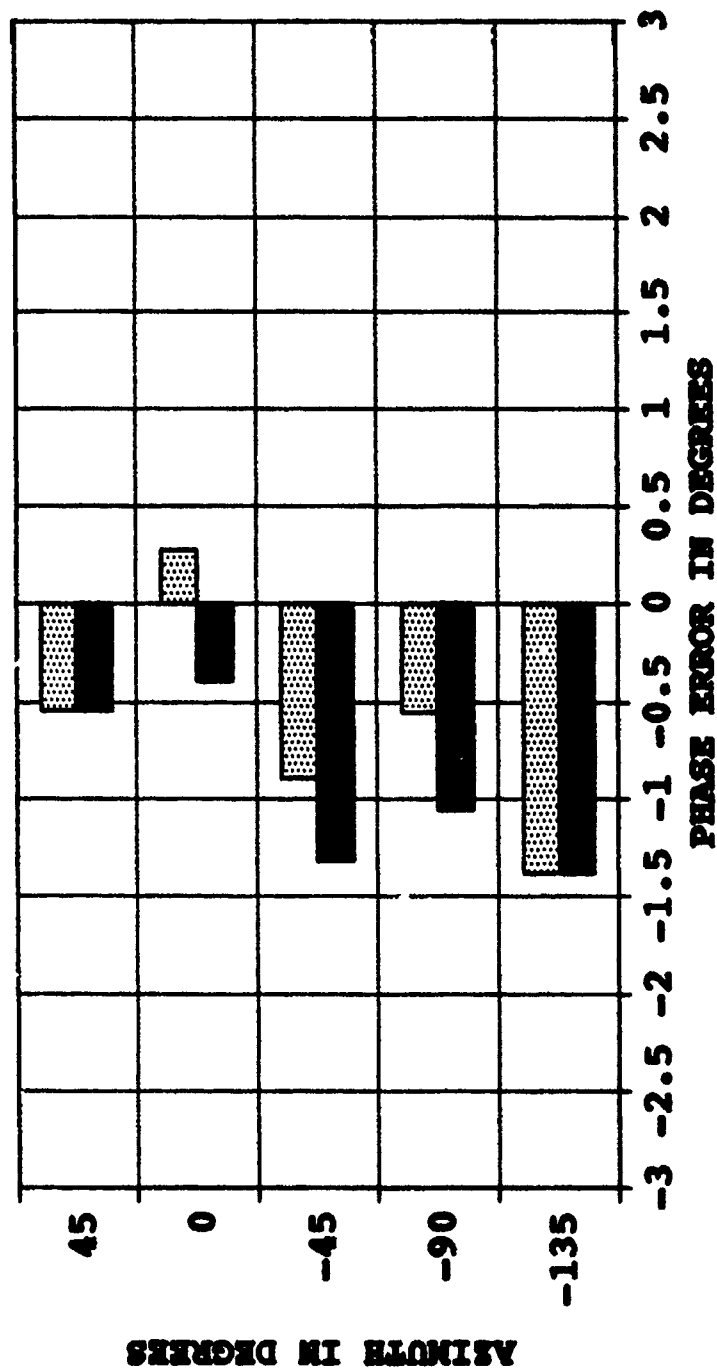


Figure E-8

APPENDIX F

SSL ERROR ANALYSIS

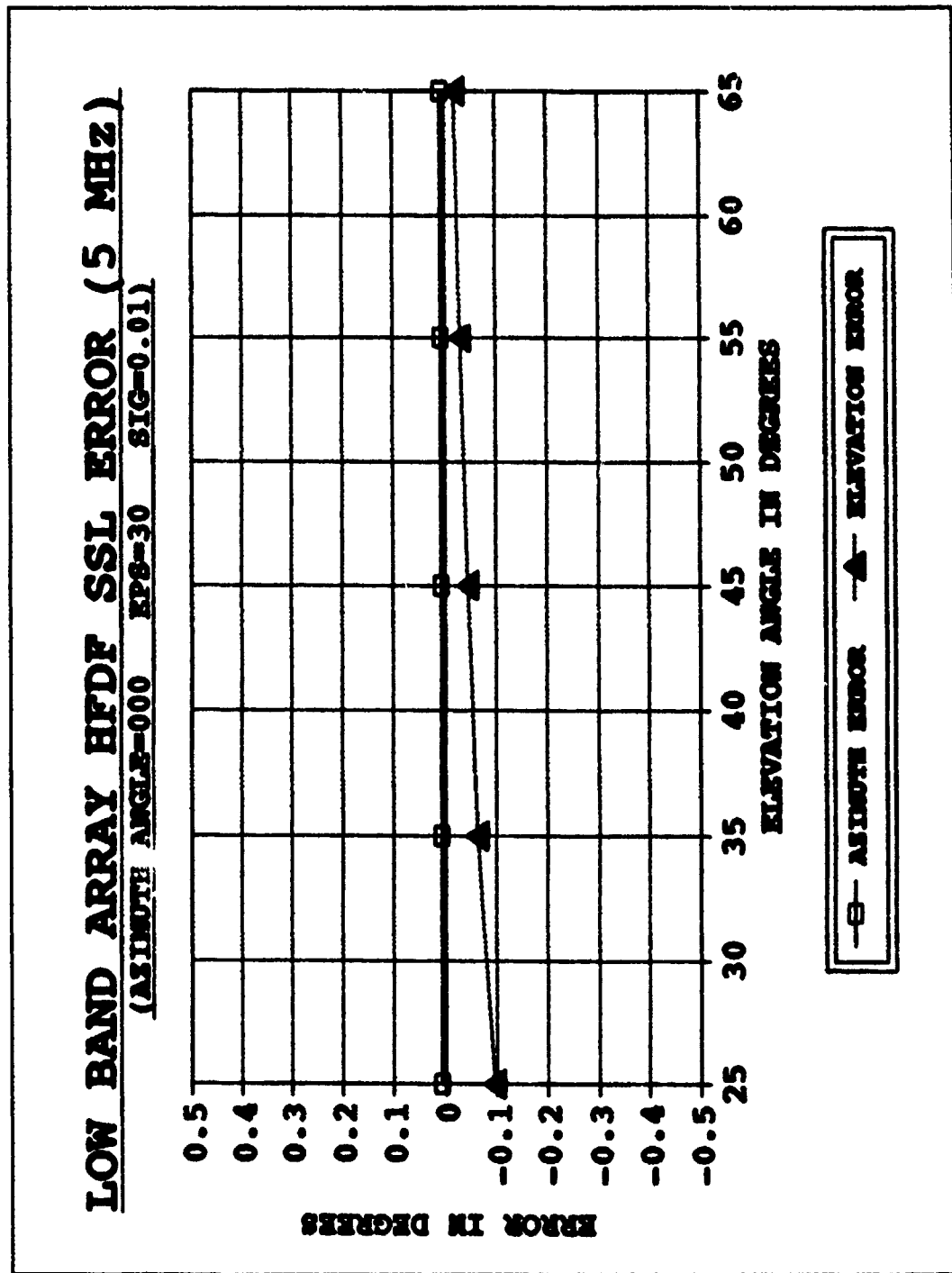


Figure F-1

LOW BAND ARRAY HFDF SSL ERROR (5 MHz)
(ELEVATION ANGLE=045 EPS=30 SIG=0.01)

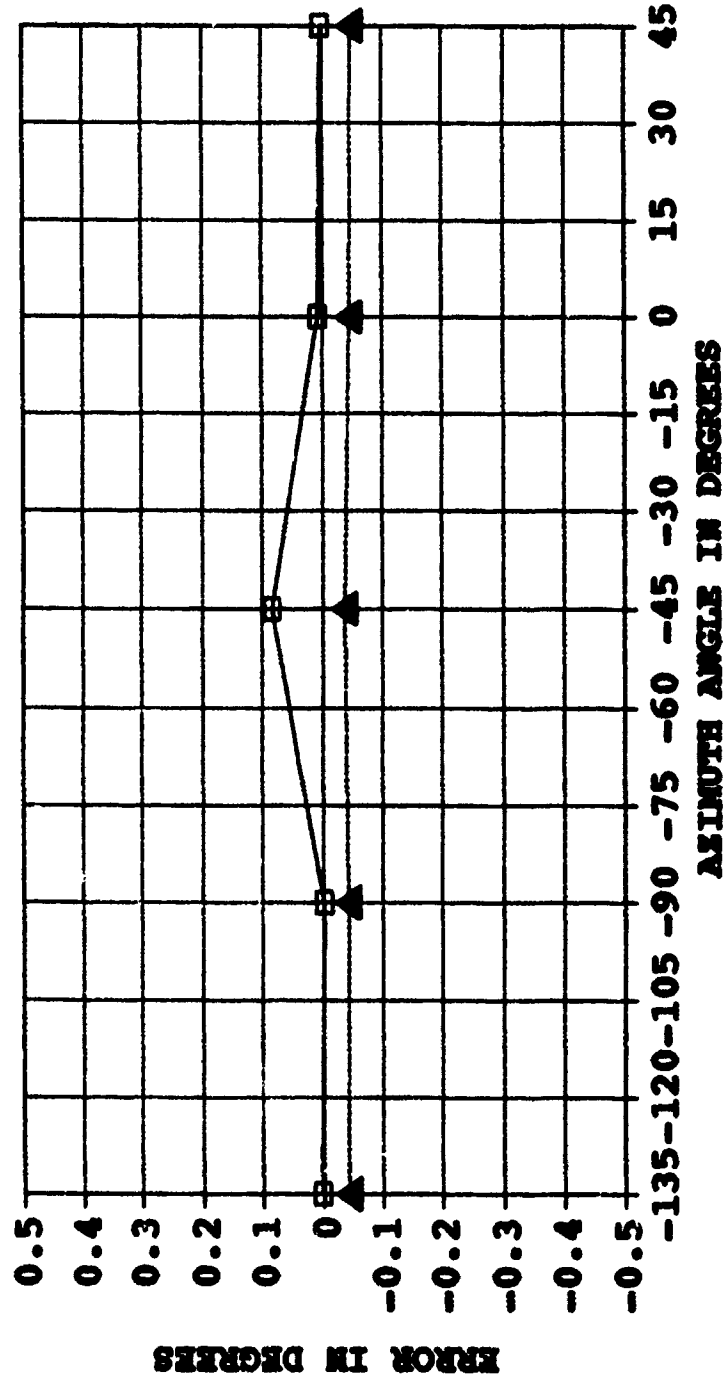
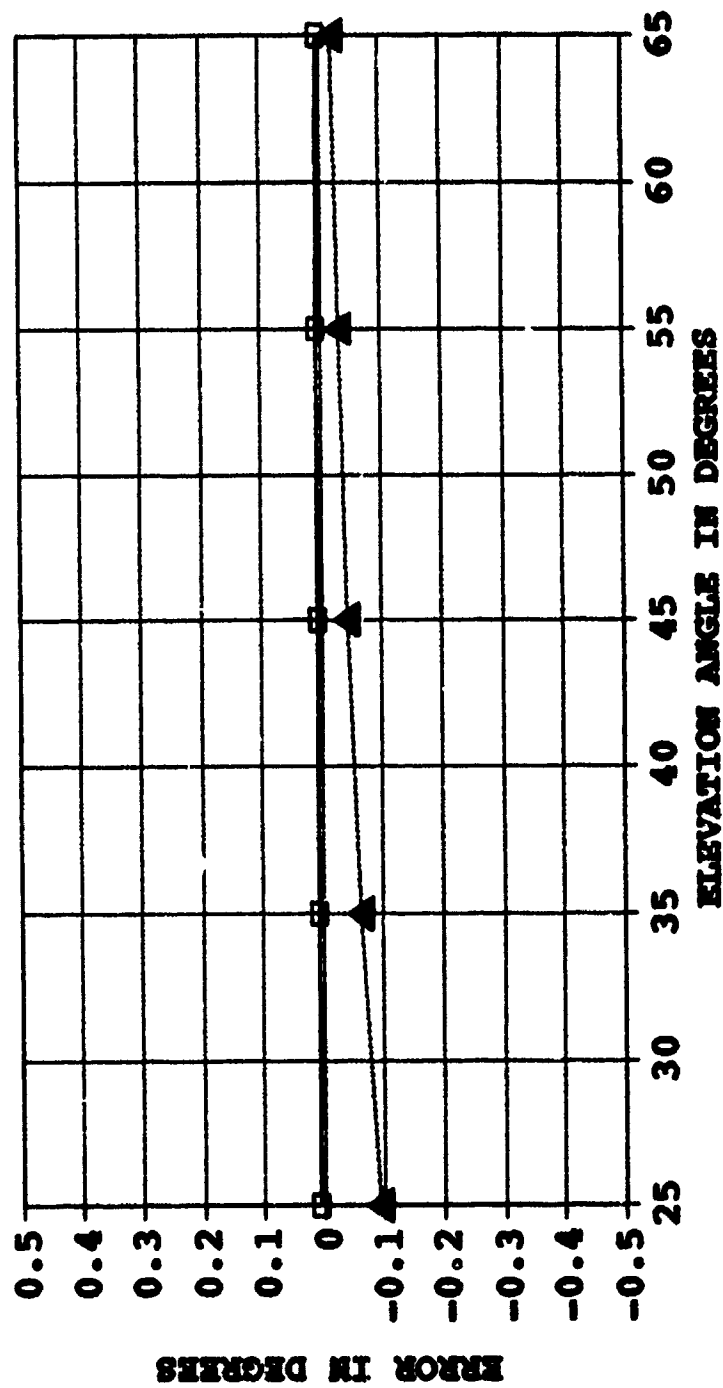


Figure F-2

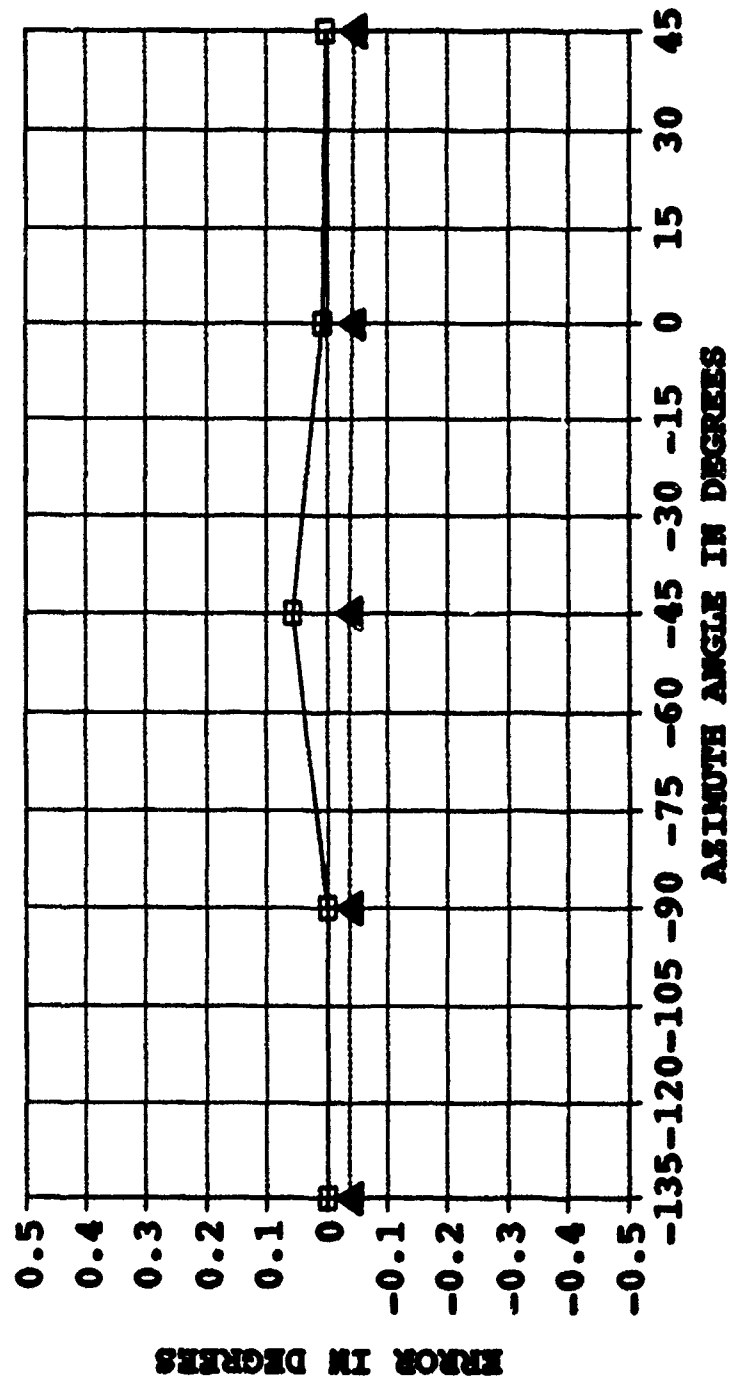
LOW BAND ARRAY HFDF SSL ERROR (5 MHz) **(AZIMUTH ANGLE=000 EPS=5 SIG=0.001)**



—□— AZIMUTH ERROR —▲— ELEVATION ERROR

Figure F-3

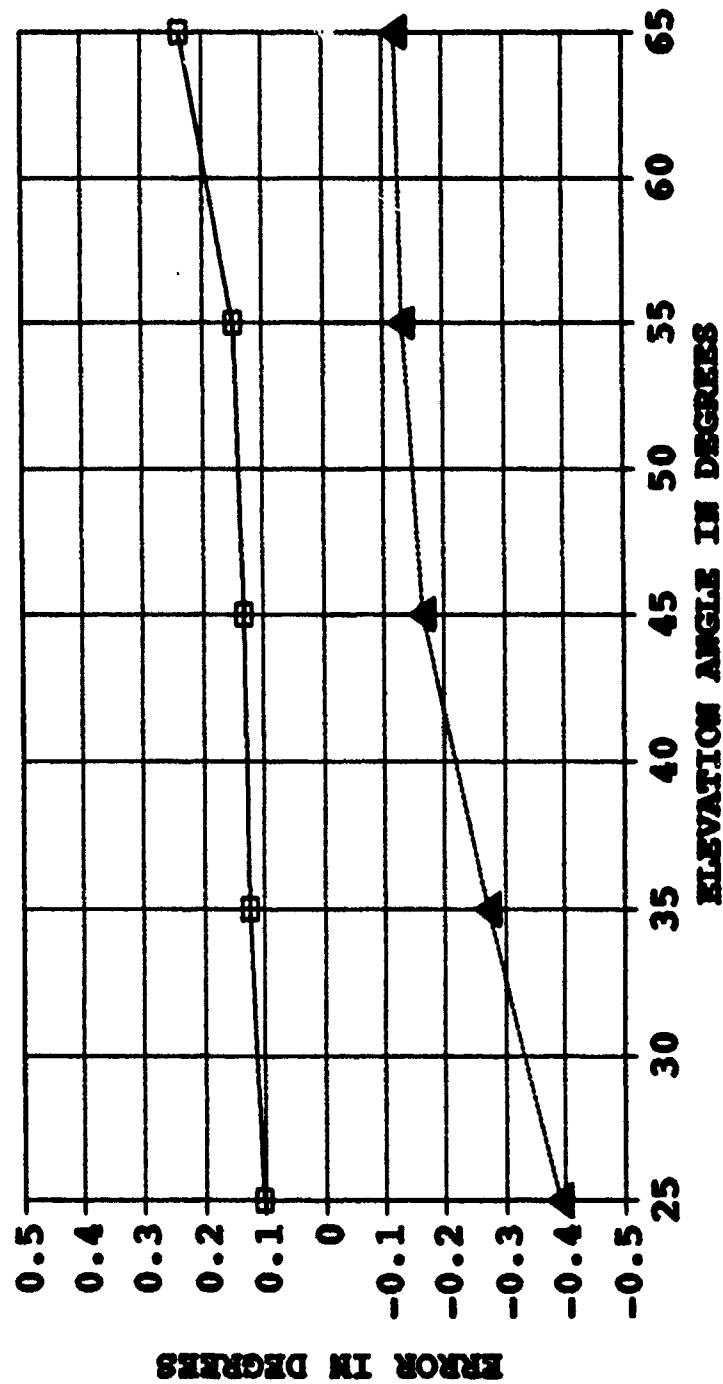
LOW BAND ARRAY HFDF SSL ERROR (5 MHz)
(ELEVATION ANGLE=045 EPS=5 SG=0.001)



—□— AZIMUTH ERROR —▲— ELEVATION ERROR

Figure F-4

(AZIMUTH ANGLE=000 EPS=30 SIG=0.01)

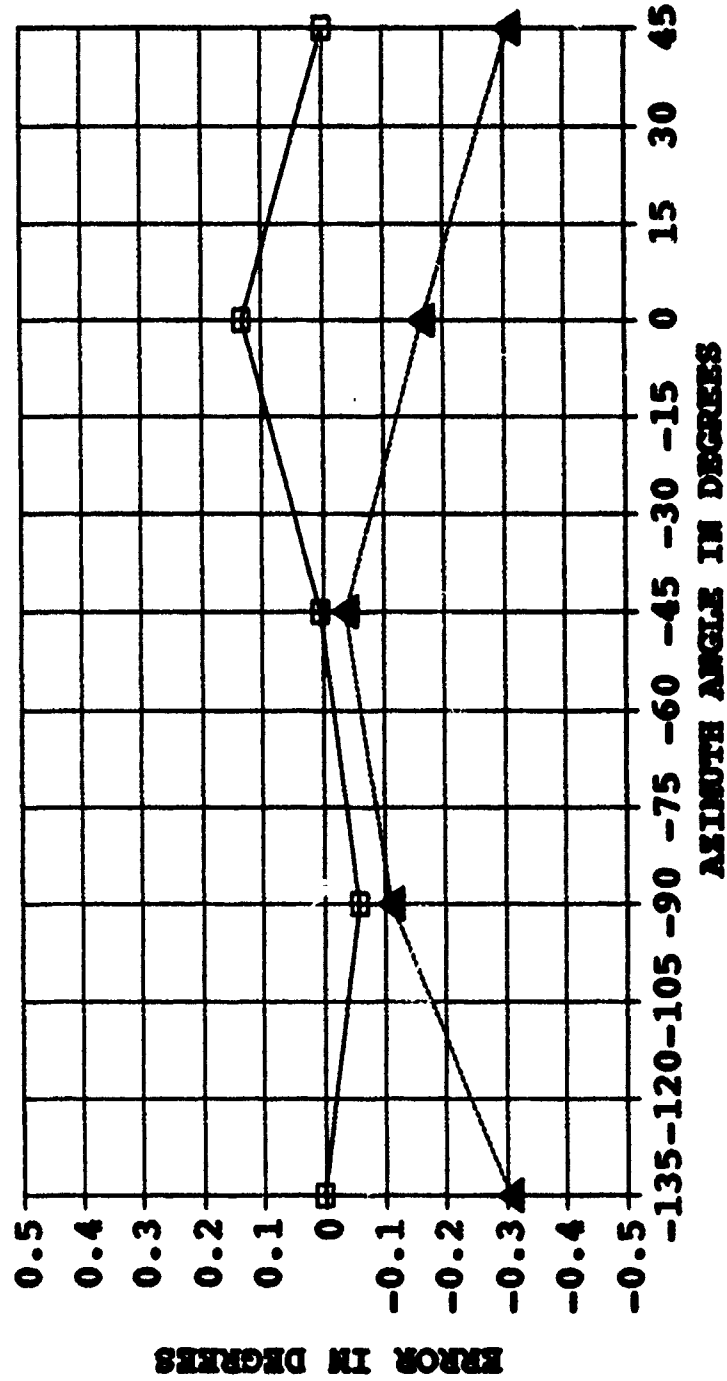


—□— AZIMUTH ERROR —▲— ELEVATION ERROR

Figure F-5

HIGH BAND ARRAY HFDF SSL ERROR (15 MHZ)

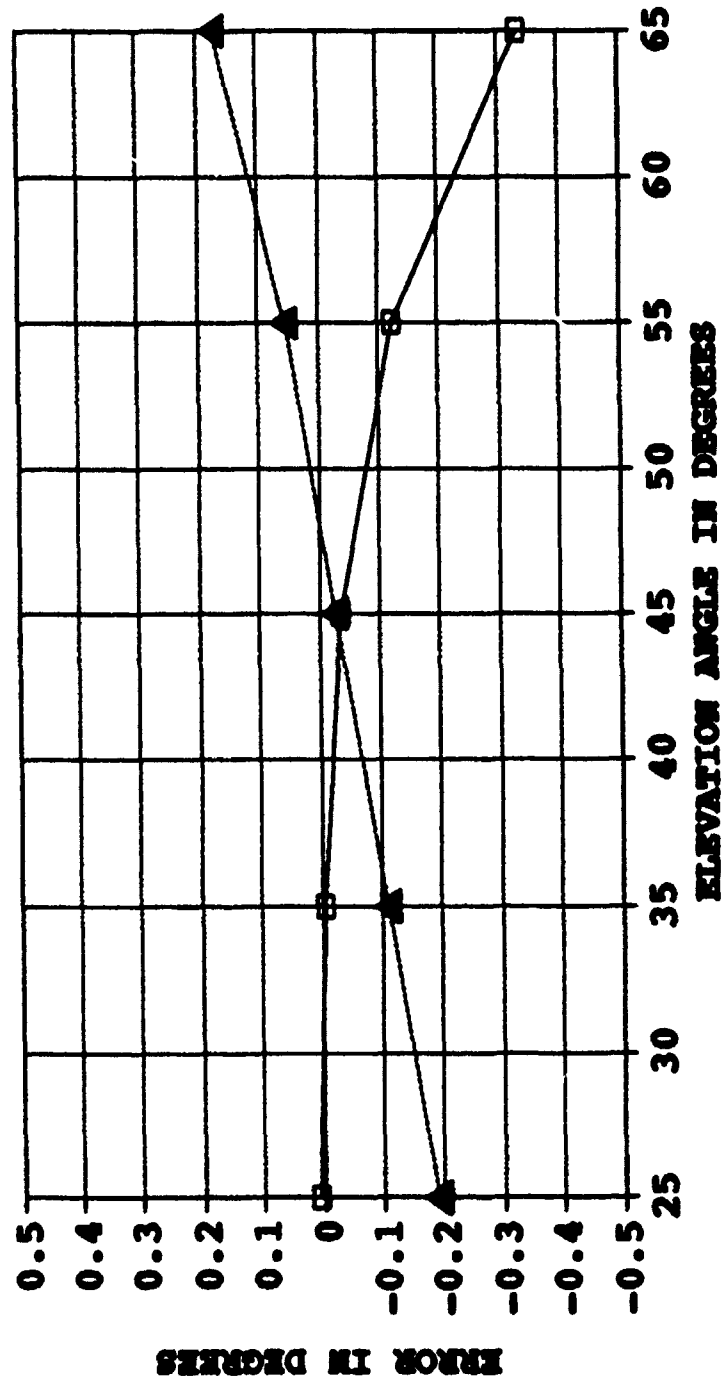
(ELEVATION ANGLE=045 EPS=30 SIG=0.01)



—□— AZIMUTH ERROR —▲— ELEVATION ERROR

Figure F-6

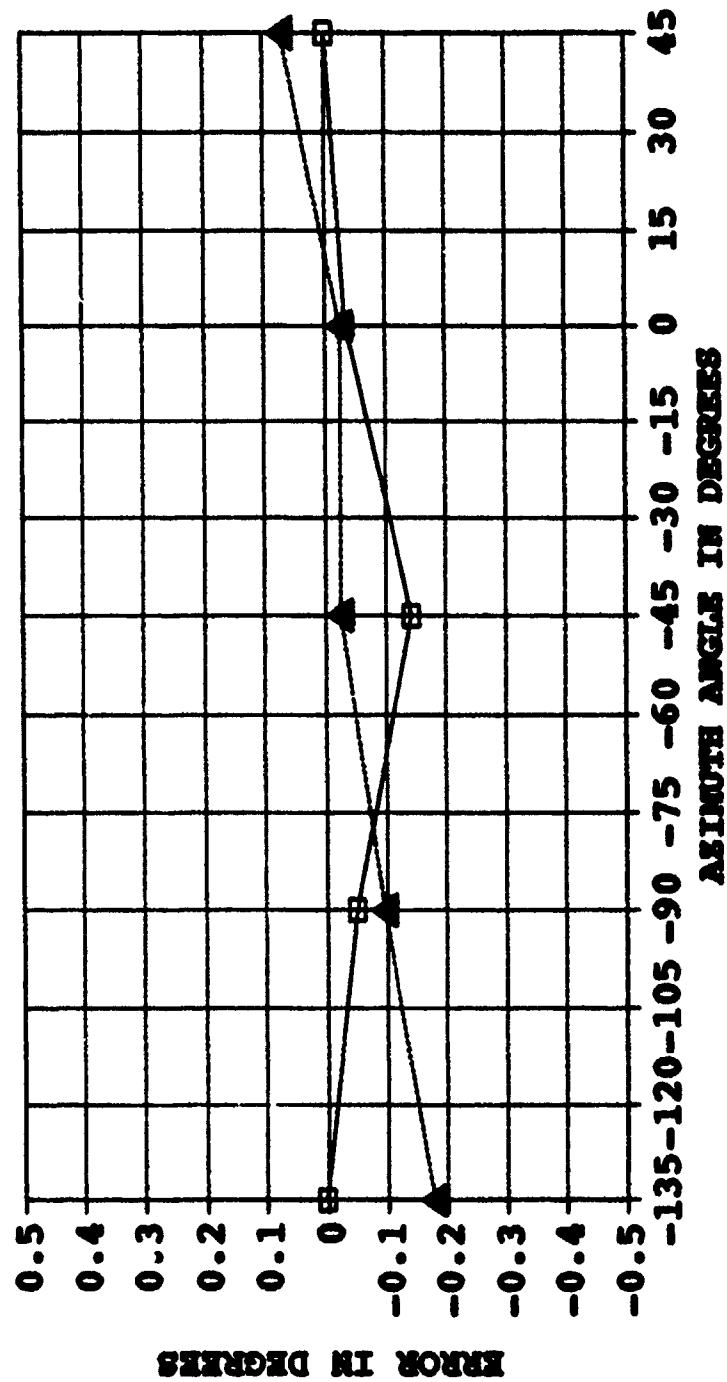
HIGH BAND ARRAY HFDF SSL ERROR (15 MHZ) **(AZIMUTH ANGLE=000 EPS=5 SIG=0.001)**



—□— AZIMUTH ERROR —▲— ELEVATION ERROR

Figure F-7

HIGH BAND ARRAY HFDF SSL ERROR (15 MHZ) **(ELEVATION ANGLE=045 EP8=5 SIG=0.001)**



—□— AZIMUTH ERROR —▲— ELEVATION ERROR

Figure F-8

REFERENCES

- 1) R. Johnson and H. Jasik, *Antenna Engineering Handbook*, McGraw- Hill, New York, 1984.
- 2) P.J.D. Gething, *Radio Direction Finding and the Resolution of Multicomponent Wave-Fields*, Peter Peregrinus LTD., London, 1978.
- 3) R. Groller, "Single station location HF direction finding", *Journal of Electronic Defense*, pp. 58-83, June 1990.
- 4) W. Ross and E.N. Bramley, "Measurements of the direction of arrival of short radio waves reflected at the ionosphere", *Proc. Royal Society*, London, Series A, Vol. 207, p. 251, 1951.
- 5) Conversation between the author and Dr. W.M. Sherrill, Director, Southwest Research Institute (SWRI), San Antonio, Texas June 1990.
- 6) B. Chatterjee, *Propagation of Radio Waves*, Asia Publishing House, New York, 1963.
- 7) Y.A. Zaytsev and Y.K. Kireyev, "Polarization errors in phase-type direction finding", *Radio Engineering*, Vol. 23, pp. 121-126, 1968.
- 8) E.V. Appleton and M.A.F. Barnett, "On some direct evidence for downcoming atmospheric reflection of electric rays", *Proc. Royal Society*, London, Series A, Vol. 109, p. 621, December, 1925.
- 9) R.F. Treharne, C.G. McCue, Z.R. Jeffrey, and B.S. Hewett, "Some characteristics of the propagation of skywaves over short ionospheric paths", *Proc. IREE*, Australia, pp. 245-254, August 1965.
- 10) G.J. Burke and A.J. Poggio, "Numerical Electromagnetics Code (NEC) - Method of Moments", Technical Report No. UCID-18834, Lawrence Livermore Laboratory, January 1981.
- 11) G.J. Burke, "Present capabilities and new developments in antenna modeling with the Numerical Electromagnetics Code NEC", Technical Report N0. UCRL-98107, Lawrence Livermore Laboratory, 1988.
- 12) Letter from Dr. W.M. Sherrill, Director, Southwest Research Institute (SWRI), San Antonio, Texas, to Dr. R.W. Adler, Professor, Naval Postgraduate School, March 30 1990.
- 13) K.H. Awadalla and A.A. Sharshar, "A simple method to determine the impedance of a loop antenna", *IEEE Trans. on Antennas and Propagation*, Vol. 32, No. 11, pp. 1248-1251, November 1984.
- 14) W.L. Stulzman and G.A. Thiele, *Antenna Theory and Design*, John Wiley & Sons, New York, 1981.

INITIAL DISTRIBUTION LIST

	No. Copies
1. Defense Technical Information Center Cameron Station Alexandria, Virginia 22304-6145	2
2. Library, Code 52 Naval Postgraduate School Monterey, California 93943-5002	2
3. Chairman, Electrical and Computer Engineering Code EC Naval Postgraduate School Monterey, California 93943	1
4. Chairman, Electronic Warfare Academic Group Code EW Naval Postgraduate School Monterey, California 93943	1
5. Professor R. W. Adler Code EC/Ab Department of Electrical and Computer Engineering Naval Postgraduate School Monterey, California 93943	3
6. Professor S. Jauregui, Jr. Code EC/Ja Department of Electrical and Computer Engineering Naval Postgraduate School Monterey, California 93943	1
7. Sr. V.ALM. Director de Instruccion Cuartel General de Marina-San Miguel Av. La Marina S/N Alt. Cdra. 35 San Miguel Lima, Peru	1
8. Commander Naval Space and Naval Warfare Systems Cmd. Attention: LCDR E. R. Arbogast PMW-143 Washington, D.C. 20363	1

- | | |
|---|---|
| 9. Commander Naval Security Group Command
Naval Security Group
Attention: G-82
Nebraska Ave.
Washington, D.C. 20390 | 1 |
| 10. Mr. H. Kobayashi
Department of Commerce
179 Admiral Cochrane Drive
Annapolis, MD 21401 | 1 |
| 11. Dr. W. M. Sherrill
Southwest Research Institute
6220 Culebra Road P.O. Drawer 28510
San Antonio, Texas 78228-0510 | 1 |
| 12. CDR H. Thornberry
Clemente X 335 San Isidro
Lima, Peru | 3 |